Fabrication, Characterization and Modeling of Functionally Graded Materials

Po-Hua Lee

Submitted in partial fulfillment of the
requirements for the degree of
Doctor of Philosophy
in the Graduate School of Arts and Sciences

COLUMBIA UNIVERSITY

2013

ABSTRACT

Fabrication, Characterization and Modeling of Functionally Graded Materials

Po-Hua Lee

In the past few decades, a number of theoretical and experimental studies for design, fabrication and performance analysis of solar panel systems (photovoltaic/thermal systems) have been documented. The existing literature shows that the use of solar energy provides a promising solution to alleviate the shortage of natural resources and the environmental pollution associated with electricity generation. A hybrid solar panel has been invented to integrate photovoltaic (PV) cells onto a substrate through a functionally graded material (FGM) with water tubes cast inside, through which water flow serves as both a heat sink and a solar heat collector. Due to the unique and graded material properties of FGMs, this novel design not only supplies efficient thermal harvest and electrical production, but also provides benefits such as structural integrity and material efficiency.

In this work, a sedimentation method has been used to fabricate aluminum (Al) and high-density polyethylene (HDPE) FGMs. The size effect of aluminum powder on the material gradation along the depth direction is investigated. Aluminum powder or the mixture of Al and HDPE powder is thoroughly mixed and uniformly dispersed in ethanol and then subjected to sedimentation. During the sedimentation process, the concentration of Al and HDPE particles temporally and spatially changes in the depth direction due to the non-uniform motion of particles; this change further affects the effective viscosity of the suspension and thus changes the drag force of particles. A Stokes' law based model is developed to simulate the sedimentation process, demonstrate the effect of manufacturing parameters on sedimentation, and predict the graded microstructure of deposition in the depth direction.

In order to improve the modeling for sedimentation behavior of particles, the Eshelby's equivalent inclusion method (EIM) is presented to determine the interaction between particles, which is not considered in a Stokes' law based model. This method is initially applied to study the case of one drop moving in a viscous fluid; the solution recovers the closed

form classic solution when the drop is spherical. Moreover, this method is general and can be applied to the cases of different drop shapes and the interaction between multiple drops. The translation velocities of the drops depend on the relative position, the center-to-center distance of drops, the viscosity and size of drops. For the case of a pair of identical spherical drops, the present method using a linear approximation of the eigenstrain rate has provided a very close solution to the classic explicit solution. If a higher order of the polynomial form of the eigenstrain rate is used, one can expect a more accurate result.

To meet the final goal of mass production of the aforementioned Al-HDPE FGM, a faster and more economical material manufacturing method is proposed through a vibration method. The particle segregation of larger aluminum particles embedded in the concentrated suspension of smaller high-density polyethylene is investigated under vibration with different frequencies and magnitudes. Altering experimental parameters including time and amplitude of vibration, the suspension exhibits different particle segregation patterns: uniform-like, graded and bi-layered. For material characterization, small cylinder films of Al-HDPE system FGM are obtained after the stages of dry, melt and solidification.

Solar panel prototypes are fabricated and tested at different water flow rates and solar irradiation intensities. The temperature distribution in the solar panel is measured and simulated to evaluate the performance of the solar panel. Finite element simulation results are very consistent with the experimental data. The understanding of heat transfer in the hybrid solar panel prototypes gained through this study will provide a foundation for future solar panel design and optimization.

Contents

List of Figures

List of Tables

ACKNOWLEDGMENTS

I am sincerely and heartily grateful to my advisor, Professor Huiming Yin, for the support and guidance he showed me throughout my dissertation writing. I am sure this work would have never been possible without his help. Besides, he always encouraged me, enlightened me, and provided endless advice and insight into my research and my career. It is my great pleasure and honor to have him as my doctoral advisor.

I am also grateful to the members of my dissertation committee, Professor Christian Meyer, Professor Raimondo Betti, and Professor James Im of Columbia University, and Professor Jeong-Ho Kim of the University of Connecticut, for taking their valuable time to participate my defense, and to read and comment on this dissertation.

Over the past four years, I have received support from a great number of individuals. I am obliged to Liming, Travis, and Adrian from the Carleton Lab who helped me in my experiment. I also owe sincere and earnest thankfulness to Zifeng, Yingjie, Hao and Lingqi for their technical support; Dajiang, Matt and Sung for their test experience; and Pablo, Brett, Patrick, Liang and Jack for their help with my writing.

I would like to thank to my parents for their unyielding support. My father Tzen-Chin was a role model throughout this entire process, serving as an example for which I could aspire to. My mother Shu-Chuan was always ready to help me when I needed and to provide very necessary moral support.

Special thanks to my wife, Chih-Wei, for your love. You brought me happiness and inspiration through the difficult and stressful times during these doctoral study years. This dissertation is your accomplishment as well.

The financial support of the National Science Foundation is greatly appreciated. This work was supported under grant CMMI 0954717. Research assistantship support provided by the Department of Civil Engineering and Engineering Mechanics, and Boris A. Bakhmeteff fellowship provided by the Department of Applied Physics and Applied Mathematics are also gratefully acknowledged.

To my parents & wife

Chapter 1

Introduction

Functionally graded materials (FGMs) exhibit a continuous variation of material properties which result from the non-homogenous microstructure (Miyamoto et al., 1999; Neubrand, 2001). Due to the unique graded material properties, FGMs have attracted a great amount of attention from researchers in many fields, including aerospace, biomaterials and engineering, among others, in the past few decades. In the novel design of a hybrid solar roofing panel system discussed in this thesis (Yin et al., 2009; Yin, 2009; Yin et al., 2012, 2013), an aluminum and high-density polyethylene (Al-HDPE) FGM is integrated to provide the combined benefits of heat harvesting efficiency, material efficiency and structural integrity. This dissertation primarily investigates the fabrication and characterization of this Al-HDPE FGM, as well as the corresponding modeling and simulations. In what follows, the fundamentals, background, motivation and scope of this work are introduced.

1.1 Functionally Graded Materials

1.1.1 Properties of Functionally Graded Materials

Functionally graded materials (FGMs) possess a position-dependent microstructure, chemical composition or atomic order, which may result in the continuous variation of material properties with position (Neubrand, 2001), such as mechanical, electrical and thermal prop-

erties. The two basic structures of gradation are illustrated in Figure 1.1.1. For the continuously graded structure, two different material phases gradually change from one side to another, as shown in Figure 1.1.1(a); whereas in Figure 1.1.1(b), material phases change in a discontinuous manner, such as a stepwise gradation which is also called segmented FGMs. The spatial gradation may exhibit at a global or local level. In a global gradation (Figure 1.1.1), the variation of properties extends over the bulk of the material. On the contrary, local gradation is restricted to a specific location in the material, such as coating on the surface or joint in the interfacial region as shown in Figure 1.1.2 (Miyamoto et al., 1999).

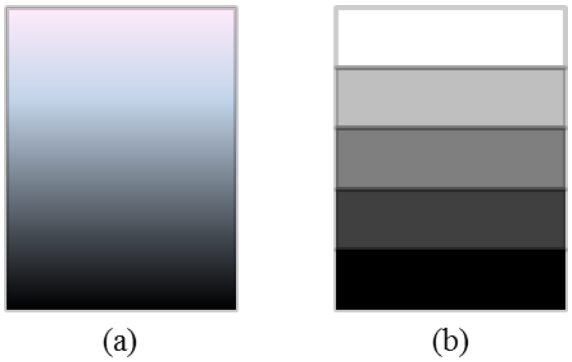

Figure 1.1.1: (a) Continuous and (b) stepwise graded structures

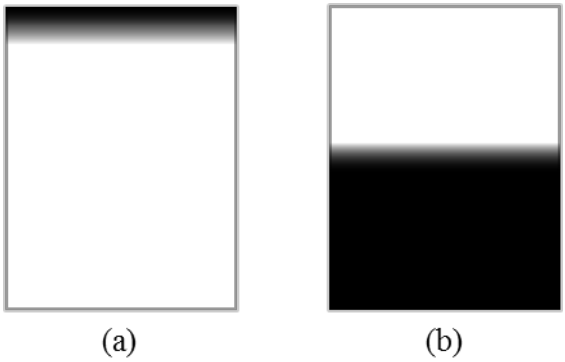

Figure 1.1.2: Local gradient at the (a) surface and (b) joint

In terms of microstructures, there are four general types of gradation: volume fraction, shape, orientation and size of material, as illustrated in Figure 1.1.3. The gradation of material could be described as a transition function, which is the relation between spatial position and gradient status. FGMs can be either artificial or natural. Animal bones and

bamboo are excellent examples of natural FGMs. For these two cases, combination of more than one type of gradation may occur. In the cross section of a typical animal bone, the reduction of both volume fraction and size of porosity from the inner to the outer surface are observed in Figure 1.1.4(a) (Wang et al., 2012). As for vascular bundles in bamboo, shown in Figure 1.1.4(b), the volume fraction increases and size decreases from the inner to the outer surface, respectively. Due to the graded distribution of vascular bundles, the effective elastic modulus of bamboo varies continuously in the radial direction. The radial elastic moduli and ultimate strength of bamboo are measured and analyzed by the hollow cylinder test, details of which are described in Appendix A. The gradation in both bone and bamboo provide the function of accommodating or sustaining external force in a similar way.

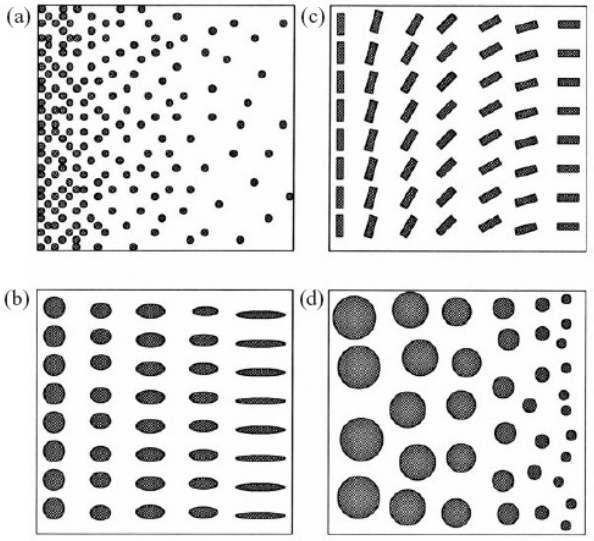

Figure 1.1.3: Different types of FEM. Gradation of (a) volume fraction, (b) shape, (c) orientation and (d) size (Neubrand, 2001)

In this work, Al-HDPE FGMs have been successfully fabricated by the sedimentation and vibration methods. To be an efficient heat collector, the aluminum-rich side is attached to a photovoltaic (PV) cell to absorb the heat collected from solar irradiation. On the other hand, the HDPE-rich side prevents heat leakage so that the thermal energy remains inside the FGM, to be taken by the water flow. As shown in Figure 1.1.4(c), the volume fraction of aluminum is about 50% at the bottom, and gradually reduces to 0% along thickness

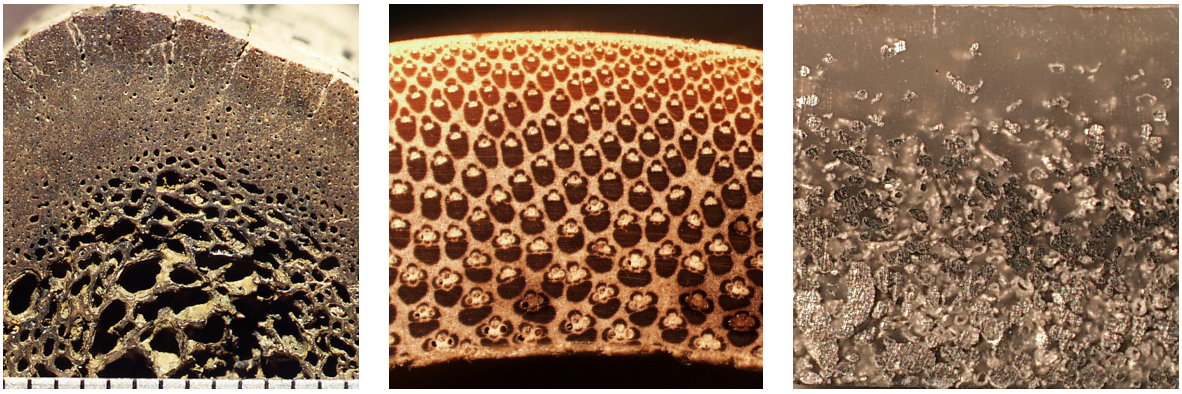

(a) (b) (c)

Figure 1.1.4: Combination of more than one type of gradation in cross section of: (a) animal bone, (b) bamboo, (c) Al-HDPE FGM

direction; additionally, the size of aluminum particles decreases from bottom to top. The processes of both experimental and theoretical study will be described in Chapters 2 - 5.

1.1.2 History of Functionally Graded Materials

The original idea of compositional and structural gradient in material microstructure was first proposed for composites and polymeric materials in 1972. Bever (1972) studied various gradient composites, investigated the global material properties and reviewed potential applications of graded composites. Shen (1972) reported that the gradation of polymeric material might be induced by the variation of the chemical nature of the monomers, the molecular constitution of the polymers and the supramolecular structure or morphology of the polymers. The effective properties, such as chemical, mechanical, biomedical and transport properties, and possible applications, including gasoline tank and damping materials, were considered. However, the design, fabrication and evaluation of this gradient structure was not studied.

Until 1985, the use of continuous texture control was presented to improve the adhesion strength and minimize the thermal stress in the ceramic coatings and joints being developed for a reusable rocket engine (Niino et al., 1986). More general concepts applied to impart new

properties and functions of materials were proposed by continuous control of the microstructure; also the design of such materials was initially introduced. The term of "functionally graded materials (FGMs)" was coined for these gradient composites and materials for more accurate description and grammar in 1986. In 1987, the famous research plan of FGMs, "Fundamental Studies on the Relaxation of Thermal Stress by Tailoring Graded Structures", was pioneered in the thermal barrier for a space plane in Japan (Koizumi and Niino, 1995). The capabilities of withstanding a surface temperature of 1700 $^{\circ}C$ and a temperature gradient of 1000 $^{\circ}C$ across only a 10 mm section were achieved by FGMs as a thermal barrier. The results and development of this research project were spread worldwide via papers, media and international conferences.

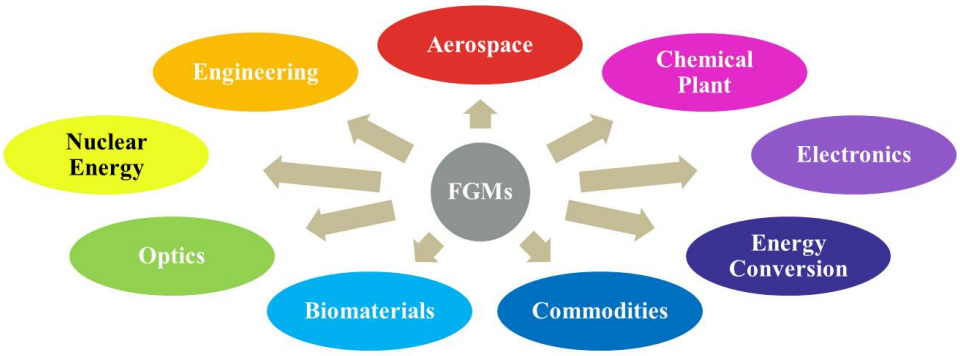

Figure 1.1.5: Potentially applicable fields for FGMs (Miyamoto et al., 1999)

Due to their unique graded material properties, FGMs attracted great amounts of researcher interest; FGMs are potentially widely applicable in numerous fields, as shown in Figure 1.1.5. In addition to the aforementioned thermal barriers, coatings and joints in aerospace, FGMs have also been developed for other novel applications.

In the field of biomaterials, biomedical implants, such as artificial bones and dental implants, are classic examples. Tampieri et al. (2001) attempted to produce the porosity-graded hydroxyapatite (HAP) ceramics, which not only provide good and fast bone ingrowth but also withstand early physiological stress, as an implant to replace natural bone. Many other researchers agreed and reported that FGMs could provide the implant a suitable stiffness to

endure the physiological loading, and that the graded porosity structure could enhance the mechanical property of the implant to optimize the material's response to external loading (Becker and Bolton, 1997; Pompe et al., 2003; Wang et al., 2012). As for dental implants, titanium/hydroxyapatite (Ti/HAP) FGMs exhibited good biocompatibility and mechanical toughness (Watari et al., 1995). No inflammation was observed in both traditional pure Ti and improved Ti/HAP FGM dental implants after eight weeks. But, Ti/HAP FGM implants showed better biocompatibility for newly formed bone (Watari et al., 1997).

1.1.3 Fabrication of Functionally Graded Materials

During the famous FGM program in Japan from 1987 to 1991, several processing methods were developed for FGM parts as a thermal barrier of a space plane. These former methods included powder metallurgy, plasma spraying, physical and chemical vapor deposition, self-propagating high temperature synthesis (SHS) and galvanoforming. Since 1991, various new methods have been invented and developed. The processing of FGMs has been categorized in different ways in reviews papers (Mortensen and Suresh, 1995; Neubrand and Rodel, 1997; Miyamoto et al., 1999). As shown in Figure 1.1.6, Miyamoto et al. (1999) classified the fabrication of FGMs into four categories including bulk, layer, preform and melt processing.

To scale up the manufacturing of Al-HDPE FGMs, various FGM manufacturing methods have been reviewed for cost savings and expediency (Suresh and Mortensen, 1998; Miyamoto et al., 1999). Powder metallurgy (PM) is one of the most popular ways, including powder stacking, plasma spraying, slip casting, electrophoretic deposition and sedimentation, among others. (Kieback et al., 2003). However, some PM methods, such as sequential slip casting (Moya et al., 1992), will make the FGM possess sharp interfaces causing the phenomenon of residual thermal stresses and thermal expansion mismatch between different layers. In order to eliminate the interfaces successfully and to produce the continuous gradation of material, sedimentation and vibration methods are used in this work.

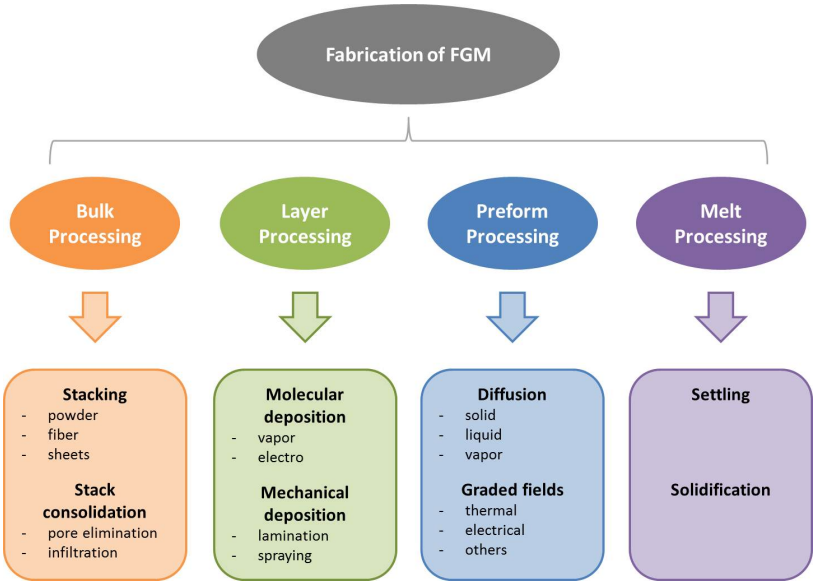

Figure 1.1.6: Proceeding methods and classification for fabrication of FGMs

1.2 Sedimentation Behavior of Particles

As described in the previous section, the sedimentation method is selected to fabricate the functionally graded materials (FGMs). In addition to the experiment, a model is also developed to simulate the dynamic behavior of particles during the sedimentation process. The fundamental theories involved in the modeling, including Stokes' law and Eshelby's equivalent inclusion method (EIM), will be first introduced in this section.

1.2.1 Reynolds Number and Stokes' law

In fluid mechanics problems, it is fundamental to define the flow condition before the analysis. Two different types of flow, laminar flow and turbulent flow, may occur in a fluid in a channel largely depending on the velocity of the flow. Laminar flow, also called streamline flow, is a flow condition in which fluid flows in parallel layers without disruptions between layers, and it always occurs at lower velocity. Opposite to laminar flow, turbulent flow shows a more complicated flow regime characterized by chaotic and stochastic behaviors, which include low momentum diffusion, high momentum convection, and rapid variation of pressure and velocity in space and time. The illustration of laminar and turbulent flow is showed in Figure

1.2.1. The so-called Reynolds number (Re) is the dimensionless parameter to distinguish these two flow regimes and is defined as:

$$Re = \frac{\rho v L}{\mu} = \frac{v L}{\nu} \tag{1.2.1}$$

where ρ, v, L, μ and ν are the density of fluid, the mean velocity of the object relative to the fluid, a characteristic linear dimension, the dynamic viscosity of the fluid and the kinematic viscosity of the fluid, respectively; all these parameters are SI units. In the case of a spherical particle moving in the fluid, the characteristic linear dimension would be the diameter of the particle. For a flow through a circular cross-section of a straight pipe, the fluid motion may remain laminar at Reynolds numbers below the critical value of approximately 2040; on the contrary, the flow could be turbulent at larger Reynolds number (Avila et al., 2011). Stokes flow is the extreme case of laminar flow at Reynolds number much less than 1.

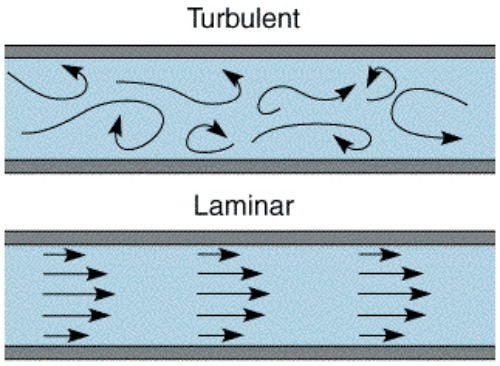

Figure 1.2.1: Illustration of laminar and turbulent flow

Reynolds number is defined as the ratio of the inertial forces to the viscous forces. Here, the inertial force is not defined in the classic way; rather, it characterizes the rate of change in momentum for a particular fluid volume element in motion and is defined as

$$F_i^{inertial} = \rho \left(\frac{\partial v_i}{\partial t} + u_j \frac{\partial v_i}{\partial x_j} \right) \tag{1.2.2}$$

where ρ, v, t and x are the density of fluid, the velocity of fluid, time and position, respec-

tively. The viscous force is the shear stress for a particular fluid volume element caused by the viscosity of fluid and is defined as

$$F_i^{viscous} = \mu \left(\frac{\partial^2 v_i}{\partial x_j \partial x_j} \right) \tag{1.2.3}$$

Therefore, in a viscous fluid with small Reynolds number ($Re << 1$), the inertia forces may be disregarded in the Navier-Stokes equation, which becomes the Stokes equation, and the vorticity field and stream function can be solved. Consequently, the force on the surface can be obtained, and the drag force can be determined by the integral of the surface force. For a rigid sphere moving in a liquid, the drag force is written as

$$D_i^s = 6\pi a \mu v_i \tag{1.2.4}$$

where D^s, a, μ and v are the magnitude of the drag force for the rigid sphere, the radius of the rigid sphere, the viscosity of the liquid, and the settling velocity of the rigid sphere, respectively. The formulation (1.2.4) is well known as Stokes' law to determine the frictional force, caused by the viscosity of the liquid, acting on a moving solid sphere (Batchelor, 1967). As for a spherical drop moving in a different fluid, such as a gas bubble or insoluble drop, the drag force has been derived in a similar fashion (Batchelor, 1967). In addition, the drag force of other shapes of object moving through liquid has also been investigated, such as an ellipsoid and a circular disk (Lamb, 1975).

Under Stokes flow ($Re << 1$), the motion of a falling spherical object will reach the terminal velocity rapidly if there is no external force applied. The terminal velocity can be determined by the balance between the drag (frictional) force and the driving (e.g. buoyant or gravitational) force and written as (Batchelor (1967))

$$U_i^0 = \frac{2a^2 \left(\rho^s - \rho^l \right)}{9\mu} g_i \tag{1.2.5}$$

where ρ^s, ρ^l, μ and g are the density of the rigid sphere, the density of the liquid, the viscosity of the liquid, and the acceleration due to gravity, respectively.

For all sets of sedimentation experiments studied in this thesis, the settling motion of aluminum and high-density polyethylene particles in ethanol is under Stokes flow because of the micro-size of particles. Thus, the model for predicting the sedimentation behavior of particles, which is discussed in Chapter 2, is based on Stokes' law. Even though the self-consistent method, which considers the time-dependent volume fraction of particles, viscosity and settling velocity, is included in the Stokes' law-based model, the interaction between particles is not considered. Therefore, the approach proposed in this thesis, Eshelby's equivalent inclusion method, is introduced and developed for a better understanding of the sedimentation of numerous particles.

1.2.2 Eshelby's Equivalent Inclusion Method

In the case of a Stokes flow, the hydrodynamic Green's function, also called the Stokeslet, is the fundamental solution of the Stokes equation. For a point in the viscous liquid applied with a concentrated force $\mathbf{F}$, the velocity field $\mathbf{v}$ caused by the force could be written in terms of the Stokeslet as

$$v_i(x) = G_{ij} F_j \tag{1.2.6}$$

where G_{ij} is the hydrodynamic Green's function, also known as the Oseen-Burgers tensor, as follows

$$G_{ij} = \frac{1}{4\pi\mu}\left[\frac{\delta_{ij}}{|x-x'|} - \frac{1}{2}\frac{\partial^2|x-x'|}{\partial x_i \partial x_j}\right] \tag{1.2.7}$$

The hydrodynamic Green's function has been derived by several different methods as follows. Kim and Karilla (1991) have developed the solution of the Stokeslet by making use of the linearity of the Stokes equations and symmetries of the system with the Fourier transform. Also, basing on the linearity of the Stokes equations, a physical approach has been derived by Dhont (1996). Zapryanov and Tabakova (1998) took the divergence of Stokes

equation, and applied the Fourier transform and the fundamental solution of the Laplace equation to solve the Stokeslet. The Stokeslet is essential for the derivation in this work, which is also referred to as the Green's function.

A new approach to derive the drag force using Eshelby's equivalent inclusion method (EIM) is presented. Eshelby (1957; 1959) first studied the stress for an inhomogeneity in an infinite matrix under a uniform far field stress and proposed that the stress disturbance caused by the inhomogeneity could be simulated by an inclusion with the same material properties as the matrix but with a appropriately chosen eigenstrain. This method is coined as Eshelby's equivalent inclusion method (EIM). The beauty of this method is that the eigenstrain is a constant when the inhomogeneity is ellipsoidal. The EIM is not only valuable for the effective elastic moduli of composites (Y. Takao et al., 1982; Chen and Cheng, 1996; Yin et al., 2008a), but it also has been successfully applied to the prediction of thermal and electric behavior of composites, e.g., work-harden rate (Huang, 1996), thermal steady-state heat conduction (Hatta and Taya, 1986) and thermal expansion coefficient (Takei et al., 1991a,b; Sakata et al., 2010) and electroelastic moduli (Dunn and Taya, 1993). In the elastic problem of an infinite domain containing an inhomogeneity, the overall elastic fields, stress, strain and displacement field are the summation of far field and disturbed elastic field. The elastic Green's function provides the connection between disturbed strain field and eigenstrain of the equivalent inclusion; the EIM is used to link the eigenstrain of the equivalent inclusion and far field strain field together (Mura, 1987).

Before now, the EIM has not been used in problems of fluid mechanics. Although a fluid has distinct material behavior from a solid, the mathematical formulation is very similar. The main difficulty in using the concept of EIM for a drop moving in a different fluid is that not only is the material property of the drop different from the matrix fluid, but also a driving force is applied on the drop. The work in this thesis successfully extends the EIM to the above-mentioned problem and formulates the velocity and stress field in the fluid.

When a drop moves at a constant velocity in an infinite domain of a different liquid, the

driving force, such as gravity or buoyancy, will be exactly balanced by the drag force from the viscous fluid. Therefore, given a driving force, if the terminal velocity can be determined, the correlation between the velocity and the drag force can also be obtained from the relationship of the velocity and the driving force, which creates a new approach to derive the drag force bypassing the boundary integral of the stress vector over the drop surface.

To find the correlation between the driving force and the terminal velocity, the EIM with a continuous boundary condition will be used. If the drop has the same viscosity as the liquid, the motion of the drop and the distributed driving force can be directly written in terms of the integral of Eq.(1.2.6) over the volume of the drop. However, due to the difference in viscosities between the liquid and the drop, the motion of the drop will surely be different. Using the EIM, the viscosity mismatch between the drop and the liquid can be simulated by introducing an eigenstrain rate. Then the overall velocity field can be written in terms of the combination of the velocity field caused by the driving force and the velocity field caused by the eigenstrain rate.

1.3 Photovoltaic/Thermal Hybrid Solar Technology

The development of photovoltaic/thermal hybrid solar technology demonstrates the potential and prospects of solar energy. In our hybrid solar roofing panel system, the aluminum and high-density polyethylene functionally graded materials (Al-HDPE FGMs) is integrated to provide the advantages of heat harvesting efficiency, material efficiency and structural integrity (Yin et al., 2009; Yin, 2009; Yin et al., 2012, 2013). In this section, the background, motivation and history of photovoltaic/thermal hybrid solar systems are introduced, as well as the design and function of the proposed hybrid solar roofing panel system.

1.3.1 Background and Motivation

In past few decades, the natural resource consumption and the pollution during electric generation became critical and urgent issues. In the US, about 40% of all energy and a

considerable percentage of non-recyclable building materials and non-renewable natural resources were consumed by residential and commercial buildings; especially, the consumption of energy was increased by 48% between 1980 and 2009 (D&R International, 2011). The use of renewable energy, such as solar energy, wind power, hydro-power and geothermal energy, was considered as the solution to release both of these environmental burdens. In the topic of solar technology, the photovoltaic/thermal hybrid solar system has demonstrated a promising performance in recent years.

A photovoltaic/thermal hybrid solar system (PVT system) is an integrated system of photovoltaic and solar thermal components/systems which produce electricity and collect heat. The solar cell only utilizes particular energy band gap which mainly the wavelength is within the ultraviolet and visible light, as shown in Figure 1.3.1. Thus, a common PVT system converts 4~21% of the solar irradiation into electricity, depending on the type of solar cells in use and working conditions. In other words, the electricity conversion does not take place in the range of infrared light, which means more than 50% of solar energy is wasted as heat. The excess heat causes the extreme high working temperature, $70°C$ or higher in summer, and this may lead to undesirable effects. First, the efficiency of solar cell will be significantly reduced (Yang and Yin, 2011; Yin et al., 2013); and second, the long-term thermal stress among the interface between different components may yield permanent structural damage and shorten its lifetime. The improvement by cooling and controlling the temperature of solar cells with air or water has been studied for several decades, the history and details are described later. The main feature of a flat-plate PVT collect is shown in Figure 1.3.2, and the several common designs of air-type and water-type PVT collector are shown in Figure 1.3.3.

1.3.2 History of Solar Roofing Panel

In the mid-1970s, theoretical and experimental investigations on photovoltaic/thermal hybrid solar system were initially documented. The fundamental concept and the data with

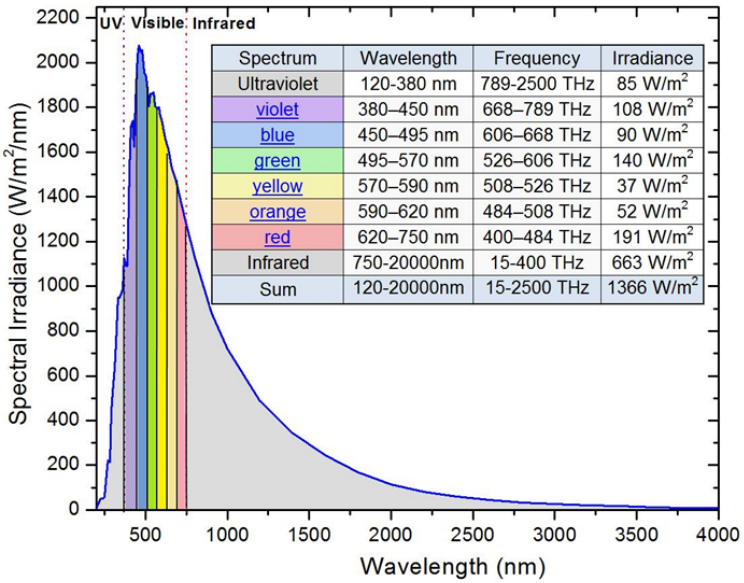

Figure 1.3.1: The standard Extraterrestrial Solar Spectrum

the use of either air or water flow for cooling, which are called PVT air and water systems respectively, were proposed by Florschuetz (1975; 1979), Wolf (1976), Kern and Russell (1978) and Hendrie (1979). Afterward, the research work of technical validity and performance analysis on flat-plate collectors (Figure 1.3.2) was conducted (Raghuraman, 1981; Cox III and Raghuraman, 1985; Braunstein and Kornfeld, 1986; Lalovic et al., 1986). From the late 1980s, the performance of different designs of air-type and water-type PVT collectors, as shown in Figure 1.3.3, were analyzed and compared.

For an air-type PVT collector system, the detailed analytical and experimental studies of different designs were demonstrated by Garg and his co-workers (Garg and Adhikari, 1997, 1998). Compared with the double glass cover, a single glass cover may collect more heat; however, the overall energy performance of a double glass cover was better than single glass. The effect on efficiency of an air-type PVT system produced by the design parameters, such as dimension of absorber plate and flow rate, was observed; the longer length and less depth of absorber and the faster air-flow rate lead to an increased thermal and electrical outputs (Bhargava et al., 1991; Garg and Adhikari, 1999). The performance of single-pass and double-pass designs (See in Figure 1.3.3(a)) were investigated in both modeling and

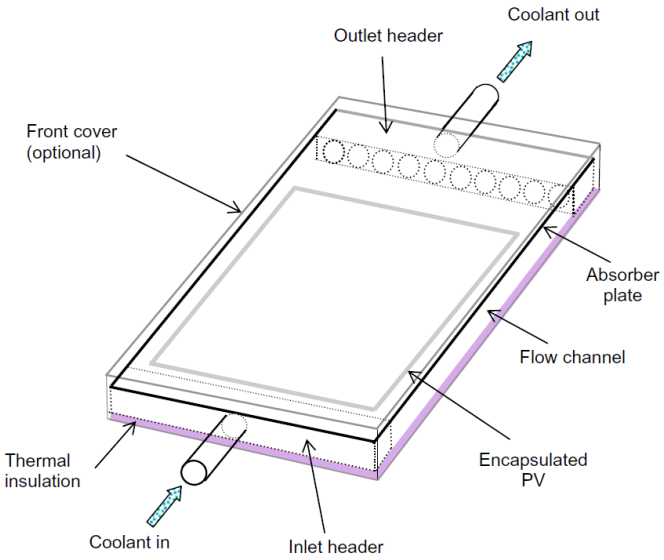

Figure 1.3.2: Main features of a flat-plate PVT collector (Chow, 2010)

experiments, the double-pass design showed better performance due to superior cooling of the front cover and solar cells (Sopian et al., 1996, 2000). For a conventional PVT collector, Prakash (1994) pointed out that water-type designs provided higher thermal efficiency than air-type because of the lower heat transfer between the air-flow and absorber plate.

Moreover, the modeling of different designs of water-type PVT collector systems were explored. Similarly, the single-covered design showed the better performance than uncovered and double-covered designs, which produced relatively low thermal and electrical efficiency respectively (Vries, 1998). However, the analysis indicated that exergy output density of the single-covered design was slightly lower than the uncovered design, which meant that so much unavailable energy existed in the thermal energy (Fujisawa and Tani, 1997). The studies expressing the relation between efficiency and design parameters, including the diameter of the tube and the quantity of water, were documented (Bergene and Lovvik, 1995; Agarwal and Garg, 1994). Additionally, the experimental tests of water-type PVT collector ware discussed and compared. Al Harbi et. al. (1998) found that there was a 30% reduction of PV cell efficiency when the water-type PVT system is operated at a high ambient temperature whereas the thermal efficiency keeps good. The prototypes of thermoelectric

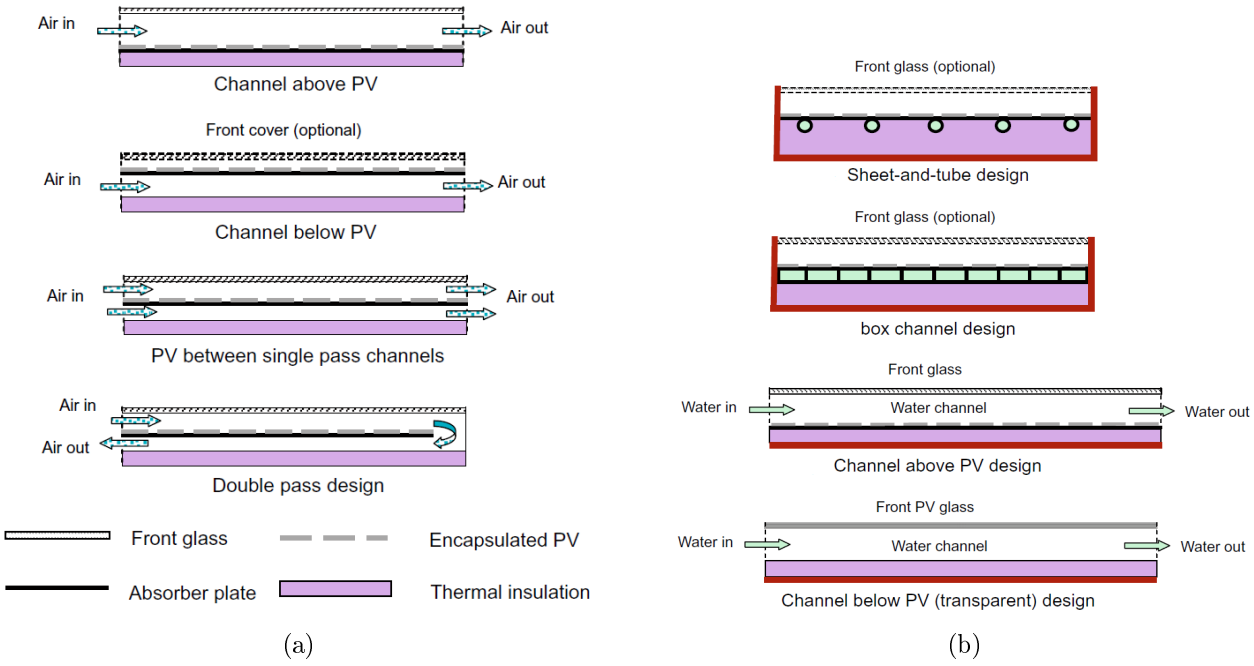

Figure 1.3.3: Longitudinal cross-sections of some common (a) air-type PVT and (b) water-type PVT collector designs (Chow, 2010)

collectors and water-type PVT collectors were constructed and tested by Rockendorf et al. (1999), the electrical output of the water-type PVT collector is significantly higher than that of thermoelectric collector.

Generally speaking, for the flat-plate collectors, the thermal efficiency of water-type PVT collector systems is within the range of 45~70% depending on the design; as for the air-type PVT collector system with optimized design, the thermal efficiency is up to 55% . According to long-term efforts of Research and Development on PVT collector system, for practical real-building applications, the air-type and water-type designs become more and more popular in both Europe and North America.

1.3.3 Hybrid Solar Roofing Panel

Different from the aforementioned conventional designs, a novel functionally graded material (FGM) based hybrid solar roofing panel as shown in Figure 1.3.4 is developed (Yin et al., 2013). This roofing panel system consists of four major components, which the or-

der from top to bottom are the protective layer, the photovoltaic (PV) cell, the aluminum and high-density polyethylene system functionally graded material (Al-HDPE FGM) interlayer and the structural substrate, respectively. The transparent protective waterproofing layer protects the power generating elements and the underlying building materials from external environmental distress such as moisture migration, surface wear, and impact. The photovoltaic (PV) cell generates power using proven mono-crystalline PV technology. The FGM layer is constructed of a mixture of heat conducting aluminum (Al) and insulating high density polyethylene (HDPE) with water tubes cast inside, which is integrated upon a structural substrate. The strong substrate in bottom, which is made of recycled polymer, provides mechanical loading support and heat insulation of the roof.

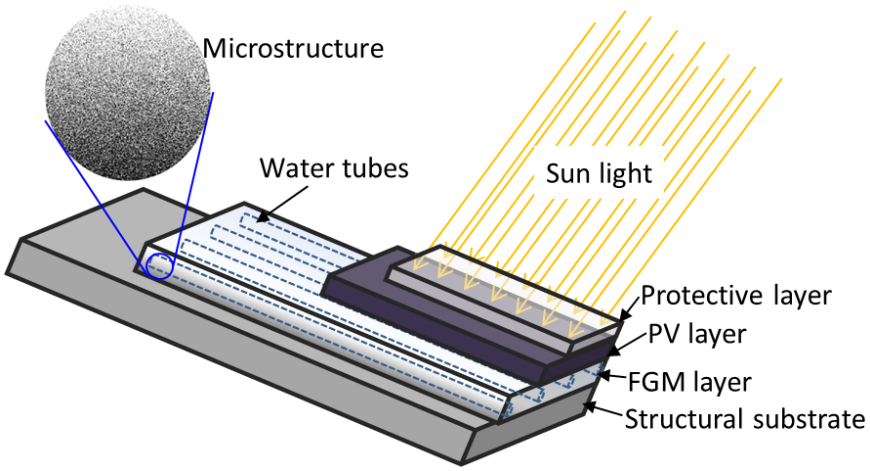

Figure 1.3.4: Schematic illustration of the hybrid solar roofing panel with a functionally graded layer (Yin et al., 2013)

The FGM interlayer contains aluminum powder dispersed in a high density polyethylene (HDPE) matrix with a graded microstructure seen in the left top of Figure 1.3.4; the volume fraction of aluminum is 50% at the top of the FGM interlayer, and continuously reduces to 0% at the bottom along the depth direction. The purpose of Al-HDPE FGM fabrication is to create a light-weight layer of solar roofing panel with gradient thermal conductivity in the depth direction, which is gradually transited from well conductive side attached with solar cell to highly insulative side bonded to the structural substrate. Water pipelines in a loop are

cast within the FGM to control the panel's temperature by using water flow rate controls and a temperature sensing system. The innovative design combined with photovoltaic/thermal hybrid solar system and temperature control system, whose cross section is illustrated in Figure 1.3.5, provides the multifunctional advantages of energy generation and savings as follow (Yin et al., 2013):

1. Improved PV efficiency - It is known that most current solar roofing panels only serve at the temperature range from -40 to $85°C$, and the energy utilization efficiency significantly reduces with increasing working temperatures (Skoplaki and Palyvos, 2009a,b). After exposure to solar radiation for a while, the temperature of a PV cell will increase; then, heat may be conducted from the PV cell to the upper part of the FGM. Cold water, whose flow is controlled by the panel, is introduced through the water tubes to cool down the PV module. Consequently, the efficiency of the PV cell will be improved under moderate temperature conditions. The relations between electricity generation efficiency and temperature under different irradiations, which are 850 and 1100 W/m^2, are depicted in Figure 1.3.6 (Yin et al., 2013).

2. Free heating supply - During the process of cooling the PV module, the heat is harvested in the water. After going through the holistic PVT system, the hot or warm water is collected in preheated water systems for floor and celing heating or domestic usage.

3. Reduced cooling demand - In summer, the excellent thermal insulation performance of the panel and the moderate roof temperature controlled by water flow will create a more comfort indoor condition, the energy for cooling demand can be saved in consequence.

4. Snow and ice removal - In winter, warm water can be introduced to remove ice and snow from the roof, clean solar panels, and thus restore and enhance solar energy utilization.

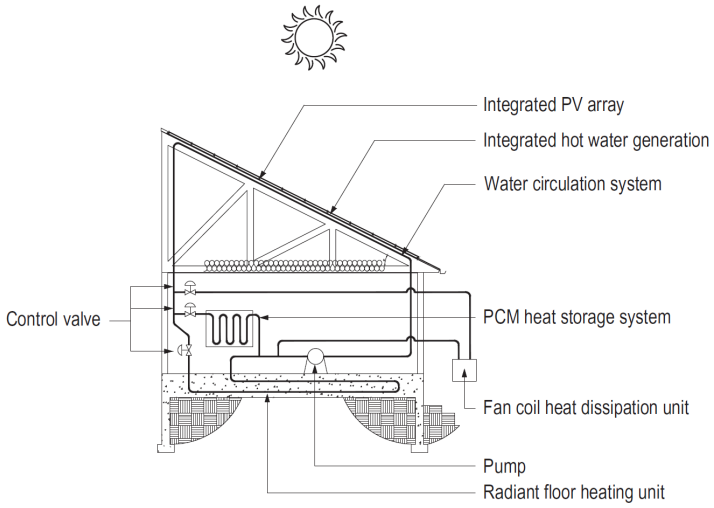

Figure 1.3.5: Cross section of residential system (Yin et al., 2013)

In addition to the above benefits, compared with the traditional sandwich construction, the use of Al-HDPE FGM interlayer reduces the total number of layers and provides the following benefits (Yin et al., 2013):

1. Heat harvesting efficiency - the water tubes are embedded in the top part of the FGM layer, where the high aluminum concentration creates high thermal conductivity so that heat can be effectively transferred to water tubes in all directions, while simultaneously being insulated by the bottom part of the FGM layer, which is made of pure HDPE.

2. Material efficiency - Due to the gradual variation of the phase proportion of materials, only a small amount of aluminum powder is needed. This reduces the cost of the panel as the aluminum material is relatively expensive.

3. Structural integrity - The absorber layer and insulation layer in traditional PVT can be replaced by one FGM layer which integrates the high thermal conductivity of the aluminum rich part in the top and the thermal insulation of the pure HDPE in the bottom. Since the volume fraction of aluminum (Al) powder continuously varies in the thickness direction, the thermo-mechanical property distribution changes smoothly, and avoids the thermal stress concentration across layers, increasing the structural

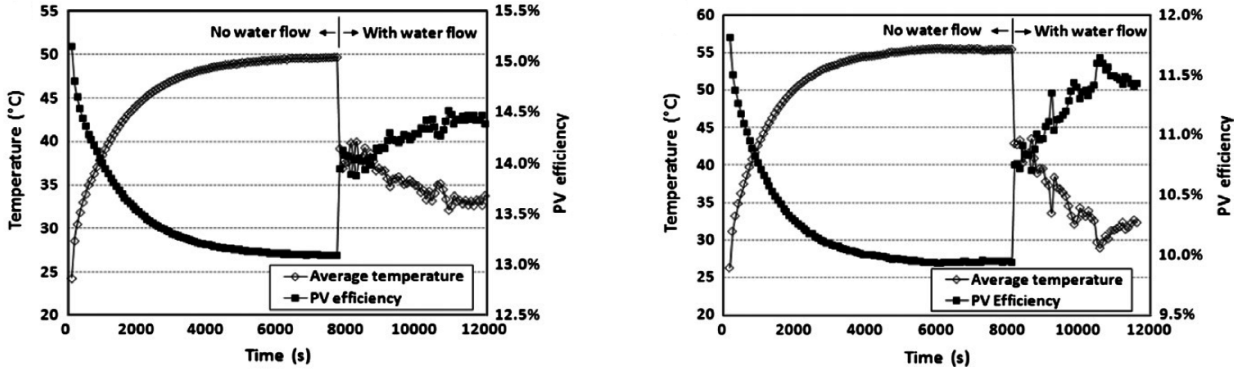

(a) (b)

Figure 1.3.6: Panel surface average temperature and PV efficiencies for (a) irradiation: 850 W/m^2, water flow rate: 33 ml/min, (b) irritation: 1100 W/m^2, water flow rate: 66 ml/min (Yin et al., 2013)

integrity and durability of the panels.

Figure 1.3.7 is the blue print of the final future goal - a net zero energy house, installed with a great deal of hybrid solar roofing panels and a water control system. The electricity and hot water for domestic usage could be generated by this solar roofing system. Thus, in order to achieve this dream, the economical and efficient fabrication of Al-HDPE FGM for mass production has to be first developed. The details and improvement of the fabrication method will be described in Chapters 2 - 5.

1.4 Scope

The primary objective of this study is to investigate the fabrication, characterization, and modeling of an aluminum and high-density polyethylene functionally graded material (Al-HDPE FGM), which is appropriately selected for the novel hybrid solar roofing panel system. Some relevant testing and analysis is also presented. The dissertation has been organized as follows:

Chapter 2 studies the fabrication of Al-HDPE FGM by the sedimentation method, as well as the simulation of the mixture of aluminum and high-density polyethylene powders

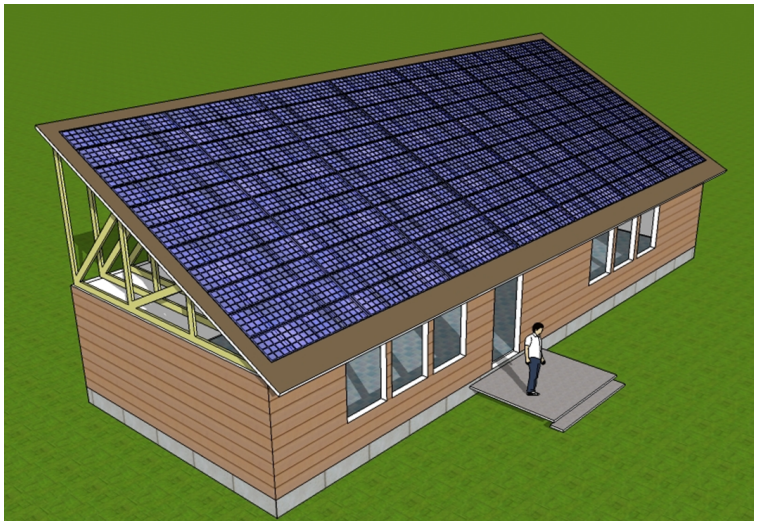

Figure 1.3.7: Future net zero energy house

settling in the ethanol by Stokes' law based modeling. For simplicity, the sedimentation test in which only fine aluminum particles (AL-104, 0.2~10 μm) dispersed in ethanol is firstly introduced, the modeling based on Stokes' law is also created by discrete method. The size distribution of the aluminum particles along the depth direction of deposition after 24 hours of sedimentation can be measured and predicted by experiment and simulation respectively. The good agreement between both results demonstrates the applicability of our modeling for the sedimentation behavior of particles under Stokes flow. Furthermore, the simple experiment is later extended to a more complicated case, where the mixture of aluminum and high-density polyethylene powders is well-dispersed and settling in the ethanol. According to the different size and density of materials, a gradient deposition of aluminum and high-density polyethylene is successfully produced, when the appropriate size of aluminum is selected.

Chapters 3 and 4 present a new approach on Eshelby's equivalent inclusion method to derive the Stokes flow of single, two or even numerous ellipsoidal drops moving in the viscous liquid. The purpose of this approach is to discuss the interaction between particles, which is not considered in the Stokes' law based modeling described in Chapter 2. Using the EIM, the viscosity mismatch between the drop and the liquid can be simulated by introducing an

eigenstrain rate. For the case of a single ellipsoidal drop, the eigenstrain rate can be assumed as a linear function; the velocity and pressure fields caused by the body force and eigenstrain rate on the inclusions of an infinite fluid domain can be obtained by the Green's function explicitly. When the drop is spherical, the solution recovers the well-known classic solution for a drop moving in a fluid (Batchelor, 1967).

However, for the case of two or more ellipsoidal drops, the eigenstrain rate distribution could be more complex. Instead, the eigenstrain rate distribution can be written in the polynomial form, and the coefficients of each order of the coordinate can be determined separately. Moreover, the translational velocities of the drops depend on the relative position, the center-to-center distance of drops, the viscosity and the size of drops. When two identical spherical drops are considered, the results of present method well agrees with Batchelor's solution (Batchelor, 1972).

Chapter 5 demonstrates another fabrication approach of Al-HDPE FGM by a vibration method for the mass production. The vibration method provides a faster and more economical manufacturing process. Under high-frequency vibration, the particle segregation of larger size aluminum particles (100 ~ 600 μm) embedded in smaller high-density polyethylene (1~100 μm) concentrated suspension is investigated. In the experiment, according to varied parameters including the amplitude, frequency and time of vibration, the suspension displays different particle segregation: uniform-like, gradient and bi-layered. The small cylinder films of Al-HDPE FGM is successfully obtained by the vibration method with appropriate experimental parameter, and this method can be also practical for the massive manufacture of thin interlayer of the novel hybrid solar roofing panel.

Chapter 6 presents the performance analysis of the novel hybrid solar roofing panel system by experiments and finite elements simulation. This novel system is invented to integrate photovoltaic (PV) cells onto a substrate through a functionally graded material (FGM) with water tubes cast inside, through which water serves as both a heat sink and a solar heat collector. Therefore, electrical efficiency of PV cells can be improved under a relatively low

temperature. The prototypes have been fabricated and tested at different water flow rates and solar irradiation intensities. The temperature distribution in the solar panel is measured and simulated to evaluate the performance of the solar panel. The finite element simulation results are very consistent with the experimental data. The understanding of heat transfer in the hybrid solar panel prototypes will provide a foundation for future solar panel design and optimization.

Chapter 7 documents the conclusions on the fabrication, characterization, and modeling of aluminum and high-density polyethylene functionally graded materials (Al-HDPE FGMs) and discusses the future research directions. Three appendices are also included: Appendix A develops a hollow cylinder test to characterize the strength and stiffness of bamboo specimens in the cross sectional plane. Based on the cellular microstructure and comparison of the elastic modulus distribution, the exponential function of elastic modulus provides the most reasonable results. Appendix B derives the velocity and pressure fields of drop moving in a viscous fluid, which is only applied with a concentrated force. Appendix C provides the expression of the integral terms of Φ, Ψ, Φ_p and Ψ_p and their derivatives, which are widely used in the Eshelby's equivalent inclusion method in Chapters 3 and 4.

Chapter 2

Fabrication of Aluminum and High-Density Polyethylene Functionally Graded Materials by the Sedimentation Method

A simple, economical, and scalable material manufacturing method of sedimentation has been used to fabricate functionally graded materials for solar roofing panels. This chapter investigates the size effect of aluminum powder on the material gradation in the depth direction when only aluminum powder or the mixture of aluminum and high-density polyethylene (HDPE) powder is thoroughly mixed and uniformly dispersed in ethanol and then subjected to sedimentation for a certain period respectively. A Stokes' law based model is developed to simulate the sedimentation process, in which the concentration of aluminum and high-density polyethylene (HDPE) particles temporally and spatially changes in the depth direction due to the non-uniform motion of particles. The concentration variation further affects the effective viscosity of the suspension and thus changes the drag force of particles. The numerical simulation demonstrates the effect of manufacturing parameters for sedimentation and pre-

dicts the graded microstructure of deposition in the depth direction. The present modeling and testing method provides a very useful tool for the material design and optimization of the solar roofing materials.

2.1 Overview

The functionally graded materials (FGMs) exhibit a non-homogenous microstructure, which results in the continuous variation of material properties, such as mechanical, electrical and thermal parameters (Krstic, 1983; Hu et al., 1998; Nishida et al., 2000; Yin et al., 2004, 2007, 2008b; Moussa et al., 2012). FGMs attract widespread attention for various novel engineering applications, such as bonding dissimilar materials (Zhou and Hashida, 2002), connecting electrodes and insulating containments (Nishida et al., 2000), and manufacturing thermal barriers (Khor et al., 1999; Bertolino et al., 2003). In our recent work (Yang et al., 2012; Yin et al., 2012, 2013), we have successfully fabricated an FGM with high density polyethylene (HDPE) and aluminum (Al) powders and integrated it into the hybrid solar roofing panel as Figure 1.3.4. The purpose of Al-HDPE FGM fabrication is to create a light-weight layer of solar roofing panel with gradient thermal conductivity in the thickness direction, which is gradually transited from a well conductive side attached with a PV solar cell (laminated by a protective layer) to another highly insulative side bonded to a structural substrate. The water flow through the FGM layer cools down photovoltaic (PV) cells and harvest the solar heat. Consequently, the efficiency of PV cell is improved while working under a moderate temperature condition; and the water flow through the FGM layer is useful for preheated water systems, which also intercepts the heat flow into the building for cooling savings.

To scale up the manufacturing of Al-HDPE FGMs, various FGM manufacture methods have been reviewed for manufacturing cost and speed (He et al., 1997; Suresh and Mortensen, 1998; Miyamoto et al., 1999; Cirakoglu et al., 2002). Powder metallurgy (PM) is the one of the most popular ways including powder stacking, plasma spraying, slip casting, elec-

trophoretic deposition and sedimentation etc (Neubrand et al., 2003). However, some kinds of PM methods, such as sequential slip casting (Moya et al., 1992), will make FGM with sharp interfaces causing the phenomenon of residual thermal stresses and thermal expansion mismatch between different layers.

Sedimentation method has been applied to fabricate FGM with continuous variation for eliminating the interfaces successfully in several setups and processes. Sanchez-Herencia et al. (1997) obtained Al2O3/Y-TZP continuous functionally graded ceramic (FGC) by filtration-sedimentation, where the gradient deposit body is moved out of plastic mold with a plaster-of-Paris basement after complete filtration and drying. Simonet et al. (2007) have studied both the experiment and simulation on YSZ/LSM FGM with two sedimentation process with different initial condition: one is that YSZ and LSM powders are mixed together in the water and homogenous dispersed in the whole vessel, and another is that YSZ and LSM particles only locates at the lower and upper part of suspension respectively. Yang et al. (2001) have developed the improved sedimentation process, both Ti and Mo start settling at a height of tube, to manufacture Ti-Mo FGMs without a homogenous bottom layer.

Yin et al. (2012) proposed to use sedimentation in manufacture of the FGM layer (Figure 1.3.4) with Al and HDPE powder, in which a suspension liquid is used to create the graded microstructure of the mixture. Because Al powder exhibits chemical reaction with water, ethanol is used to mix Al powder and HDPE powder. Because Al and HDPE have significantly different specific gravities (2.7 and 0.95, respectively) over a large range of size distribution, the two types of powders will fall down at different velocities and thus create a graded microstructure automatically. When a desired graded microstructure forms, the ethanol is filtered out for reuse. By heating up the graded powder mix in a vacuum oven, the HDPE powder will be melt so as to form a composite of Al particles dispersed in the HDPE matrix with graded microstructure. After curing it, one can obtain the solid FGM layer. To optimize the particle distribution and manufacturing speed, the sedimentation process should be quantitatively understood and controlled.

There exist several theories on the analysis of small particles sedimentation (Mirza and Richardson, 1979; Tory et al., 1995; Caron et al., 1996; Yang et al., 2008). Tory et al. (1995) used a fourth-order stochastic Runge-Kutta method to statistically determine the particle position and velocity at discrete time. Yang et al. (2008) considered various prevailing forces, such as van der Waals attractive, electrostatic repulsive, Brownian, depletion, gravitational, contact and drag force, acting on single particles. The Stokes' law (Batchelor, 1967), which can calculate the settling velocity of small spherical particle in viscous liquid under the laminar flow ($Re \ll 1$), has been used to predict the particle motion in sedimentation process. Yang et al. (2001) developed a mathematical model base on Stokes' law to predict the compositional distribution of Ti-Mo FGM systems. In their model, it is assumed that the viscosity of solution is not concentration-dependent but consistent as pure solvent because of the low volume ratio between solid and liquid, also the sedimentation velocity of particle can be constant as terminal velocity calculated by Stokes' law directly. This model is applicable to the sedimentation of a dilute suspension with a large sedimentation distance compared with particle size.

However, in the proposed manufacturing method for Al-HDPE FGMs, both the proportion of ethanol and the sedimentation distance should be minimized for low cost and fast manufacturing. Therefore, the existing models for dilute suspensions are not applicable to the proposed manufacturing method. As the first step toward fully understanding the sedimentation process of Al-HDPE mix, the goal of this chapter is to understand the sedimentation process of aluminum particles with size from 200 nm to 700 μm. The coupled behavior of particle concentration change and particle motion will be investigated by considering concentration-dependent viscosity of solution. Stokes' law based model for sedimentation tests has been developed, and particle size distribution has been experimentally measured and numerically simulated in this chapter.

First, for simplicity, only aluminum powder with size from 200 nm to 10 μm (Al-104 from Micron Metals, Inc.) was introduced into ethanol, was chosen to observe the sedimentation

behavior of small spherical particles. After complete sedimentation and drying, the deposit body was investigated layer by layer to measure the particle size distribution along the thickness direction by a particle analyzer. The model is used to predict the volume fraction of three groups of aluminum powder, containing different range of particle sizes, along the depth direction and to explore the effect of manufacturing parameters, such as height of suspension, for sedimentation behavior.

Moreover, the experiment has been extended to the mixture of Al and HDPE with different Al particle sizes, namely Al-104 (200 nm - 10 μm), Al-101 (2 - 100 μm) and Al-111(100 - 700 μm). For each group of Al powder, Al and HDPE particles were mixed uniformly in ethanol and then were subjected the sedimentation process. The density measurement of powder layer by layer, which is based on the Rice Density Measurement (ASTM D-2041), is used to determine the volume fraction of aluminum in depth direction of deposit body after complete sedimentation and drying. According to the observation of the Al and HDPE particle distribution, the graded and bi-layered mixtures of particles have been created for different Al particle groups. The aforementioned model has been extended to predict the volume fraction of aluminum in the mixtures.

The remainder of this chapter is organized as follows: Section 2.2 introduces the experiments including the apparatus, material preparation, testing procedure and measurement results. Section 2.3 presents the sedimentation model and provides the theoretical algorithm of simulation. Finally, Section 2.4 shows the comparison between experimental and numerical simulation results. Using the present model, parametric studies are conducted.

2.2 Experiment

2.2.1 Apparatus and Material Preparation

Three types of aluminum powders Al-101, Al-104 and Al-111, whose particle size distribution were showed in Figure 2.2.1, were used for experiment of sedimentation with the suspension of ethanol. Notice that the Al-101 and HDPE have very similar size distributions; Al-104

and HDPE exhibits spherical shape of particles; whereas Al-101 and Al-111 have irregular shape. The sedimentation device, as shown in Figure 2.2.2, with a diameter of 27 mm was used for sedimentation. The drain faucet was designed to drain the upper level ethanol after completed sedimentation. Notice that the deposit body after the completion of sedimentation should always be below the drain outlet. The detachable pedestal provided convenience to take out the air-dried deposit for particle size analysis. The particle size distribution was characterized by a particle analyzer (Mastersizer 2000, Malvern). The morphology of aluminum particles was observed by the scanning electron microscope (SEM).

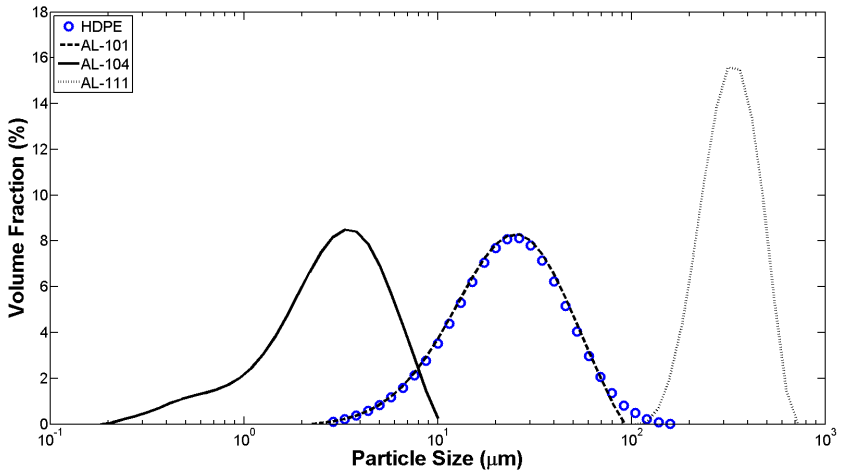

Figure 2.2.1: Particle size distribution of different types of aluminum and HDPE powders

2.2.2 Experimental Tests

The first experiment, which will be called the Al test (Al-T) later, was designed to measure the particle size distribution of deposit body at different depth. Although the particle size is continuously change in the range of 0.2 to 10 microns, for convenience of demonstration, the aluminum powder (Al-104) was divided into three groups, namely groups A, B and C, depending on particle size. In each group, some subgroups were divided for simulation. The size specifications were provided in Table 2.1.

In the mixing procedure, the 11.5 g aluminum powder was introduced into ethanol and

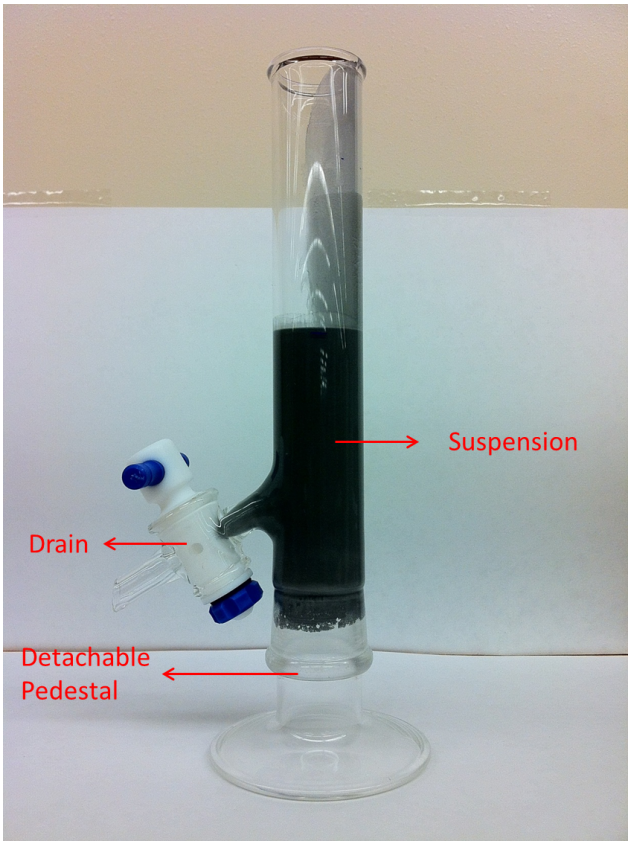

Figure 2.2.2: Sedimentation device with specification

well dispersed by ultrasonic devices for 10 minutes. After that, a mechanic mixer was used with mixing speed 500/s for 10 minutes. After mixing, the homogenous suspension was placed in the sedimentation device and started settling; the total height of suspension is 80 mm. Through sedimentation for 24 hours, more than 98% aluminum particles were completely settled; minor particles were still floating in the suspension above the deposition, which leads to the difference between the original and justified particle size distribution in Figure 2.2.3. The deposit body was obtained after discharging most the suspension by opening the drain and vaporing remaining ethanol out of the deposit body by air-dry for 6 hours.

The following steps were conducted for particle analysis: divide the aluminum deposit body equally into five layers along the thickness direction after fully-drying; number the layers in order from top to bottom; scratch out the powder layer by layer; and then analyze

Table 2.1: Details of particles in groups A, B and C with the maximum particle size specified

Group	A	B	C
Range of particle size (μm)	$r_a < 1.9$	$r_b = 1.9 \sim 3.8$	$r_c > 3.8$
Index of particle subgroup (i)		Particle size(μm)	
1	0.2089	2.1877	4.3651
2	0.2398	2.5118	5.0118
3	0.2754	2.8840	5.7543
4	0.3162	3.3113	6.6069
5	0.3630	3.8018	7.5857
6	0.4168		8.7096
7	0.4786		10
8	0.5495		
9	0.6309		
10	0.7244		
11	0.8317		
12	0.9549		
13	1.0964		
14	1.2589		
15	1.4454		
16	1.6595		
17	1.9054		

the particle size for each layer. The particle analyzer was used to measure the particle size distribution for each layer as shown in Figure 2.2.3. In addition, the SEM observations for layers 1 and 5 were shown in Figure 2.2.4, which were the top and bottom layers, respectively; it confirmed the test results from the particle analyzer, where the average particle size raised up from top to bottom. After the measurement by the particle analyzer, the volume fractions of group A, B and C for each layer were calculated and plotted later in Figure 2.4.1 of Section 2.4. The particle size distribution of original aluminum powder (Al-104) and justified aluminum powder, integral of 5 layers, were also plotted in Figure 2.2.3.

In addition, the interaction between aluminum powder and the solution is also important for FGM fabrication in this study. It has been mentioned on the International Chemistry Safety Card (ICSC) that aluminum powder in contact with water and ethanol may cause chemical danger. We have investigated the chemical reaction with special caution for the mixing and sedimentation process. In the literature, Streletskii et al. (2008) have also

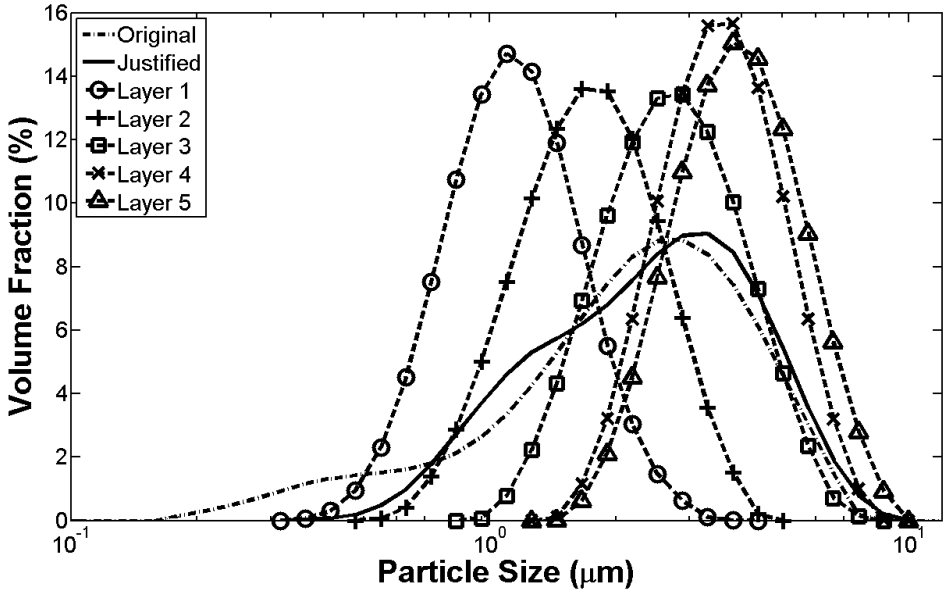

Figure 2.2.3: Particle size distribution of 5 different layers and original Al-104 powder

observed that aluminum ethoxide ($Al\,(C_2H_5O)_3$) and hydrogen were produced while nano-size aluminum particle reacted with ethanol under $90°C$. However, there is no obvious chemical reaction in our experiment with micron size of aluminum powder. Figures 2.2.4 and 2.2.5 show the microstructure of aluminum powder, which has been immersed in ethanol and water for 24 hours before the SEM observation. Aluminum oxide (Al_2O_3) produced by reaction between aluminum and water causes the hairy surface of particle as shown in Figure 2.2.5(a); whereas no obvious difference is observed between the original aluminum particles in Figure 2.2.5(b) and the particles placed in the ethanol for 24 hours in Figure 2.2.4. In our final manufacturing process, the mixing duration should be much less than one hour, so the chemical reaction will not be an issue.

Moreover, the second experiment, which will be called the FGM test (FGM-T) later, was developed to explore the volume fraction of aluminum along the depth direction of deposit body of Al and HDPE particles. To investigate the size effect of the Al particles on the gradation of the deposition, Al-101, Al-104, or Al-111 powders were used to be mixed with high-density polyethylene (HDPE) powder in the solution of ethanol. The solid loading

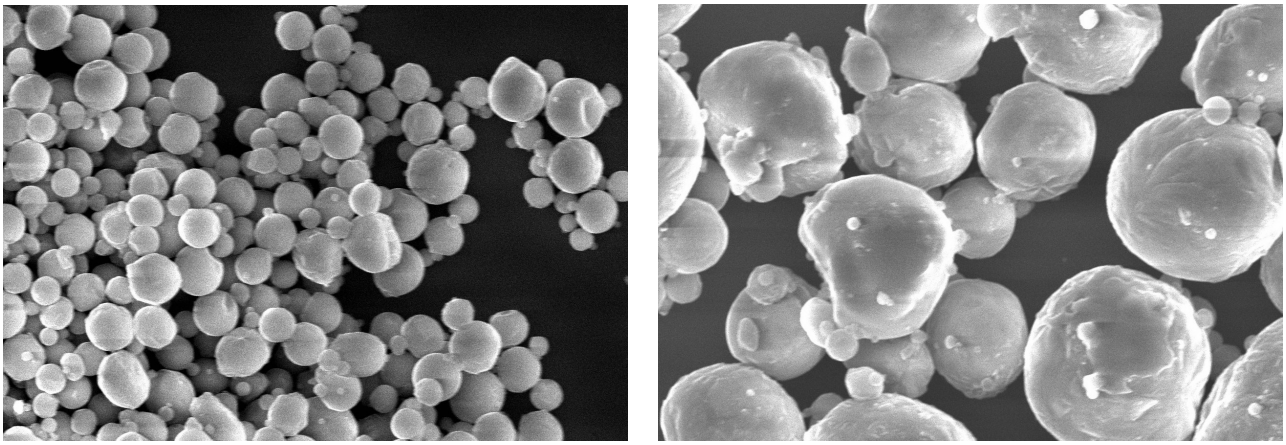

(a) (b)

Figure 2.2.4: SEM observations (7000x) for (a) top layer and (b) bottom layer of deposit body which settling in ethanol for 24 hours

of powders ($wt.\%$) and volume ratio of aluminum in mix were chosen as 20% and 25%, respectively, namely 7.29 g aluminum powders and 7.71 g HDPE powder prepared for the mixing in each test. The mixing procedure was applied as same as the Al-T method. After the mixing process, one hour sedimentation, and then 48 hours air-dry, the deposit body was also divided equally into five layers along the depth direction. It has been observed that a graded deposition was created for the cases of Al-101 and Al-104; whereas a bi-layered deposition was produced for Al-111. Dry powder of each layer was collected separately, and the Rice density measurement method was used to measure the density of mixed powder as a common and simple method to determine the volume fraction of aluminum in each layer.

2.3 Simulation and Modeling

To calculate the settling velocity of spherical aluminum particle in a viscous liquid, Stokes' law is used as:

$$V = \frac{2r^2 g\left(\rho_{particle} - \rho_{liquid}\right)}{9\eta} \tag{2.3.1}$$

where V, r, ρ, η and g are the settling velocity of particle, radius of particle, density, viscosity of liquid and acceleration of gravity, respectively. Yang et al. (2001) introduced

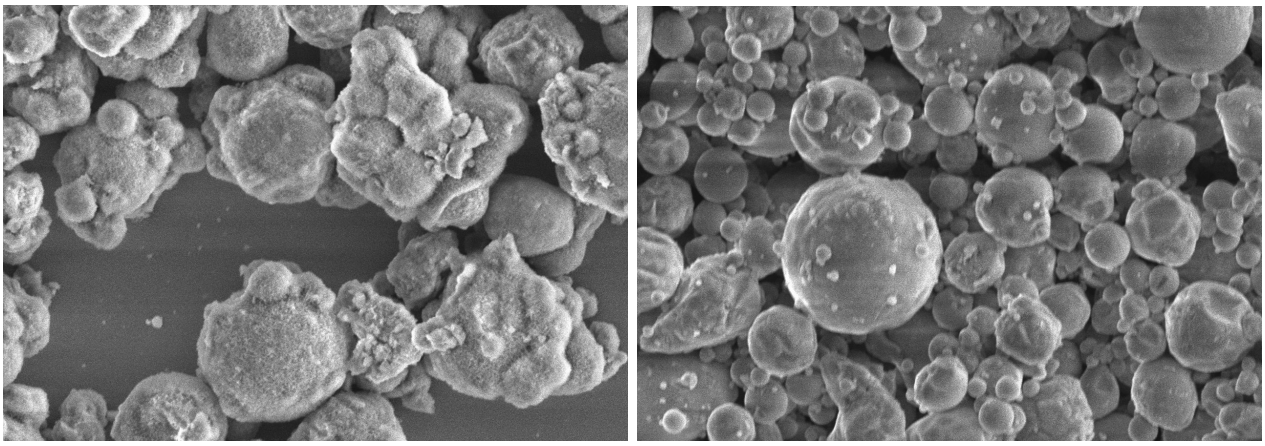

(a) (b)

Figure 2.2.5: SEM observations (7000x) for (a) aluminum powder immersing in water for 24 hours and (b) original Al-104 powder

the mathematical model based on Stokes' law to predict the compositional distribution of Ti-Mo system FGM. Because of the low volume ratio, which is only 0.6%, the viscosity of suspension is assumed as constant and not relative with concentration. Besides, consistent settling velocity of all particles is adopted in the whole simulation without consideration of acceleration. This model may provide reasonable prediction for dilute suspension with a large settling distance.

However, in the present work, the simulation will be based on the acceleration of particles with drag force which depends on solution concentration. A Stokes' law based numerical model, the discrete method dividing the mixed suspension into n sections and estimating the volume fraction of different groups (group A, B and C) or volume fraction of aluminum at any time with fixed time interval Δt, is derived and demonstrated for prediction of sedimentation behavior of aluminum particle. The major process and formula of discrete method for the Al-T measurements are introduced in this Section, which can be straightforwardly extended to the simulation of the FGM-T.

In the simulation, the suspension is evenly divided into n sections in the depth direction. The motion of particles and effective properties of the suspension are simulated and thus the microstructure of the deposition can be obtained when the sedimentation process is

completed.

2.3.1 Measurement of Initial Parameters and Conditions

To set up the initial condition for the sedimentation, the suspension in the cylinder is discretized into n sections in the depth direction. Because the suspension is thoroughly mixed, each section has uniform ϕ_a^0, ϕ_b^0 and ϕ_c^0, which are initial volume fraction of group A, B and C, as follows:

$$\begin{cases} \phi_a^0 &= \frac{F(r_{a,max})\cdot M_{AL}}{\rho_{AL}\cdot S\cdot h_{total}} \\ \phi_b^0 &= \frac{\left[F\left(r_{b,max}\right)-F(r_{a,max})\right]\cdot M_{AL}}{\rho_{AL}\cdot S\cdot h_{total}} \\ \phi_c^0 &= \frac{\left[F(r_{c,max})-F\left(r_{b,max}\right)\right]\cdot M_{AL}}{\rho_{AL}\cdot S\cdot h_{total}} \end{cases} \tag{2.3.2}$$

where M_{AL} and ρ_{AL} are total mass of aluminum powder and density of aluminum, respectively. Here $\rho_{AL} = 2.699\ g/cm^3$.

The number and size of particles in each group are shown in Table 2.1. The relationship of volume fraction between particles and groups can be described as

$$\begin{cases} \phi_a^0 &= \sum_{k=1}^{n}\sum_{i=1}\phi_{a,i,k}^0 \\ \phi_b^0 &= \sum_{k=1}^{n}\sum_{i=1}\phi_{b,i,k}^0 \\ \phi_c^0 &= \sum_{k=1}^{n}\sum_{i=1}\phi_{c,i,k}^0 \end{cases} \tag{2.3.3}$$

$$\phi_{total,k}^j = \phi_{a,k}^j + \phi_{b,k}^j + \phi_{c,k}^j = \sum_{i=1}^{max}\left(\phi_{a,i,k}^j + \phi_{b,i,k}^j + \phi_{c,i,k}^j\right) \tag{2.3.4}$$

where $\phi_{a,i,k}^0$ refers to the initial volume fraction of each particle index i of group A at section k. The superscript, first, second and third subscripts represent number of time period, name of group, index of particles and number of sections, respectively. Besides, $\phi_{a,k}^j$, the summation of $\phi_{a,i,k}^j$, is the volume fraction of all particles of group A at section k during time period j. The initial total volume fraction of each group, $\phi_{a,k}^0$, $\phi_{b,k}^0$ and $\phi_{c,k}^0$, should be all uniform ($\phi_{a,1}^0 = \phi_{a,2}^0 = ... = \phi_{a,n}^0$) in the different sections as for the uniformly dispersed

mixture.

2.3.2 Corresponding Viscosity η

The viscosity of suspensions varies with the volume fraction of suspended particle. The effective viscosity can be estimated by the self-consistent method as (Yin and Lai, 2012)

$$\overline{\eta} = \frac{\eta_0}{1 - 2.5\phi} \tag{2.3.5}$$

where $\overline{\eta}$, η_0 and ϕ are effective viscosity of suspension, viscosity of the matrix fluid and volume fraction of the suspended particle, respectively.

To consider the three size groups of particles, η_k^j, the effective viscosity of solution in section k during time period j, is calculated by three steps in sequence as follows:

$$\begin{cases} \eta_{1,k}^j &= \dfrac{\eta_0}{1-2.5\left(\frac{\phi_{a,k}^j}{1-\phi_{b,k}^j-\phi_{c,k}^j}\right)} \\ \eta_{2,k}^j &= \dfrac{\eta_{1,k}^j}{1-2.5\left(\frac{\phi_{b,k}^j}{1-\phi_{c,k}^j}\right)} \\ \eta_{3,k}^j &= \dfrac{\eta_{2,k}^j}{1-2.5\left(\phi_{c,k}^j\right)} \end{cases} \tag{2.3.6}$$

These three steps in Eq.(2.3.6) are used to solved $\eta_{3,k}^j$ which is treated as η_k^j and applied for determination of settling velocity and distance for every identical i in the whole analysis. Eq.(2.3.6) is introduced under following assumption: At first, the finest particles (group A) were placed into ethanol; $\eta_{1,k}^j$ was the effectively viscosity of the suspension which only included particle of group A. Then, we treated the suspension only with particle of group A as the matrix liquid; $\eta_{2,k}^j$ is solved by these known parameters. Finally, the second step was repeatedly employed; the suspension with particles of group A and B is treated as the matrix liquid for the particle of group C, $\eta_{3,k}^j$ and is obtained. The initial volume fractions, $\phi_{a,k}^0$, $\phi_{b,k}^0$ and $\phi_{c,k}^0$, are obtained from Eqs.(2.3.2) ~ (2.3.4); updating volume fractions with

varied time period, $\phi^j_{a,k}$, $\phi^j_{b,k}$ and $\phi^j_{c,k}$ are calculated from Eqs.(2.3.7) ~ (2.3.11).

Notice that there is a limit to the Eq.(2.3.5) while $\phi \to 0.4$ which causes that the effective viscosity approaches infinity. However, it is not realistic because the suspension with 40% particle should still flow. It has also been confirmed in the experiments that the maximum volume fraction ϕ_{max} is commonly more than 0.4. Fortunately, with the homogenization of particles with different sizes in Eq.(2.3.6), the overall volume fraction of the aluminum particles can be over 0.4.

2.3.3 Time-dependent ϕ

As times goes by, all the aluminum particles will fall down; it causes the reduction of concentration and viscosity in upper sections and the increments in lower sections. According to the Stokes' law, Eq.(2.3.7) shows the acceleration of settling spherical particle.

$$a = \frac{F_g - F_d}{m} = \frac{4\pi r^3 g\left(\rho_p - \rho_l\right) - 6\pi\eta r V}{3m} \tag{2.3.7}$$

where F_g, F_d, ρ_p, ρ_l and m are gravitational force combined with buoyant force, drag force, density of aluminum particle, density of ethanol and mass of single aluminum particle, respectively. Settling distance of identical particle X from time period j to $j+1$ (time interval $= \Delta t$) can be estimated in Eq.(2.3.8) by considering of acceleration. Coefficient m, the ratio of settling distance to height of section Δh, is relative with X and solved in Eq.(2.3.9).

$$X^j_{a,i,k} = V^j_{a,i,k} \cdot \Delta t + \frac{1}{2} a^j_{a,i,k} \left(\Delta t\right)^2 \tag{2.3.8}$$

$$m^j_{a,i,k} = \frac{X^j_{a,i,k}}{\Delta h} \tag{2.3.9}$$

Thus, for group A, the corresponding volume fraction of identical particle i in section k at $t = j$ can be calculated as below

$$\begin{cases} \phi^j_{a,i,k+\beta,I} &= \left(\gamma - m^j_{a,i,k}\right) \cdot \phi^j_{a,i,k} \\ \phi^j_{a,i,k+\gamma,II} &= \left(m^j_{a,i,k} - \beta\right) \cdot \phi^j_{a,i,k} \end{cases} \quad \text{if } k + \gamma \leq k_{max} \tag{2.3.10}$$

$$\begin{cases} \phi^j_{a,i,k_{max},I} &= \sum_k^{k_{max}} \left(\gamma - m^j_{a,i,k}\right) \cdot \phi^j_{a,i,k} \\ \phi^j_{a,i,k_{max},II} &= \sum_k^{k_{max}} \left(m^j_{a,i,k} - \beta\right) \cdot \phi^j_{a,i,k} \end{cases} \quad \text{if } k + \gamma > k_{max} \tag{2.3.11}$$

$$\phi^{j+1}_{a,i,k} = \phi^j_{a,i,k,I} + \phi^j_{a,i,k,II} \quad \text{for } k = 1 \sim n \tag{2.3.12}$$

where γ and β rounds the elements of $m^j_{a,i,k}$ to the nearest integers greater and less than $m^j_{a,i,k}$, respectively. The solutions of volume fraction from Eqs.(2.3.10) ~ (2.3.12) are also adopted for groups B and C. The corresponding total concentration in each section at following period of time is obtained by substituting Eq.(2.3.12) into Eq.(2.3.4).

2.3.4 Translation Velocity

Base on Newton's second law of motion and Stokes' law, the settling particle in viscous liquid will reach terminal velocity at very short times; however, this phenomenon only happens for a dilute suspension system, which means that the viscosity of liquid is consistent at any time. In both experiment and simulation, the viscosity of suspension in each section changes caused by the variation of concentration as time goes by. Thus, the settling velocity of every aluminum particle will keep changing slightly even during the end of the whole sedimentation process.

In the process of modeling, each section was treated as a unit where identical aluminum particle only have one settling velocity during a time period j. Besides, settling velocity of

identical particle during time period $j+1$ satisfies the conservation of momentum as follows:

$$V_{a,i,k}^{j+1} = P_{a,i,k}^{j+1} / M_{a,i,k}^{j+1} \tag{2.3.13}$$

where $V_{a,i,k}^{j+1}$, $P_{a,i,k}^{j+1}$ and $M_{a,i,k}^{j+1}$ are settling velocity of particle, total momentum and total mass of identical particle i (belong to group A) located in section k during time period $j+1$, respectively.

The total momentum $P_{a,i,k}^{j+1}$ is contributed by two partial momentum, $P_{a,i,k,I}^{j+1}$ and $P_{a,i,k,II}^{j+1}$, and described as:

$$P_{a,i,k}^{j+1} = P_{a,i,k,I}^{j+1} + P_{a,i,k,II}^{j+1} = M_{a,i,k,I}^{j+1} \cdot V_{a,i,k,I}^{j+1} + M_{a,i,k,II}^{j+1} \cdot V_{a,i,k,II}^{j+1} \tag{2.3.14}$$

where $V_{a,i,k,I}^{j+1}$ and $V_{a,i,k,II}^{j+1}$ are corresponding velocity of mass $M_{a,i,k,I}^{j+1}$ and $M_{a,i,k,II}^{j+1}$.

These two partial momentums can be written in terms of the velocity of particle during time period j, $V_{a,i,k}^{j}$, and the relationship are:

$$\begin{cases} P_{a,i,k+\beta,I}^{j+1} = M_{a,i,k+\beta,I}^{j+1} \cdot V_{a,i,k+\beta,I}^{j+1} = \left(\gamma - m_{a,i,k}^{j}\right) \cdot \phi_{a,i,k}^{j} \cdot {V_{a,i,k}^{j}}' \\ P_{a,i,k+\gamma,II}^{j+1} = M_{a,i,k+\gamma,II}^{j+1} \cdot V_{a,i,k+\gamma,II}^{j+1} = \left(m_{a,i,k}^{j} - \beta\right) \cdot \phi_{a,i,k}^{j} \cdot {V_{a,i,k}^{j}}' \end{cases} \tag{2.3.15}$$

and

$${V_{a,i,k}^{j}}' = V_{a,i,k}^{j} + a_{a,i,k}^{j} \cdot \Delta t \tag{2.3.16}$$

Combined with two corresponding partial momentum $P_{a,i,k,I}^{j+1}$ and $P_{a,i,k,II}^{j+1}$ from Eqs.(2.3.14) ~ (2.3.16), the new settling velocity of identical particle during time period $j+1$ is obtained by Eq.(2.3.13) and placed into Eq.(2.3.7) to solve the new acceleration $a_{a,i,k}^{j+1}$. Thus, final volume fraction of each group along the thickness direction in deposition will be determined by repeating Eqs.(2.3.7) ~ (2.3.16) with time-dependent viscosity of liquid, η_k^j, which is calculated by Eq.(2.3.6); furthermore, each section of deposition is assumed fully-packed while the total volume fraction $\phi_{total,k}^{j}$ is equal to 0.5 - the value observed by comparison of

total thickness of deposition between experimental and ideal results.

This proposed model can also be applicable for the FGM-T test. The only changes of input parameters in simulations are: (1) there are only two groups, aluminum and HDPE respectively; (2) the densities of these two powders are different.

2.4 Results and Discussions

The numerical modeling is based on Stokes' law, which is applicable for the laminar flow. To determine whether the sedimentation process is still in the range of a Stokes flow, we calculate the maximum Reynolds number (Re) of the whole system based on the dilute suspension formulation as follows:

$$\begin{aligned} V_{cr} &= \frac{2r_{cr}^2 g(\rho_p - \rho_l)}{9\eta_l} = \frac{2\times\left(32.74\times10^{-6}\right)^2\times9.81\times(2.699-0.789)\times10^3}{9\times1.074\times10^{-3}} \\ &= 4.16\times10^{-3} \quad m/s \end{aligned} \tag{2.4.1}$$

and

$$Re = \frac{\rho_l \cdot V_{cr} \cdot d_{cr}}{\eta_l} = \frac{0.7892\times10^3\times4.16\times10^{-3}\times65.48\times10^{-6}}{1.074\times10^{-3}} = 0.2 \tag{2.4.2}$$

where V_{cr} and r_{cr} (d_{cr}) are the settling velocity and the radius(diameter) of particle with critical size; and η_l is the viscosity of pure ethanol. Shabestari et al. (1995) verified that the whole system is under laminar flow if the Reynolds number (Re) of is less than 0.2. Based on this, the critical particle size d_{cr} is 65.48 microns using the Eqs.(2.4.1) and (2.4.2); laminar flow will happens for an aluminum particle settling in ethanol if the size is smaller than critical particle size. For all particles and about 97% particles in the group of Al-104 and Al-101 are, respectively, smaller than critical particle size. Therefore, Stokes' law could be applied in numerical modeling for these two cases of FGM-T test, containing Al-101 and Al-104, as well as Al-T test. Notice that in actual experiments, the particles may not be able to reach the critical velocity in Eq.(2.4.1) due to the change of effective viscosity and

density, so the actual critical particle size can be higher than 65.48 microns.

For the Al-T test only containing aluminum powder, Figure 2.4.1 shows the numerical simulation results using the sedimentation configuration in Section 2.2. The proportion distribution of each group, say Group A, B, or C, in the depth direction from the bottom to the top is illustrated with a curve, which well compares with the experimental data shown with circles. Obviously, at the top the small particles of Group A are dominated; whereas at the bottom the large particles of Group C are the majority as observed in Figure 2.2.4. In Figure 2.4.1(a), the proportion of Group A particles gradually increases from the bottom to the top. The numerical results slightly overestimate the experimental results. In Figure 2.4.1(b), the proportion of the medium size of Group B particles increases first, reaches a maximum, and then decreases. Both the experiments and the numerical simulation show the same trend but the simulation results amplify the variation. Figure 2.4.1(c) shows the proportion of the large size of Group C particles decreases from the bottom to the top. Notice that in the experiments, only five layers are measured and the average values are used. The variation of the experimental results could be higher if more layers can be accurately measured. However, considering the resolution of our instrument and our test procedure, we choose five layers in the present experiments balancing the workability and accuracy.

In the sedimentation process, the parameters, such as height of suspension, particle size distribution, density of particle and matrix liquid, play important roles to affect vertical compositional distribution of final deposition. The understanding of the correlation among these parameters and the end results of the FGM will extremely important for the material design and optimization. The present numerical simulation and modeling framework provides a very valuable tool to reveal the correlations.

Given a set of material, the volumetric design of the sedimentation may change the end results. Figure 2.4.2 illustrates the effects of the suspension height on volume fraction distribution of each group in the depth direction. Using the same aluminum-ethanol suspension as the one in experiments, two more cases of suspension height 40mm and 160mm, respec-

tively, are considered. The sedimentation processes can be simulated in the computer; upon the completion of sedimentation, the final proportion distributions in the depth direction of the three groups A, B, and C are illustrated in Figures 2.4.2 (a), (b), and (c), respectively. Although the proportion distributions for the three cases follow the same trends, the proportion variation of the three groups A, B, and C in the depth direction is considerably lower for the height of 40 mm compared with that for 160 mm. Therefore, the lower the suspension height, the smaller the material gradation.

Furthermore, the proposed numerical model has been extended to the FGM-T tests, which contain three types of aluminum powders mixed with HDPE powder into ethanol, to simulate the volume fraction of aluminum particles along the depth direction of deposit body.

Figure 2.4.3(a) illustrates the volume fraction of Al changing along the depth of the deposition for the case of Al-104. The simulation results show that the volume fraction of aluminum increases from the bottom to the top because the size of HDPE is much larger than Al particles, which causes higher settling speed. However, the experiments show that volume fraction of Al particles starts high at the bottom, reduces to a minimum in the middle, and then increases again at the top. In addition, the distribution curves vary significantly in the replicates. This implies the instability of sedimentation process for this set of mixture. Because the higher density of Al may cause the higher settling speed but the smaller size of Al particles causes lower settling speed, other factors, such as the effective density and viscosity, may produce significant effect on the sedimentation process. In general, the HDPE particles may first settle faster than aluminum particles and deposit in the bottom layer; then it may start floating because of the effective density of ethanol increases caused by the concentration of aluminum powders. Moreover, the finer aluminum particles could infiltrate through the bigger particles of HDPE even though the deposit body is almost packed. Therefore, the proposed model may not fully take into account of these factors. It is observed that the experimental volume fraction of aluminum in the bottom layer is always higher theoretical

results. Future investigation of these factors is underway.

Figure 2.4.3(b) illustrates the results for cases of Al-101 and Al-111, which exhibit good agreement between the experiments and the modeling results. Notice that because the case of Al-111 simply exhibits a bi-layered microstructure of the deposition and the Reynolds number of the particle sedimentation may also be higher than 0.2, the modeling results may be trivial for this case. However, when the solid load is higher in the suspension, the above trend will be significantly changed, which is still under the investigation. For the case of Al-101, both Al and HDPE particles fall in the same size range and their motion in the ethanol belongs to laminar flow, very good agreement between the modeling and experimental results is observed.

Based on the present modeling and experimental results, it is demonstrated that the sedimentation process can successfully produce graded mixtures of Al and HDPE particles, which will be used to fabricate Al-HDPE functionally graded materials. Future research is to investigate workability for sedimentation process with higher solid load, so as to scale up the manufacture process for mass production of solar roofing panels.

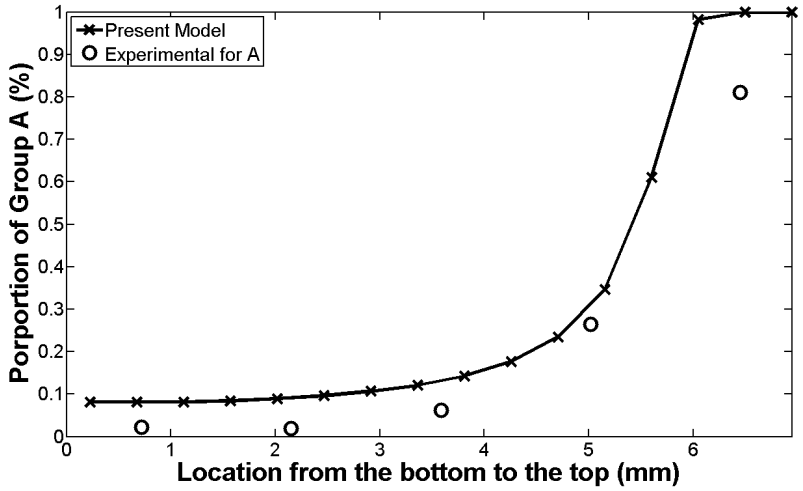

(a)

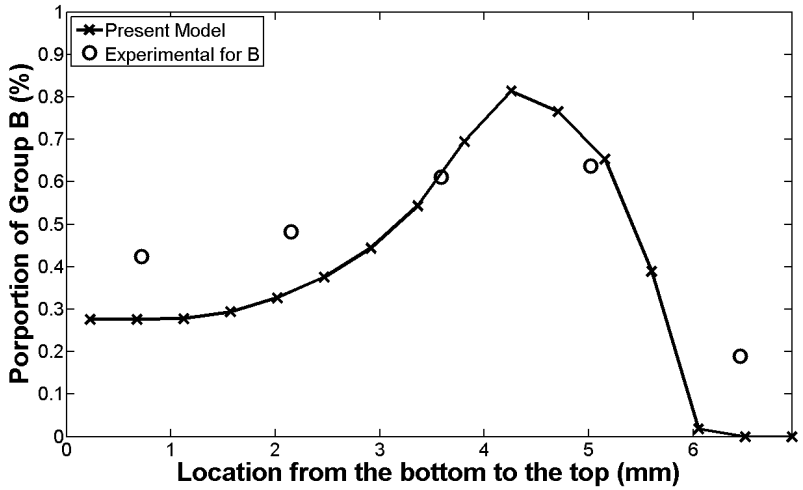

(b)

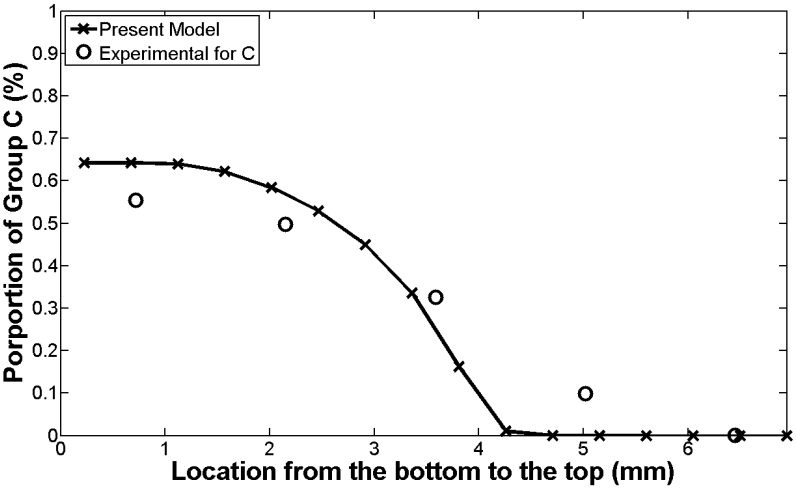

(c)

Figure 2.4.1: Comparison between experimental and theoretical results for proportion of (a) group A ($r_a < 1.9\,\mu m$), (b) group B ($1.9 \leq r_b \leq 3.8\,\mu m$) and (c) group C ($r_c > 3.8\,\mu m$) at location from the bottom to the top

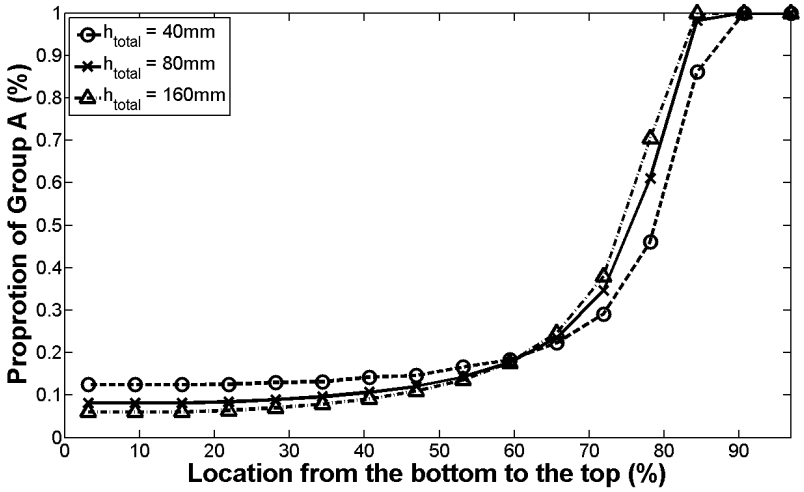

(a)

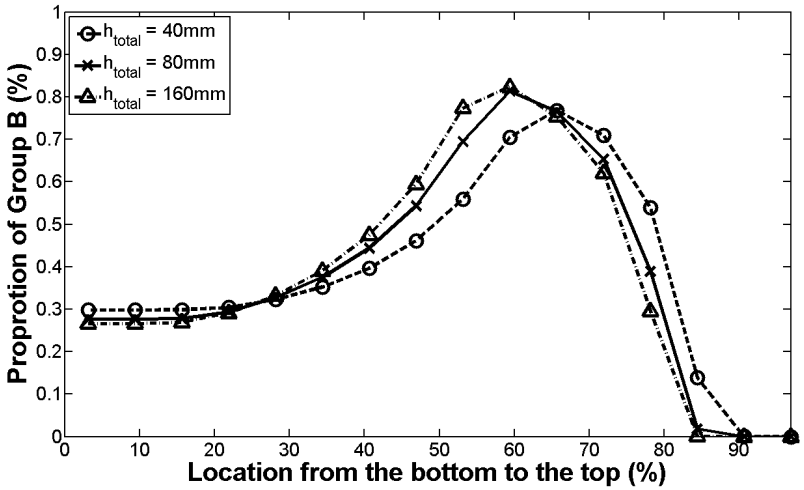

(b)

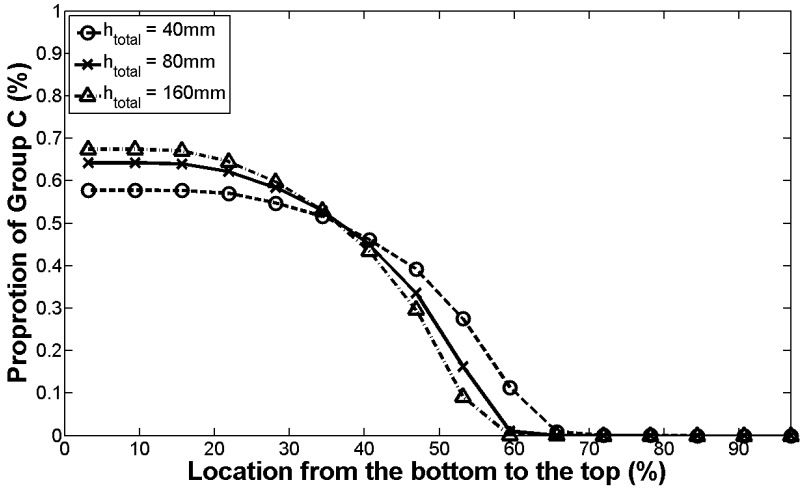

(c)

Figure 2.4.2: Theoretical compositional distribution of each group at location from the bottom to the top from present model when total height of suspension is (a) 40 mm; (b) 80 mm and (c) 160 mm

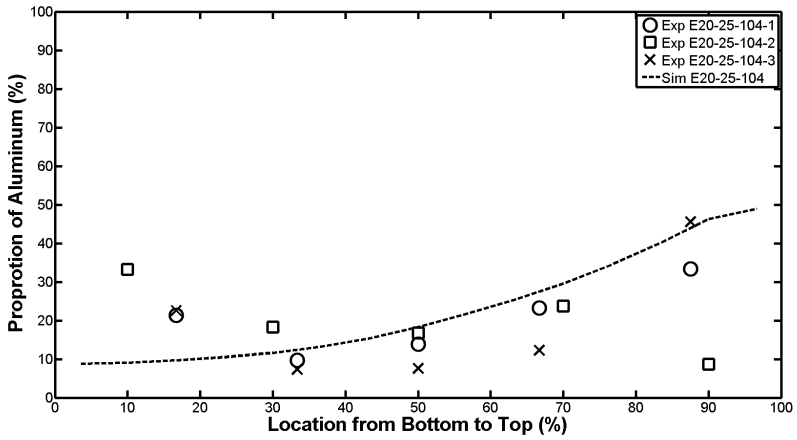

(a)

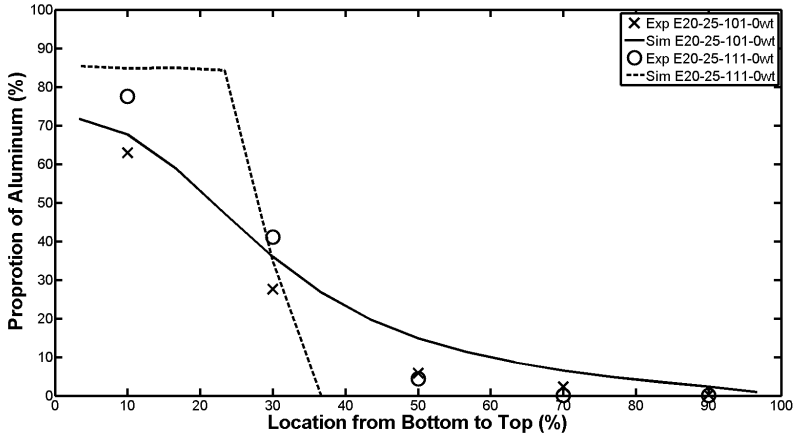

(b)

Figure 2.4.3: Comparison between experimental and theoretical result for volume fraction of aluminum at location from the bottom to the top in the case of: (a) Al-104 + HDPE; (b) Al-101 or Al-111 + HDPE

Chapter 3

Sedimentation Behavior of a Single Ellipsoidal Drop

An approach based on Eshelby's equivalent inclusion method is presented to derive the Stokes flow of an ellipsoidal drop moving in a Newtonian fluid at small Reynolds number. The inclusion problem is first introduced that the drop with the same material properties as the fluid is subjected to a body force and a fictitious non-mechanical strain rate, which is called eigenstrain rate. Then the original problem is solved by the equivalent inclusion method, in which the drop is replaced with an inclusion but an eigenstrain rate is introduced to represent the mismatch between the drop and the rest fluid. The drag force on the drop is obtained by the integral of the distributed body force over the drop volume bypassing the boundary integral of the stress distribution on the particle surface. This chapter demonstrates the theoretical framework of this method considering one drop moving in a Newtonian fluid. When the drop is spherical, the solution recovers the closed form classic solution for a drop moving in a fluid. This method is general and can be applicable to the cases of different

shapes of drops and the interaction between multiple drops.

3.1 Overview

In the viscous fluid of small Reynolds number Re, the inertia forces may be disregarded in the Navier-Stokes equation, which becomes the Stokes equation; and the motion of a falling spherical object will reach the terminal velocity rapidly, where the drag (frictional) force and the driving (say buoyant and gravitational) force are exactly balanced. For a rigid sphere moving in a liquid, the drag force is written in Eq.(1.2.4). This formulation is well known as Stokes' law to determine the frictional force of a moving solid sphere caused by the viscosity of the liquid (Batchelor, 1967). As for a spherical drop moving in a different fluid, such as a gas bubble or insoluble drop, the drag force has been derived in the similar fashion (Batchelor, 1967). In addition, the drag force of other shapes of objects moving through liquid has also been investigated, such as ellipsoid and circular disk (Lamb, 1975). In the above cases, due to condition of the small Re, the governing equations could be simplified and vorticity field and stream function will be solved. Consequently, the stress vector on the surface is obtained, and the drag force is determined by the integral of surface force.

A closed-form solution to an ellipsoidal drop moving in a different fluid with a no-slip interface at a small Reynolds number is derived. In case of a Stokes flow, the hydrodynamic Green's function is the Stokeslet, which is the fundamental solution of the Stokes equation. For a point in the viscous liquid applied with a concentrated force $\mathbf{F}$, the velocity field $\mathbf{v}$ caused by the force could be written in terms of the Stokeslet as

$$v_i(x) = G_{ij} F_j \tag{3.1.1}$$

where G_{ij} is the hydrodynamic Green's function, also known as the Oseen-Burgers tensor, as follows

$$G_{ij} = \frac{1}{4\pi\mu}\left[\frac{\delta_{ij}}{|x-x'|} - \frac{1}{2}\frac{\partial^2 |x-x'|}{\partial x_i \partial x_j}\right] \tag{3.1.2}$$

The hydrodynamic Green's function has been derived by several different methods as follows. Kim and Karilla (1991) have developed the solution of the Stokeslet by making use of the linearity of the Stokes equations and symmetries of the system with the Fourier transform. Also, basing on the linearity of the Stokes equations, a physical approach has been derived by Dhont (1996). Zapryanov and Tabakova (1998) took the divergence of Stokes equation, and applied the Fourier transform and the fundamental solution of the Laplace equation to solve the Stokeslet. The Stokeslet will be essential for the derivation in this work, which is also called the Green's function.

This chapter presents a new approach to derive the drag force using Eshelby's equivalent inclusion method (EIM). Eshelby (1957; 1959) firstly studied the stress for an inhomogeneity in an infinite matrix under a uniform far field stress and proposed that the stress disturbance caused by the inhomogeneity could be simulated by an inclusion with the same material properties as the matrix but with a appropriately chosen eigenstrain. This method is coined as Eshelby's equivalent inclusion method (EIM). The beauty of this method is that the eigenstrain is a constant when the inhomogeneity is ellipsoidal. The EIM is not only valuable for the effective elastic moduli of composite (Y. Takao et al., 1982; Chen and Cheng, 1996; Yin et al., 2008a), it but also successfully applied for the prediction of thermal and electric behavior of composite, e.g., work-harden rate (Huang, 1996), thermal steady-state heat conduction (Hatta and Taya, 1986) and thermal expansion coefficient (Takei et al., 1991a,b; Sakata et al., 2010) and electroelastic moduli (Dunn and Taya, 1993). In the elastic problem of infinite domain containing inhomogeneity, the overall elastic fields, stress, strain and displacement field are the summation of far field and disturbed elastic field. The elastic Green's function provides the connection between disturbed strain field and eigenstrain of the equivalent inclusion; the EIM is used to link the eigenstrain of the equivalent inclusion and far field strain field together (Mura, 1987).

The EIM has not been used in problems of fluid mechanics yet. Although a fluid has distinct material behavior from a solid, the mathematical formulation is very similar. The

main difficulty to use the concept of EIM for a drop moving in a different fluid is that not only is the material property of the drop different from the matrix fluid, but also a driving force is applied on the drop. This thesis successfully extends the EIM to the above-mentioned problem and formulates the velocity and stress fields in the fluid.

When a drop moves at a constant velocity in an infinite domain of a different liquid, the driving force, such as gravity or buoyancy, will be exactly balanced by the drag force from the viscous fluid. Therefore, given a driving force, if the terminal velocity can be determined, the correlation between the velocity and the drag force can also be obtained from the relationship of the velocity and the driving force. Therefore, the drag force can be directly obtained by the driving force bypassing the boundary integral of the stress vector over the drop surface.

To find the correlation between the driving force and the terminal velocity, the EIM with a continuous boundary condition will be used. If the drop has the same viscosity as the fluid, the motion of the drop and the distributed driving force can be directly written in terms of the integral of Eq.(3.1.1) over the volume of the drop. However, due to the difference of viscosities between the fluid and the drop, the motion of the drop will surely be different. Using the EIM, the viscosity mismatch between the drop and the fluid can be simulated by introducing an eigenstrain rate. Then the overall velocity field will be written in terms of the combination of the velocity field caused by the driving force and the velocity field caused by the eigenstrain rate.

The method is general and can be extended to a many-particle system by numerical methods (Lee et al., 2013). This chapter introduces the theoretical framework of the equivalent inclusion method and provides the analytical solution for an ellipsoidal drop moving in a different fluid. The remainder of this chapter is organized as follows: Section 3.2 introduces the inclusion problem for one ellipsoidal inclusion in an infinite medium subjected to a body force and eigenstrain rate. Section 3.3 formulates the EIM problem for an ellipsoidal drop moving in a viscous fluid and derives the correlation between the driving force and the

velocity. Finally, Section 3.4 demonstrates the solution for a spheroidal drop and presents closed form solutions for the case of a spherical drop, solid particle, and air void, which is consistent with the classic solution. The interfacial continuity of the surface stress vector and velocity is also discussed.

3.2 The Inclusion Problem

Extending Mura's definition (1987) to a fluid system, an inclusion in an infinite homogeneous fluid D is defined as a subdomain Ω, where an eigenstrain rate $e^*_{ij}(\mathbf{x})$ or a body force $f_i(\mathbf{x})$ is applied on Ω but is zero on $D-\Omega$. The viscous properties of the fluids in the inclusion and the rest (matrix) are the same. This term of inclusion is to differentiate another counterpart - inhomogeneity. An inhomogeneity is a subdomain in a homogenous fluid with different material properties from the rest. In the following of this section, we focus on the inclusion problem first.

Consider a ellipsoidal inclusion Ω moving in a homogeneous fluid as Figure 3.2.1, where the ellipsoidal inclusion is defined by the function $\frac{x_1^2}{a_1^2}+\frac{x_2^2}{a_2^2}+\frac{x_3^2}{a_3^2}\leq 1$ with a_i $(i=1,2,3)$ being the three principal half axes of the ellipsoid. The viscosity is same in the inclusion and the matrix, written as μ_0. A body force $f_i(\mathbf{x})$ and an eigenstrain $e^*_{ij}(\mathbf{x})$ are distributed on the particle, but are zero in the matrix.

The stress σ_{ij} in any position $\mathbf{x}$ can be expressed as

$$\sigma_{ij} = -p\delta_{ij} + 2\mu_0\left(e_{ij} - e^*_{ij}\right) \tag{3.2.1}$$

where the strain rate reads

$$e_{ij} = \frac{1}{2}\left(v_{i,j} + v_{j,i}\right) \tag{3.2.2}$$

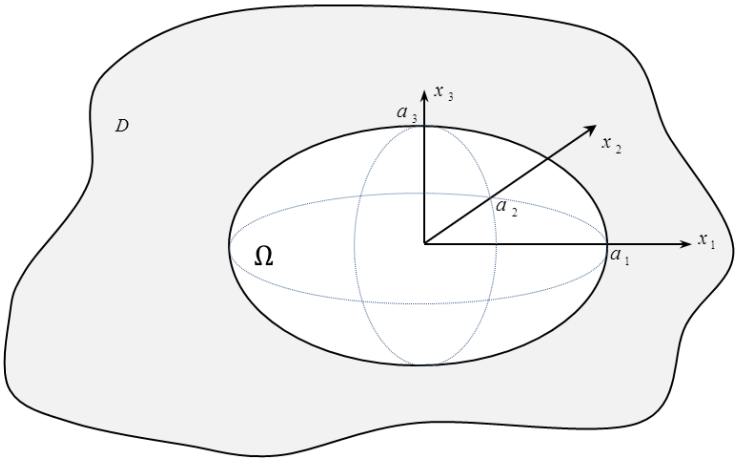

Figure 3.2.1: One ellipsoidal subdomain Ω embedded in the infinite domain D

Both e_{ij} and e^*_{ij} satisfy the mass conservation respectively as

$$e_{ii} = 0; \text{ and } e^*_{ii} = 0 \tag{3.2.3}$$

Using Eq.(3.2.1) in the equilibrium equation, one can obtain the equation of motion, written as

$$2\mu_0 e_{ij,i} - p_{,j} = -f_i(\mathbf{x}) + 2\mu_0 e^*_{ij,i}(\mathbf{x}), \qquad v_{i,i} = 0, \quad \mathbf{x} \in \Omega \tag{3.2.4}$$

and

$$2\mu_0 e_{ij,i} - p_{,j} = 0, \qquad v_{i,i} = 0, \quad \mathbf{x} \in D - \Omega \tag{3.2.5}$$

Notice that outside the inclusion, the equation of motion also reads the Stokes' equation by substituting Eq.(3.2.2) into it. The velocity and pressure fields in this inclusion problem is caused by two sources: the body force and the eigenstrain rate on the right-hand side of Eq.(3.2.4) in the inclusion domain Ω.

Using the Green's function technique (Yin et al., 2006), one can write the velocity and pressure fields in the domain D in terms of the integrals of the eigenstrain rate e^*_{ij} and the

applied force f_i with the tensorial Green's function $\mathbf{G}$ as follows:

$$v_i(\mathbf{x}) = \int_D \left[G_{ik}\left(\mathbf{x},\mathbf{x}'\right) f_k\left(\mathbf{x}'\right) - 2\mu_0 G_{im}\left(\mathbf{x},\mathbf{x}'\right) \frac{\partial e^*_{mn}\left(\mathbf{x}'\right)}{\partial x'_n} \right] d\mathbf{x}' \tag{3.2.6}$$

and

$$p(\mathbf{x}) = -\frac{1}{4\pi} \int_D \left[\frac{\partial \phi}{\partial x_k} f_k - 2\mu_0 \frac{\partial \phi}{\partial x_m} \frac{\partial e^*_{mn}\left(\mathbf{x}'\right)}{\partial x'_n} \right] d\mathbf{x}' \tag{3.2.7}$$

where

$$\phi\left(\mathbf{x},\mathbf{x}'\right) = \frac{1}{|\mathbf{x}-\mathbf{x}'|}, \qquad \psi\left(\mathbf{x},\mathbf{x}'\right) = |\mathbf{x}-\mathbf{x}'| \tag{3.2.8}$$

and the tensorial Green's function is written as

$$G_{ij}\left(\mathbf{x},\mathbf{x}'\right) = \frac{1}{4\pi\mu_0} \left(\delta_{ij}\phi - \frac{1}{2} \frac{\partial^2 \psi}{\partial x_i \partial x_j} \right) \tag{3.2.9}$$

which is the same as the Stokeslet in Eq.(3.1.2). The detailed derivation of Eqs.(3.2.6) and (3.2.7) is given in Appendix B.

Using the Gauss' theorem, Eqs.(3.2.6) and (3.2.7) can be rewritten as

$$v_i(\mathbf{x}) = \int_\Omega \left(G_{ik} f_k - 2\mu_0 G_{im,n} e^*_{mn} \right) \, d\mathbf{x}' \tag{3.2.10}$$

and

$$p(\mathbf{x}) = -\frac{1}{4\pi} \int_\Omega \left(\phi_{,k} f_k - 2\mu_0 \phi_{,mn} e^*_{mn} \right) \, d\mathbf{x}' \tag{3.2.11}$$

where the eigenstrain rate in the far field $e^*_{mn} = 0$ is used. Notice that Eq.(3.2.11) implies the far field pressure is zero. For the case a uniform pressure exists, a constant term of the pressure will be superposed. Because $e^*_{mn} = e^*_{nm}$, using the concept of the modified Green's function (Kroner, 1990), onecan rewrite Eq.(3.2.10) as

$$v_i(\mathbf{x}) = \int_\Omega G_{ik} f_k - \mu_0 \Gamma_{imn} e^*_{mn} \, d\mathbf{x}' \tag{3.2.12}$$

where

$$\Gamma_{imn} = G_{im,n} + G_{in,m} \tag{3.2.13}$$

In the ellipsoidal domain, the body force and the eigenstrain rate are generally continuously distributed, so that they can be written in the polynomial form using the Taylor's expansion. Then the integral in Eqs.(3.2.10) and (3.2.11) can be explicitly written with the aid of the identities of the integral of ϕ and ψ (Mura, 1987; Yin et al., 2006; Yin and Sun, 2006). Appendix C has provided those identities which may be needed in this chapter.

3.3 The Equivalent Inclusion Method

Consider a ellipsoidal drop Ω moving in a homogeneous fluid as Figure 3.2.1, where the ellipsoidal drop is an inhomogeneity. The viscosity is constant in the drop and the fluid, written as μ_1 and μ_0, respectively. A driving force is uniformly distributed on the particle, written as

$$f_i(\mathbf{x}) = \begin{cases} f_i^0 & \mathbf{x} \in \Omega \\ 0 & \mathbf{x} \in D - \Omega \end{cases} \tag{3.3.1}$$

The Stokes equation is written as

$$2\mu_0 e_{ij,i} - p_{,j} = 0, \qquad v_{i,i} = 0, \qquad \mathbf{x} \in D - \Omega \tag{3.3.2}$$

On the drop, the driving force $f_i(\mathbf{x})$ makes it move in the fluid. The Stokes equation can be similarly written as

$$2\mu_1 e_{ij,i} - p_{,j} = -f_i, \qquad v_{i,i} = 0, \qquad \mathbf{x} \in \Omega \tag{3.3.3}$$

Using Eshelby's equivalent inclusion method, one can assume the particle Ω has the same viscosity as the fluid, but introduce an eigenstrain rate $e_{ij}^*(x)$ in the particle Ω to represent

the disturbance caused by the mismatch of drop's viscosity. Based on Eshelby's equivalent inclusion method, e^*_{ij} satisfies

$$\mu_0 \left(e_{ij} - e^*_{ij}\right) = \mu_1 e_{ij}, \quad \mathbf{x} \in \Omega \tag{3.3.4}$$

Here, the eigenstrain rate is a fictitous non-mechanical field, which make the stress field in two problems equivalent (Mura, 1987). Then the original problem with an inhomogeneity can be treated as an inclusion problem with the eigenstrain rate satisfying Eq.(3.3.4). Therefore, Eq.(3.3.3) is rewritten as

$$2\mu_0 \frac{\partial}{\partial x_i}\left(e_{ij} - e^*_{ij}\right) - \frac{\partial p}{\partial x_j} = -f_j, \quad v_{i,i} = 0, \quad \mathbf{x} \in \Omega \tag{3.3.5}$$

To solve for the eigenstrain rate, it is written in terms of polynomial of $\mathbf{x}$ with the origin at the center of the ellipsoid, such as

$$e^*_{ij}(\mathbf{x}) = e^0_{ij} + e^1_{ijk} x_k + e^2_{ijkl} x_k x_l + ..., \quad \mathbf{x} \in \Omega \tag{3.3.6}$$

For one ellipsoidal inclusion moving in a fluid driven by a constant body force, the strain rate over the inclusion is linearly distributed (Yin et al., 2006; Yin and Sun, 2006). It can be seen that only one term $e^1_{ijk} x_k$ may make the exact solution for one drop problem (Lee and Yin, 2013). For simplicity, we directly write

$$e^*_{ij}(\mathbf{x}) = e^1_{ijk} x_k, \quad \mathbf{x} \in \Omega \tag{3.3.7}$$

where from the definition of e^*_{ij}, one can write

$$e^1_{ijk} = e^1_{jik} \quad \text{and} \quad e^1_{iik} = 0 \tag{3.3.8}$$

Notice that, for more than one particles, the eigenstrain rate should be more complex and

other terms in Eq.(3.3.6) will be non-zero. However, truncating it to linear terms has produced very accurate results, which will be demonstrated in next chapter (Lee and Yin, 2013).

Substituting Eqs.(3.3.1) and (3.3.6) into Eq.(3.2.12) yields

$$v_i(\mathbf{x}) = \frac{1}{4\pi\mu_0}\int_\Omega \left[\left(\delta_{ik}\phi - \frac{1}{2}\psi_{,ik}\right) f_k^0 \, d\mathbf{x}' - \int_\Omega \mu_0 \Gamma_{imn} e^1_{mnp} x_p^{'}\right] d\mathbf{x}' \tag{3.3.9}$$

Following Mura's book (1987), one can integrate Eq.(3.3.9) as

$$v_i(\mathbf{x}) = \frac{1}{4\pi\mu_0}\left[\left(\delta_{ik}\Phi - \frac{1}{2}\Psi_{,ik}\right) f_k^0 - \mu_0\left(\delta_{im}\Phi_{p,n} + \delta_{in}\Phi_{p,m} - \Psi_{p,imn}\right) e^1_{mnp}\right] \tag{3.3.10}$$

where Φ and Ψ denote the integral of ϕ and ψ over the ellipsoidal particle and Φ_p and Ψ_p denote the integral of $\phi x_p^{'}$ and $\psi x_p^{'}$. These integrals and their derivative terms are explicitly provided in Appendix C.

Similarly, Eq.(3.2.11) can be rewritten as

$$p(\mathbf{x}) = -\frac{1}{4\pi}\left[\Phi_{,k} f_k - 2\mu_0 \Phi_{p,mn} e^1_{mnp}\right] \tag{3.3.11}$$

According to Eq.(3.3.10), the derivative of velocity field can be obtained as

$$v_{i,j}(\mathbf{x}) = \frac{1}{4\pi\mu_0}\left[\left(\delta_{ik}\Phi_{,j} - \frac{1}{2}\Psi_{,ijk}\right) f_k^0 - \mu_0\left(\delta_{im}\Phi_{p,jn} + \delta_{in}\Phi_{p,jm} - \Psi_{p,ijmn}\right) e^1_{mnp}\right] \tag{3.3.12}$$

Then, strain rate field can be determined as

$$e_{ij}(\mathbf{x}) = \frac{1}{2}\left[v_{i,j}(\mathbf{x}) + v_{j,i}(\mathbf{x})\right] = \frac{1}{8\pi\mu_0}\left[F_{ijk} f_k^0 - D_{ijmnp} e^1_{mnp}\right] \tag{3.3.13}$$

where

$$F_{ijk} = \delta_{ik}\Phi_{,j} + \delta_{jk}\Phi_{,i} - \Psi_{,ijk} \tag{3.3.14}$$

$$D_{ijmnp} = \mu_0\left(\delta_{im}\Phi_{p,jn} + \delta_{in}\Phi_{p,jm} + \delta_{jm}\Phi_{p,in} + \delta_{jn}\Phi_{p,im} - 2\Psi_{p,ijmn}\right) \tag{3.3.15}$$

After e_{ij} is obtained, substitute Eq.(3.3.6) into Eq.(3.3.4), it can be rewritten as

$$e^*_{ij} = e^1_{ijr} x_r = \frac{\mu_0 - \mu_1}{\mu_0} e_{ij} \quad \mathbf{x} \in \Omega \tag{3.3.16}$$

Because Eq.(3.3.13) only include the linear terms, the above equation could be rewritten as

$$e^1_{ijr} = \frac{\mu_0 - \mu_1}{\mu_0} e_{ij,r} \tag{3.3.17}$$

The substitution of Eq.(3.3.13) into Eq.(3.3.17) yields

$$e^1_{ijr} = \frac{\mu_0 - \mu_1}{8\pi\mu_0^2} \left(F_{ijk,r} f^0_k - D_{ijmnp,r} e^1_{mnp} \right) \tag{3.3.18}$$

The above relation between e^1_{ijr} and f^0_kcan be rewritten as

$$e^1_{ijr} = S_{ijkr} f^0_k \tag{3.3.19}$$

where S_{ijkr} can be solved by the linear equation system with 27 linear algebra equations in (3.3.18) and will be explicitly provided in the next Section for the case of a spherical drop.

By substituting Eq.(3.3.19) into Eqs.(3.3.10) and (3.3.11), velocity field $v_i(\mathbf{x})$ and pressure field $p(\mathbf{x})$ can be written in terms of f^0_i. Then, the overall velocity of the drop can be determined as

$$\langle v_i \rangle = \frac{1}{V} \int_\Omega v_i \left(\mathbf{x} \right) \, d\mathbf{x} \tag{3.3.20}$$

where V is the volume of an ellipsoidal particle. The total drag force P_i can be written in terms of the body force as

$$P_i = -V f^0_i \tag{3.3.21}$$

which will be further discussed in Subsection 4.4. The relation between $\langle v_i \rangle$ and f^0_i can be obtained in Eq.(3.3.20) and the relation between P_i and f^0_i is given in Eq.(3.3.21); consequently, one can obtain the relation between the drag force and the effective velocity.

Because all the integrals can be obtained by the identities in Appendix C, which are given in terms of elliptic integrals, the solution for the pressure and velocity fields are given in Eqs.(3.3.11) and (3.3.10), respectively, with e^1_{ijr} written in Eq.(3.3.19). In the next section, we will use a spherical drop as an example to explain the capabilities and applications of the present method.

3.4 Results and Discussions

This section will demonstrate the present theory through a couple of examples for one drop moving a Newtonian fluid, including spheroidal and spherical drops. The formulation can be used to calculate the drag force for the motion of particle systems. The application and extension of this method to more general cases are also discussed.

3.4.1 Case Study for a Spheroidal Drop Moving in a Fluid

When two of three semi-diameters are equal, the ellipsoidal drop in Figure 3.2.1 becomes a spheroid drop. According to the derivation in Section 3, the term of $e^1_{ijk}(\mathbf{x})$ can be determined in terms of applied force f^0_i, when $\mathbf{x}$ is an interior point of Ω; and the velocity and pressure fields can be calculated in consequence. For example, the motion of a prolate spheroidal drop with radius $(a, a, 2a)$ and $(2a, a, a)$ are investigated in detail. Given the radii of a spheroidal drop and applied body force, the velocity of any interested point $\mathbf{x}$ at interior or exterior of spheroid can be determined. In Figures 3.4.1 and 3.4.2, the velocity component v_3 at points along three axes are plotted for two cases that the spheroid drop raising along the long and short axes, respectively. In each case, three different viscosities of drop, 0.01, twice larger than viscosity of fluid and infinite are considered to approximate the inhomogeneities of an air bubble, a drop and a solid, respectively. When the same body force f^0_i is applied, it is observed that the average raising velocity of spheroidal drop will be affected by the viscosity: the drop with a lower viscosity will have a higher velocity. Besides, the moving orientation of

the spheroidal drop has different velocities for the Stokes' flow. For a spheroidal air bubble ($\mu_1 = 0.01$) moving along the long axis, the velocity of bubble center approaches 0.4 in Figure 3.4.1; whereas the velocity will reduce to about 0.15 if it moves along the short axis in Figure 3.4.2.

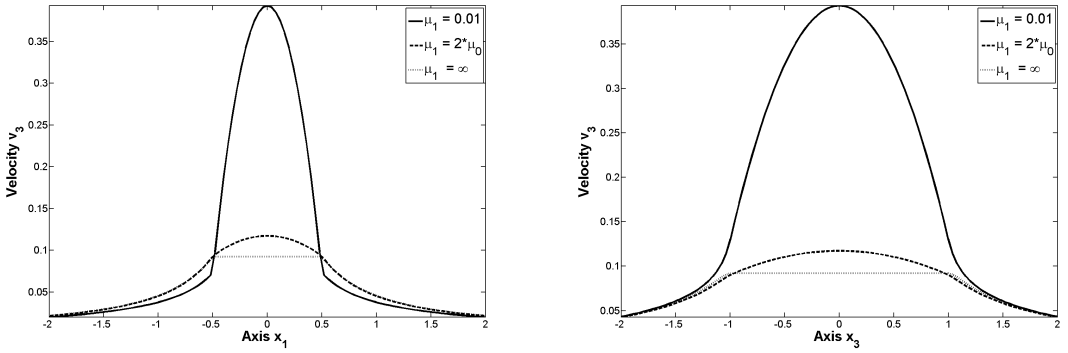

(a) (b)

Figure 3.4.1: The comparison of x_3-component of velocity at points along (a) x_1 and (b) x_3 axes when the the drop moves along the long axis of x_3 direction with assumption of $a_1 = a_2 = 0.5$, $a_3 = 1$ and body force $f_i^0 = 1$

The velocity vector and the contour of velocity field along $x_1 - x_3$ and $x_2 - x_3$ planes for two cases of spheroidal drop ($\mu_1 = 2\mu_0$) are plotted in Figures 3.4.3 and 3.4.4. According to the results shown in Figure 3.4.4, the vortex ring will be created in the spheroidal drop when it moves along the short axis. However, the drop will deform soon due to the concentration of maximum velocity at both edge, as shown in Figure 3.4.3, when the spheroidal drop raising edgeways.

3.4.2 Explicit Solution for Spherical Drop

When $a_1 = a_2 = a_3 = a$, the ellipsoidal drop in Figure 3.2.1 becomes a spherical drop. When $\mathbf{x}$ is an interior point of Ω, from Eqs.(3.3.14) ~ (3.3.15), F_{ijk} and D_{ijmnp} for the spherical drop can be explicitly derived, with the aid of the identities in Appendix C, as

$$F_{ijk} = -\frac{4\pi}{5}\delta_{ik}x_j - \frac{4\pi}{5}\delta_{jk}x_i + \frac{8\pi}{15}\delta_{ij}x_k \tag{3.4.1}$$

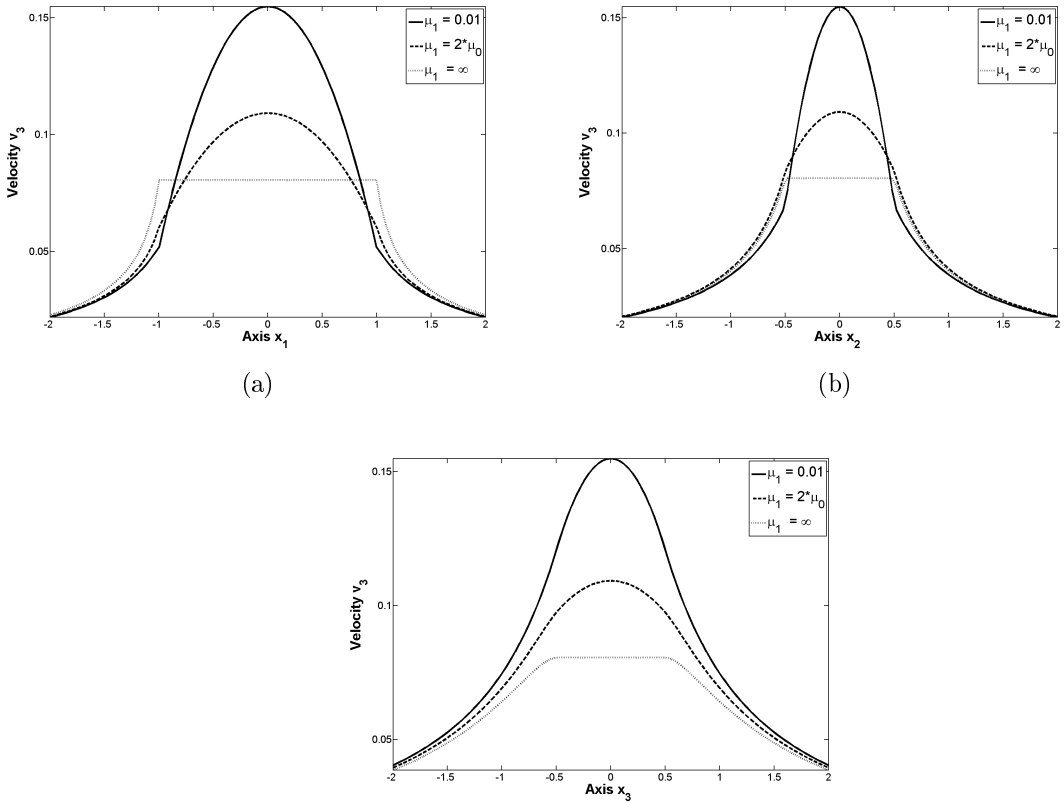

(a) (b)

(c)

Figure 3.4.2: The comparison of x_3-component of velocity at points along (a) x_1, (b) x_2 and (c) x_3 axis when the the drop moves along the short axis of x_3 direction with assumption of $a_1 = 1$, $a_2 = a_3 = 0.5$ and body force $f_i^0 = 1$

$$D_{ijmnp} = \mu_0 \begin{bmatrix} \left(\frac{16\pi}{35}\delta_{jp}\delta_{mn} - \frac{12\pi}{35}\delta_{jm}\delta_{np} - \frac{12\pi}{35}\delta_{jn}\delta_{mp}\right) x_i \\ + \left(\frac{16\pi}{35}\delta_{ip}\delta_{mn} - \frac{12\pi}{35}\delta_{im}\delta_{np} - \frac{12\pi}{35}\delta_{in}\delta_{mp}\right) x_j \\ + \left(\frac{16\pi}{35}\delta_{ij}\delta_{np} - \frac{12\pi}{35}\delta_{ip}\delta_{jn} - \frac{12\pi}{35}\delta_{in}\delta_{jp}\right) x_m \\ + \left(\frac{16\pi}{35}\delta_{ij}\delta_{mp} - \frac{12\pi}{35}\delta_{ip}\delta_{jm} - \frac{12\pi}{35}\delta_{im}\delta_{jp}\right) x_n \\ + \left(\frac{16\pi}{35}\delta_{ij}\delta_{mn} - \frac{8\pi}{7}\delta_{im}\delta_{jn} - \frac{8\pi}{7}\delta_{in}\delta_{jm}\right) x_p \end{bmatrix} \tag{3.4.2}$$

Substitute Eqs.(3.4.1) and (3.4.2) into Eq.(3.3.13); then, S_{ijkr} in Eq.(3.3.19) can be derived from Eqs.(3.3.16) ~ (3.3.18) and can be explicitly written as

$$S_{ijkr} = \gamma\delta_{ij}\delta_{kr} + \xi\left(\delta_{ik}\delta_{jr} + \delta_{jk}\delta_{ir}\right) \tag{3.4.3}$$

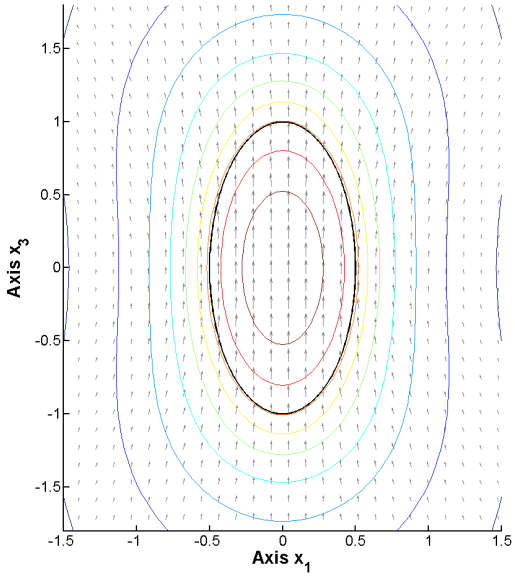

Figure 3.4.3: The vector and contour of velocity on $x_1 - x_3$ ($x_2 - x_3$) plane when the drop moves in the long axis of x_3 direction with assumption of $a_1 = a_2 = 0.5$, $a_3 = 1$ and body force $f_i^0 = 1$

where

$$\begin{cases} \gamma = \frac{\mu_0 - \mu_1}{3\mu_0(2\mu_0 + 3\mu_1)} \\ \xi = \frac{\mu_0 - \mu_1}{-2\mu_0(2\mu_0 + 3\mu_1)} \end{cases} \tag{3.4.4}$$

Therefore, the velocity field $v_i(\mathbf{x})$ from Eq.(3.3.10) can be rewritten as:

$$v_i(\mathbf{x}) = \begin{cases} \frac{1}{3\mu_0(2\mu_0+3\mu_1)} \begin{bmatrix} \left(3a^2\mu_0 + 2a^2\mu_1 - 2x^2\mu_0\right) f_i^0 \\ +\mu_0 x_i x_k f_k^0 \end{bmatrix}, & \mathbf{x} \in \Omega \\ \frac{1}{6\mu_0(2\mu_0+3\mu_1)} \begin{bmatrix} a^2\rho\left(2\mu_0 + 3\mu_1 + \rho^2\mu_1\right) f_i^0 \\ +\rho^3\left(2\mu_0 + 3\mu_1 - 3\rho^2\mu_1\right) x_i x_k f_k^0 \end{bmatrix}, & \mathbf{x} \in D - \Omega \end{cases} \tag{3.4.5}$$

where

$$\begin{cases} x^2 = x_i x_i \\ \rho = \frac{a}{x} \end{cases} \tag{3.4.6}$$

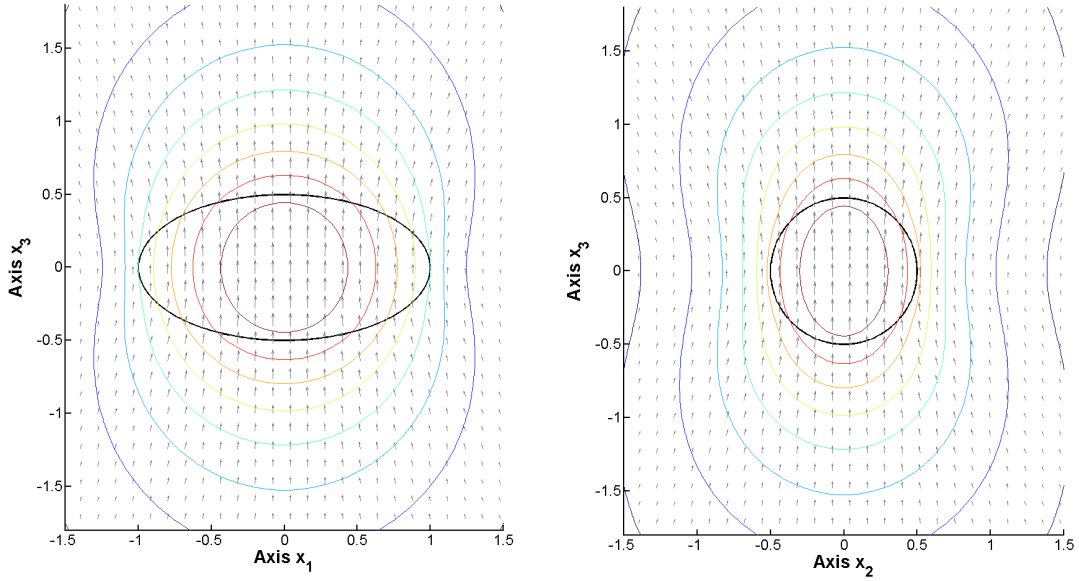

(a) (b)

Figure 3.4.4: The vector and contour of velocity on (a) $x_1 - x_3$ and (b) $x_2 - x_3$ plane when a spheroidal drop moves in the short axis of x_3 direction with assumption of $a_1 = 1$, $a_2 = a_3 = 0.5$ and body force $f_i^0 = 1$

Similarly, the pressure field $p(\mathbf{x})$ from Eq.(3.3.11) can be rewritten as

$$p(\mathbf{x}) = \begin{cases} \frac{6\mu_0 - \mu_1}{3(2\mu_0 + 3\mu_1)} x_k f_k^0, & \mathbf{x} \in \Omega \\ \frac{1}{3} a \rho^2 n_k f_k^0, & \mathbf{x} \in D - \Omega \end{cases} \tag{3.4.7}$$

Here the constant pressure term in the far field has not been included. Otherwise, a uniform pressure term should be superposed in the above equation.

With the known integrals as

$$\begin{cases} \int_\Omega a^2 \, dx = \frac{4\pi a^5}{3} \\ \int_\Omega x^2 \, dx = \frac{4\pi a^5}{5} \\ \int_\Omega x_i x_j \, dx = \frac{4\pi a^5}{15} \delta_{ij} \end{cases} \tag{3.4.8}$$

The average velocity field $\langle v_i \rangle$ over the drop can be determined as

$$\begin{aligned} \langle v_i \rangle &= \frac{3}{4\pi a^3} \int_\Omega v_i(x)\ dx \\ &= \frac{2(\mu_0+\mu_1)a^2}{3\mu_0(2\mu_0+3\mu_1)} f_i^0 \end{aligned} \tag{3.4.9}$$

For three different case, such as spherical solid particle, drop and air void, it is obtained that

$$\begin{cases} \langle v_i \rangle_s = \frac{2a^2}{9\mu_0} f_i^0, & \text{for solid sphere } \mu_1 = \infty \\ \langle v_i \rangle_a = \frac{a^2}{3\mu_0} f_i^0, & \text{for spherical air void } \mu_1 = 0 \\ \langle v_i \rangle_d = \frac{2(\mu_0+\mu_1)a^2}{3\mu_0(2\mu_0+3\mu_1)} f_i^0, & \text{for spherical drop with viscosity } \mu_1 \end{cases} \tag{3.4.10}$$

From Eq.(3.3.21), the total drag force can be determined by substituting Eq.(3.4.10)

$$P_i = -\tfrac{4\pi a^3}{3} f_i^0$$

$$\Rightarrow \begin{cases} P_i^s = -6\pi a \mu_0 \langle v_i \rangle, & \text{for solid sphere } \mu_1 = \infty \\ P_i^a = -4\pi a \mu_0 \langle v_i \rangle, & \text{for spherical air void } \mu_1 = 0 \\ P_i = -2\pi a \mu_0 \langle v_i \rangle \frac{2\mu_0+3\mu_1}{(\mu_0+\mu_1)} f_i^0, & \text{for spherical drop with viscosity } \mu_1 \end{cases} \tag{3.4.11}$$

The above results of drag force for three different cases show the exactly the same with the one derived by Stokes' law (Batchelor, 1967). Comparing the velocity and pressure fields in Eqs.(3.4.5) and (3.4.7) with the classic solutions (Batchelor, 1967), we found they are also consistent.

3.4.3 Continuity of the Interface

Although both the EIM and classic solution provide the same results, they follow very different methodology. The classic solution is formulated from a specific boundary value problem using the continuity of the normal velocity cross the interface ; whereas the EIM is based on the equivalence of the materials by introducing an eigenstrain rate over the drop.

Obviously, for one spherical drop moving in a fluid, the velocity continuity has been exactly satisfied in Eq.(3.4.5). Notice that the pressure field is discontinuous, written as

$$p^{+} - p^{-} = \frac{4\left(\mu_0 - \mu_1\right)}{3\left(2\mu_0 + 3\mu_1\right)} x_j f_j^0 \tag{3.4.12}$$

but the stress vector along the interface is still continuous

$$n_j \left(\sigma_{ji}^{+}\right)_{r=a} = n_j \left(\sigma_{ji}^{-}\right)_{r=a} = \frac{1}{a\left(2\beta + 3\right)} \left[-2\beta x_i x_j f_j^0 - x^2 f_i^0\right] \tag{3.4.13}$$

Notice that in the above analysis, no surface tension is considered. Otherwise, a constant term can be superposed to the pressure field in either outer or inner of the sphere, which still satisfies the governing equation. It means that Eq.(3.4.12) may include one more constant term. It causes the component of the above stress vector in the surface normal direction may be discontinuous with the constant pressure term, which should be balanced by the surface tension of the interface (Batchelor, 1967).

For a general ellipsoidal drop, the velocity continuity across the interface is also guaranteed by Eq.(3.2.10) for the continuity of the elliptic integrals in the Appendix C. However, because the integral of Eqs.(C.0.4) and (C.0.18) is discontinuous for the components of $i = j$, which are caused by the integral of a Dirac delta function, the pressure field in Eq.(3.2.11) is generally discontinuous. However, the equivalent condition guarantees the continuity of the stress vector across the interface. Therefore, for one ellipsoidal drop moving in a Newtonian fluid, the interfacial continuities of velocity and stress vector can be exactly satisfied.

The EIM deals with a homogenous fluid system with an eigenstrain rate on the inhomogeneities, which can be easily extended to other cases, such as multiple drops with different sizes. The present method can be implemented through numerical methods to solve general Stokes flow problems of heterogeneous fluid systems. In next chapter, the application of the EIM for the case of two or more particles will be demonstrated (Lee and Yin, 2013; Lee et al., 2013).

In general cases of drops moving in a fluid, because the governing equations over the whole domain have automatically been satisfied through the Green's function technique, if the interfacial continuities of velocity and stress vector could be satisfied, one should obtain the exact solution. Obviously, the velocity continuity can always be satisfied. However, the continuity of stress vector along the interface will depend on the accuracy of the polynomial form of the eigenstrain field over the drop. For ellipsoidal drops, the eigenstrain field is smooth, a few polynomial terms may provide high accuracy. For example, Lee and Yin (Lee and Yin, 2013) will demonstrate that a linear approximate form of eigenstrain field can provide sufficient accuracy for a two-particle case.

3.4.4 Drag Force and Drop Velocity

Given a body force on a drop, the material difference is simulated by an eigenstrain rate. Once the equivalent inclusion problem is solved, the strain rate and stress fields can be obtained. Here the Stokes flow is considered and so no acceleration of an infinitesimal element of the fluid is included in the equilibrium equation. The drag force can be obtained by the integral of the surface stress vector over the interface, i.e.

$$P_j = \int_{\partial\Omega} n_i \sigma_{ij} d\mathbf{x} \tag{3.4.14}$$

Using the Gauss' theorem and the equilibrium equation, the above equation can be rewritten

$$P_j = \int_{\Omega} \sigma_{ij,i} d\mathbf{x} = \int_{\Omega} -f_i^0 d\mathbf{x} = -V f_i^0 \tag{3.4.15}$$

where V is the total volume of the drop. Therefore, the drag force on the moving drop is balanced by the driving force, which is considered as a uniformly distributed body force in this chapter. This provides Eq.(3.3.21).

Given a driving force, the velocity on the moving drop is not uniform. For simplicity, we

used the average velocity to represent the drop's velocity, which can be written as

$$\langle v_j \rangle = \int_\Omega v_j \left(\mathbf{x}\right) d\mathbf{x} = \int_\Omega \left(x_j v_i\right)_{,i} d\mathbf{x} \tag{3.4.16}$$

where $v_{i,i} = 0$ has been used. Using the Guass' theorem, the above equation can be written as

$$\langle v_j \rangle = \int_{\partial\Omega} v_i n_i x_j d\mathbf{x} \tag{3.4.17}$$

Because the velocity is continuous on the interface, the above surface integral is well defined. In general cases, the above integral forms of drag force and velocity are still applicable. For a solid particle, the velocity is uniform over the drop. The above equation is obvious. Because the average velocity is also written in term of f_i^0, the relation between the drag force and drop velocity can be obtained.

Chapter 4

Extension of the Equivalent Inclusion Method to Multiple Drops

The Eshelby's equivalent inclusion method (EIM) has been presented to investigate the motion of drops moving in a Newtonian fluid at small Reynolds number caused by the body force, such as buoyancy or gravity in last chapter. The material mismatch between the drop and matrix fluids is simulated by a fictitious nonmechanical strain rate, namely eigenstrain rate on the drop, which is written in a polynomial form of the local coordinates. Using the equivalent inclusion condition, the eigenstrain rate on each drop is solved and the velocity field is derived with the Green's function technique. The interaction between a pair of drops is investigated. The velocities of the drops depend on the relative position, the center-to-center distance of drops, the viscosity and size of drops. For the case of a pair of identical spherical drops, the present method using a linear approximation of the eigenstrain rate has provided a very close solution to the explicit solution provided by Batchelor in 1972 for the average velocity of drops moving in the fluid. If a higher order of the polynomial form of eigenstrain rate is used, one can expect a more accurate result. Although only two spherical drops are considered in this chapter, this method is general and can be extended

to a many-body system with ellipsoidal shape of drops.

4.1 Overview

A pair of drops moving in a viscous fluid have been studied in the past century. Stimson and Jeffery investigated the motion of two equal or unequal spheres moving parallel to their line of centers (Stimson and Jeffery, 1926). Goldman, Cox and Brenner determined the terminal velocity of two identical arbitrary oriented spheres settling in an unbounded fluid at small Reynolds numbers, either the interactive force and torque due to the translation (Goldman et al., 1966). After Batchelor's organizing, the translation velocity of two identical rigid spheres with centers separated by the vector $\mathbf{r}$ as

$$\mathbf{U} = \lambda_1 \mathbf{r} \frac{\mathbf{r}.\mathbf{U_0}}{r^2} + \lambda_2 \left(\mathbf{U_0} - \mathbf{r} \frac{\mathbf{r}.\mathbf{U_0}}{r^2} \right) \tag{4.1.1}$$

where $\mathbf{U_0}$ is the terminal velocity of either rigid sphere falling in isolation, and λ_1 and λ_2 are constants corresponding to the ratio of r to radius of sphere a (Batchelor, 1972).

To solve the problems of two spherical inhomogeneities in the infinite domain, three standard methods have already been studied. The first method is the use of bispherical (spherical bipolar) coordinates developed by Jeffery to solve electromagnetic fields related to Laplace´s equation in 1912 (Jeffery, 1912) . Afterward, it is applied to calculate the elastic fields for two voids or rigid spheres by Sternberg and Sadowsky (1952) and Shelley and Yu (1966). The multipole expansion method is served as the second method. For elastic problem, it is employed to solve elastic fields for two voids by Miyamoto (1955; 1958), and Tsuchida et. al. (1976); Chen and Acrivos (1978) even extended it to general elastic spheres. Moreover, Ross (1968), Jeffery (1973), and Klingenberg and Zukoski (1990) formalized this method for the electromagnetic problem. The problem of two identical rigid spheres with interaction forces and moments embedded in the infinite domain is solved by Borcea and Bruno (2001). The last is based on the modified Green's function combined with Eshelby's

equivalent inclusion method (EIM). Moschovidis and Mura (1975) utilize it to obtain elastic fields for two ellipsoidal inhomogeneities. The first method requires the numerical solution of a set of infinite linear equations for each separation distance between the spheres; the second requires the derivation of recurrence formulae for relating the coefficients of the spherical harmonics (Chen and Acrivos, 1978), and; the last method involves Taylor´s expansions of the eigenstrain and local strain. Even though all of these methods could provide any desired degree of accuracy by retaining the appropriate number of terms, the last method provides convenience for studying the interaction between particles with an analytical expression (Ju and Chen, 1994a,b). Moreover, it can be used for general ellipsoidal particles (Moschovidis and Mura, 1975).

To exactly solve the local field for an inhomogeneity in an infinite matrix under a uniform far field stress, Eshelby (1957; 1959) firstly proposed that the stress disturbance caused by the inhomogeneity could be simulated by an inclusion with the same material properties as the matrix but with a appropriately chosen eigenstrain. Eshelby's EIM is not only valuable for the effective elastic moduli of composite (Y. Takao et al., 1982; Chen and Cheng, 1996; Yin et al., 2008a), it also successfully applied for the prediction of thermal and electric behavior of composite (Huang, 1996; Hatta and Taya, 1986; Sakata et al., 2010; Takei et al., 1991a,b; Dunn and Taya, 1993). In the elastic problem of infinite domain containing inhomogeneity, the overall elastic fields, stress, strain and displacement field, is the summation of far field and disturbed elastic field. Elastic Green's function provides the connection between disturbed strain field and eigenstrain of the equivalent inclusion; the EIM is used to correlate the eigenstrain of the equivalent inclusion and far field strain field together (Mura, 1987).

Although two drops moving in a viscous fluid are completely different from two particles deforming in a matrix in physics point of view, when the drops move slowly, the two problems share the same mathematical formulation, so that they may be solved in the same approach too. In this chapter, Eshelby's EIM has been extended to the Stokes flow of two drops moving in a viscous fluid. The size, location and viscosity of each drop can be arbitrary.

This approach is new in fluid mechanics and can be applied to the multiphase flow problem with many particles. In this particular study, only two drops are considered. The eigenstrain rate on each particle is assumed in a polynomial form in the position coordinates by following Moschovidis and Mura's algorithm (1975), and it can be solved from a linear equation system numerically. Besides, the interaction between two spherical drops is investigated, the effects on the translational velocity of each drop by several parameters, such as orientation, viscosity and size of drops, are studied.

The remainder of this chapter is organized as follows: Section 4.2 briefly reviews the Eshelby's equivalent inclusion method, and introduces the algorithm to derive the eigenstrain rate on the drops and the overall velocity and pressure fields . Section 4.3 demonstrates the numerical results for case studies, in which a pair of distinct drops are considered. When two identical spherical drops are considered, the results of present method well agree with Batchelor's solution (Batchelor, 1972). This method is general and can be extended to a many-particle system by the numerical methods (Lee et al., 2013).

4.2 Basic Formulation

4.2.1 Introduction to the Equivalent Inclusion Method

Using Mura's definition (1987) in a fluid system, an inclusion in an infinite homogeneous fluid D is defined as a subdomain Ω, where an eigenstrain rate $e^*_{ij}(\mathbf{x})$ or a body force $f_i(\mathbf{x})$ is applied on Ω but is zero on $D-\Omega$. The viscosities of the fluids in the inclusion and the rest (matrix) are the same. On the other hand, an inhomogeneity is a subdomain in a homogenous fluid with different material properties from the rest. In the following of this section, we focus on the inclusion problem. Consider one drop Ω with viscosity μ_1 embedded in a fluid with viscosity μ_0 subjected to a body force on the drop. Using Eshelby's equivalent inclusion method, one can assume the drop Ω has the same viscosity as the fluid, but introduce an eigenstrain rate $e^*_{ij}(x)$ in the particle Ω to represent the disturbance caused by the mismatch

of drop's viscosity. Based on Eshelby's equivalent inclusion method, e^*_{ij} satisfies

$$\mu_0 \left(e_{ij} - e^*_{ij}\right) = \mu_1 e_{ij}, \quad \mathbf{x} \in \Omega \tag{4.2.1}$$

where the strain rate field $e_{ij}(\mathbf{x})$ is given by

$$e_{ij}(\mathbf{x}) = \frac{1}{2}\left[v_{i,j}(\mathbf{x}) + v_{j,i}(\mathbf{x})\right] \tag{4.2.2}$$

and the eigenstrain rate is a fictitous non-mechanical field, which make the stress field in two problems equivalent (Mura, 1987). Then, the original problem with an inhomogeneity can be treated as an inclusion problem with the eigenstrain rate satisfying Eq.(4.2.1). Therefore, the equation of motion is written as

$$2\mu_0 \frac{\partial}{\partial x_i}\left(e_{ij} - e^*_{ij}\right) - \frac{\partial p}{\partial x_j} = -f_j, \quad v_{i,i} = 0, \quad \mathbf{x} \in \Omega \tag{4.2.3}$$

Following our work in last chapter (Yin and Lee, 2013), the velocity and pressure fields caused by the body force and eigenstrain rate on the inclusions of an infinite fluid domain can be obtained by the Green's function. The velocity field $v_i(\mathbf{x})$ is given by

$$v_i(\mathbf{x}) = \int_\Omega G_{ik}\left(\mathbf{x}, \mathbf{x}'\right) f_k - \mu_0 \Gamma_{imn}\left(\mathbf{x}, \mathbf{x}'\right) e^*_{mn} \, d\mathbf{x}' \tag{4.2.4}$$

and the pressure field $p_i(\mathbf{x})$ is shown as

$$p(\mathbf{x}) = -\frac{1}{4\pi}\int_\Omega \left(\phi_{,k} f_k - 2\mu_0 \phi_{,mn} e^*_{mn}\right) \, d\mathbf{x}' \tag{4.2.5}$$

where $f_i(\mathbf{x})$ is the body force uniformly distributed on the drop; an eigenstrain rate $e^*_{ij}(x)$ can be a continuously tensorial field on the drop; and the tensorial and modified Green's

function are written as

$$\begin{cases} G_{ij} &= \frac{1}{4\pi\mu_0}\left(\delta_{ij}\phi - \frac{1}{2}\frac{\partial^2\psi}{\partial x_i \partial x_j}\right) \\ \Gamma_{imn} &= G_{im,n} + G_{in,m} \end{cases} \tag{4.2.6}$$

with

$$\phi\left(\mathbf{x},\mathbf{x}'\right) = \frac{1}{|\mathbf{x}-\mathbf{x}'|}, \qquad \psi\left(\mathbf{x},\mathbf{x}'\right) = |\mathbf{x}-\mathbf{x}'| \tag{4.2.7}$$

If the velocity field obtained by Eq.(4.2.4) makes the equivalent inclusion condition of Eq.(4.2.1) exactly satisfied, one can obtain the exact solution of the original boundary value problem. When a single drop moves in the fluid, the eigenstrain rate $e^*_{ij}(\mathbf{x})$ can be assumed as a linear function , which can be correlated with the body force $f_i(\mathbf{x})$. Using the eigenstrain rate and body force in Eqs.(4.2.4) and (4.2.5), the velocity and pressure fields can be expressed explicitly. However, for the cases of two or more drops moving in the fluid, the eigenstrain rate distribution could be more complex. Instead, the eigenstrain rate distribution can be written in the polynomial form, and the coefficients of each order of the coordinate can be determined separately by numerical method (Moschovidis and Mura, 1975). In what follows, we will first go through the single drop solution (Yin and Lee, 2013). Following the similar steps, we will elaborate the procedure to solve the two drop solution.

4.2.2 Numerical Approach to Single Spherical Drop

For the single spherical drop Ω moving in an infinite homogenous fluid domain D driven by a constant body force, set one coordinate system with origin at center of the drop. The body force $f_i(\mathbf{x})$ is written as

$$f_i(\mathbf{x}) = \begin{cases} f_i^0, & \mathbf{x} \in \Omega \\ 0, & \mathbf{x} \in D - \Omega \end{cases} \tag{4.2.8}$$

however, the eigenstrain rate is expressed in polynomial form as

$$e_{ij}^{*}(\mathbf{x}) = \begin{cases} E_{ij} + E_{ijk}x_r + E_{ijkl}x_r x_s + ..., & \mathbf{x} \in \Omega \\ 0, & \mathbf{x} \in D - \Omega \end{cases} \tag{4.2.9}$$

For the single drop case, as proven later, the eigenstrain rate can be written in term of a linear function as

$$e_{ij}^{*}(\mathbf{x}) = E_{ijk}x_k \ , \ \mathbf{x} \in \Omega \tag{4.2.10}$$

The velocity of any points in the fluid can be rewritten by substitution of Eq.(4.2.6) into Eq.(4.2.4),

$$v_i(\mathbf{x}) = \frac{1}{4\pi\mu_0}\left[\left(\delta_{ik}\Phi - \frac{1}{2}\Psi_{,ik}\right) f_k - \mu_0\left(\delta_{im}\Phi_{p,n} + \delta_{in}\Phi_{p,m} - \Psi_{p,imn}\right) E_{mnp}\right] \tag{4.2.11}$$

where Φ, Ψ, $\Phi_p$and Ψ_p denote the integral of ϕ and ψ over the ellipsoidal particle by following Mura's book (1987) as

$$\begin{cases} \Phi = \int_\Omega \phi \, dx' \\ \Psi = \int_\Omega \psi \, dx' \end{cases} \quad \text{and} \quad \begin{cases} \Phi_p = \int_\Omega \phi x_p^{'} \, dx' \\ \Psi_p = \int_\Omega \psi x_p^{'} \, dx' \end{cases} \tag{4.2.12}$$

In general, if the eigenstrain rate is given in the polynomial form of Eq.(4.2.9), the strain rate caused by the constant body force and the eigenstrain rate can be similarly written as below:

$$e_{ij}(\mathbf{x}) = F_{ijk}(\mathbf{x})f_k^0 + D_{ijmn}(\mathbf{x})E_{mn} + D_{ijmnp}(\mathbf{x})E_{mnp} + ... \tag{4.2.13}$$

where

$$\begin{aligned} F_{ijk} &= \tfrac{1}{8\pi\mu_0}\left(\delta_{ik}\Phi_{,j} + \delta_{jk}\Phi_{,i} - \Psi_{,ijk}\right) \\ D_{ijmn} &= -\tfrac{1}{8\pi}\left(\delta_{im}\Phi_{,jn} + \delta_{in}\Phi_{,jm} + \delta_{jm}\Phi_{,in} + \delta_{jn}\Phi_{,im} - 2\Psi_{,ijmn}\right) \\ D_{ijmnp} &= -\tfrac{1}{8\pi}\left(\delta_{im}\Phi_{p,jn} + \delta_{in}\Phi_{p,jm} + \delta_{jm}\Phi_{p,in} + \delta_{jn}\Phi_{p,im} - 2\Psi_{p,ijmn}\right), \quad \text{etc.} \end{aligned} \tag{4.2.14}$$

For spherical drops, the above tensors have been explicitly integrated and been provided in the Appendix C.

To solve for eigenstrain rate, the strain rate $e_{ij}(\mathbf{x})$ can be expanded in the Taylor series as

$$e_{ij}(\mathbf{x}) = e_{ij}(\mathbf{0}) + \frac{\partial}{\partial x_r} e_{ij}(\mathbf{0}) x_r + \frac{\partial^2}{\partial x_r \partial x_s} e_{ij}(\mathbf{0}) x_r x_s + ... \tag{4.2.15}$$

Substituting Eqs.(4.2.9) and (4.2.15) into equivalency equation, shown as Eq.(4.2.1), and comparing of coefficient of constants and x_r etc., one can obtain

$$\begin{array}{rcl} E_{ij} & = & \frac{\mu_0 - \mu_1}{\mu_0} \left\{ F_{ijk}(\mathbf{0}) f_k^0 + D_{ijmn}(\mathbf{0}) E_{mn} + D_{ijmnp}(\mathbf{0}) E_{mnp} + ... \right\} \\ E_{ijr} & = & \frac{\mu_0 - \mu_1}{\mu_0} \left\{ F_{ijk,r}(\mathbf{0}) f_k^0 + D_{ijmn,r}(\mathbf{0}) E_{mn} + D_{ijmnp,r}(\mathbf{0}) E_{mnp} + ... \right\}, \quad \text{etc.} \end{array} \tag{4.2.16}$$

where the notation $F_{ijk}[0]$, $F_{ijk,r}[0]$, $D_{ijmn}[0]$, $D_{ijmn,r}[0]$, etc., means that these function and their derivatives are evaluated at the point 0, the center of spherical drop. After reorganization, the foregoing equation yields

$$\begin{array}{rcl} \left\{ D_{ijmn}(\mathbf{0}) - \beta \cdot I_{ijmn} \right\} E_{mn} + D_{ijmnp}(\mathbf{0}) E_{mnp} + ... & = & -F_{ijk}(\mathbf{0}) f_k^0 \\ D_{ijmn,r}(\mathbf{0}) E_{mn} + \left\{ D_{ijmnp,r}(\mathbf{0}) - \beta \cdot I_{ijmnpr} \right\} E_{mnp} + ... & = & -F_{ijk,r}(\mathbf{0}) f_k^0 \end{array} \tag{4.2.17}$$

where $\beta = \frac{\mu_0}{\mu_0 - \mu_1}$ and I is the unit tensor which maps a tensor to itself through the corresponding multiplications. Then the unknowns E_{ij}, E_{ijr}, etc. can be determined from the linear equation system by numerical method. Notice that for the case of a single drop, $D_{ijmnp}(\mathbf{0}) = F_{ijk}(\mathbf{0}) = D_{ijmn,r}(\mathbf{0}) = \mathbf{0}$, one can observed $E_{mn} = 0$ so that the eigenstrain rate in Eq.(4.2.10) provides the exact solution (Yin and Lee, 2013). Using the eigenstrain rate in Eqs.(4.2.4) and (4.2.5), the velocity and pressure fields at any point in this domain can be obtained.

4.2.3 Pair of Spherical Drops Moving in a Viscous Fluid

For the pair of arbitrarily oriented spherical drops, Ω_I and Ω_{II}, moving in a homogenous fluid domain driven by the constant body force, set two coordinate systems, says 1^{st} and 2^{nd} system, with origin at point $0\,(x_{1,}x_{2,}x_{3,})$ and $\overline{0}\,(\overline{x}_{1,}\overline{x}_{2,}\overline{x}_{3,})$ respectively, as shown in Figure 4.2.1. Moreover, the corresponding coordinates x_i and $\overline{x}_i$ are the 1^{st} coordinate and the 2^{nd} coordinate. For an arbitrary point P in the domain, x_i^P and $\overline{x}_i^P$ stand for the corresponding coordinates in the two systems and their relation is expressed as

$$x_i^P = x_i^{\overline{0}} + \overline{x}_i^P \tag{4.2.18}$$

The velocity field of any point located in the fluid domain will be the superposition of the field induced by the sources of body forces and eigenstrain rates of the two moving drops as follows:

$$v_i(\mathbf{x^P}) = \frac{1}{4\pi\mu_0}\int_{\Omega_I+\Omega_{II}} G_{ik}\left(\mathbf{x},\mathbf{x}'\right) f_k - \mu_0\Gamma_{imn}\left(\mathbf{x},\mathbf{x}'\right) e^*_{mn}\, d\mathbf{x}' \tag{4.2.19}$$

where f_k^I and f_k^{II} are the body force applied on Ω_I and Ω_{II} respectively, and the eigenstrain rates applied on each drop is written as

$$\begin{aligned} e^*_{ij}(\mathbf{x}) &= E^I_{ij} + E^I_{ijk}x_r + E^I_{ijkl}x_r x_s + ... \\ \overline{e}^*_{ij}(\overline{\mathbf{x}}) &= E^{II}_{ij} + E^{II}_{ijk}\overline{x}_r + E^{II}_{ijkl}\overline{x}_r\overline{x}_s + ... \end{aligned} \tag{4.2.20}$$

Similarly, the field of strain rate in two coordinate systems is the summation as

$$\begin{aligned} e_{ij}(\mathbf{x^P}) &= e^I_{ij}(\mathbf{x^P}) + e^{II}_{ij}(\mathbf{x^P}) \\ \overline{e}_{ij}(\overline{\mathbf{x}}^{\mathbf{P}}) &= \overline{e}^I_{ij}(\overline{\mathbf{x}}^{\mathbf{P}}) + \overline{e}^{II}_{ij}(\overline{\mathbf{x}}^{\mathbf{P}}) \end{aligned} \tag{4.2.21}$$

where $e^I_{ij}(\mathbf{x^P})$ is the strain rate at point P induced by an body force f_k^I and eigenstrain rate e^*_{ij} in Ω_I in 1^{st} coordinate system; $\overline{e}^{II}_{ij}(\overline{\mathbf{x}}^{\mathbf{P}})$ is the strain rate at point P induced by an body force f_k^{II} and eigenstrain rate $\overline{e}^*_{ij}$ in Ω_{II} in 2^{nd} coordinate system and so on. According

to Eq.(4.2.13), these induced strain rates are defined as

$$\begin{aligned} e_{ij}^{I}(\mathbf{x^P}) &= F_{ijk}^{I}(\mathbf{x^P})f_k^I + D_{ijmn}^{I}(\mathbf{x^P})E_{mn}^{I} + D_{ijmnp}^{I}(\mathbf{x^P})E_{mnp}^{I} + ... \\ \overline{e}_{ij}^{II}(\overline{\mathbf{x}}^{\mathbf{P}}) &= F_{ijk}^{II}(\overline{\mathbf{x}}^{\mathbf{P}})f_k^{II} + D_{ijmn}^{II}(\overline{\mathbf{x}}^{\mathbf{P}})E_{mn}^{II} + D_{ijmnp}^{II}(\overline{\mathbf{x}}^{\mathbf{P}})E_{mnp}^{II} + ... \end{aligned} \tag{4.2.22}$$

As mentioned in Eq.(4.2.15), the above strain rates can be expanded in the Taylor series as

$$\begin{aligned} e_{ij}^{I}(\mathbf{x^P}) &= e_{ij}^{I}(0) + \tfrac{\partial}{\partial x_r}e_{ij}^{I}(0)x_r^P + \tfrac{\partial^2}{\partial x_r \partial x_s}e_{ij}^{I}(0)x_r^P x_s^P + ... \\ e_{ij}^{II}(\mathbf{x^P}) &= \overline{e}_{ij}^{II}(0) + \tfrac{\partial}{\partial \overline{x}_r}\overline{e}_{ij}^{II}(0)x_r^P + \tfrac{\partial^2}{\partial \overline{x}_r \partial \overline{x}_s}\overline{e}_{ij}^{II}(0)x_r^P x_s^P + ... \\ \overline{e}_{ij}^{I}(\overline{\mathbf{x}}^{\mathbf{P}}) &= e_{ij}^{I}(\overline{0}) + \tfrac{\partial}{\partial x_r}e_{ij}^{I}(\overline{0})\overline{x}_r^P + \tfrac{\partial^2}{\partial x_r \partial x_s}e_{ij}^{I}(\overline{0})\overline{x}_r^P \overline{x}_s^P + ... \\ \overline{e}_{ij}^{II}(\overline{\mathbf{x}}^{\mathbf{P}}) &= \overline{e}_{ij}^{II}(\overline{0}) + \tfrac{\partial}{\partial \overline{x}_r}\overline{e}_{ij}^{II}(\overline{0})\overline{x}_r^P + \tfrac{\partial^2}{\partial \overline{x}_r \partial \overline{x}_s}\overline{e}_{ij}^{II}(\overline{0})\overline{x}_r^P \overline{x}_s^P + ... \end{aligned} \tag{4.2.23}$$

After the Taylor expansion, the strain rates in Eq.(4.2.23) are expressed in terms of the functions of F^I, F^{II}, D^I and D^{II} and their derivatives evaluated at origin of two coordinates $0\,(x_{1,}x_{2,}x_{3,})$ and $\overline{0}\,(\overline{x}_{1,}\overline{x}_{2,}\overline{x}_{3,})$. The equivalent condition given by Eq.(4.2.1) in Ω_I and Ω_{II} with substitution of Eq.(4.2.21) yields

$$\begin{aligned} \mu_0 \quad \left\{\left[e_{ij}^{I}(\mathbf{x^P}) + e_{ij}^{II}(\mathbf{x^P})\right] - e_{ij}^{*}(\mathbf{x^P})\right\} &= \quad \mu_1^I \left[e_{ij}^{I}(\mathbf{x^P}) + e_{ij}^{II}(\mathbf{x^P})\right] \quad , \quad \text{for } P \text{ in } \Omega_I \\ \mu_0 \quad \left\{\left[\overline{e}_{ij}^{I}(\overline{\mathbf{x}}^{\mathbf{P}}) + \overline{e}_{ij}^{II}(\overline{\mathbf{x}}^{\mathbf{P}})\right] - \overline{e}_{ij}^{*}(\overline{\mathbf{x}}^{\mathbf{P}})\right\} &= \quad \mu_1^{II} \left[\overline{e}_{ij}^{I}(\overline{\mathbf{x}}^{\mathbf{P}}) + \overline{e}_{ij}^{II}(\overline{\mathbf{x}}^{\mathbf{P}})\right] \quad , \quad \text{for } P \text{ in } \Omega_{II} \end{aligned} \tag{4.2.24}$$

where μ_1^I and μ_1^{II} are the viscosity of drop Ω_I and Ω_{II}, respectively.

By substituting of Eq.(4.2.23) into Eq.(4.2.24) and comparing of coefficient of constants and x_r etc., one can obtain

$$\begin{aligned} E_{ij}^{I} &= \tfrac{\mu_0 - \mu_1^I}{\mu_0} \left\{ \begin{array}{c} F_{ijk}^{I}[0]\, f_k^I + D_{ijmn}^{I}[0]\, E_{mn}^{I} + D_{ijmnp}^{I}[0]\, E_{mnp}^{I} + ... \\ + F_{ijk}^{II}[0]\, f_k^{II} + D_{ijmn}^{II}[0]\, E_{mn}^{II} + D_{ijmnp}^{II}[0]\, E_{mnp}^{II} + ... \end{array} \right\} \\ E_{ijr}^{I} &= \tfrac{\mu_0 - \mu_1^I}{\mu_0} \left\{ \begin{array}{c} F_{ijk,r}^{I}[0]\, f_k^I + D_{ijmn,r}^{I}[0]\, E_{mn}^{I} + D_{ijmnp,r}^{I}[0]\, E_{mnp}^{I} + ... \\ + F_{ijk,r}^{II}[0]\, f_k^{II} + D_{ijmn,r}^{II}[0]\, E_{mn}^{II} + D_{ijmnp,r}^{II}[0]\, E_{mnp}^{II} + ... \end{array} \right\}, \quad \text{etc.} \end{aligned} \tag{4.2.25}$$

and

$$
\begin{aligned}
E_{ij}^{II} &= \frac{\mu_0-\mu_1^{II}}{\mu_0}\left\{\begin{array}{c} F_{ijk}^{I}\left[\overline{0}\right]f_k^I + D_{ijmn}^{I}\left[\overline{0}\right]E_{mn}^{I} + D_{ijmnp}^{I}\left[\overline{0}\right]E_{mnp}^{I} + ... \\ +F_{ijk}^{II}\left[\overline{0}\right]f_k^{II} + D_{ijmn}^{II}\left[\overline{0}\right]E_{mn}^{II} + D_{ijmnp}^{II}\left[\overline{0}\right]E_{mnp}^{II} + ... \end{array}\right\} \\
E_{ijr}^{II} &= \frac{\mu_0-\mu_1^{II}}{\mu_0}\left\{\begin{array}{c} F_{ijk,r}^{I}\left[\overline{0}\right]f_k^I + D_{ijmn,r}^{I}\left[\overline{0}\right]E_{mn}^{I} + D_{ijmnp,r}^{I}\left[\overline{0}\right]E_{mnp}^{I} + ... \\ +F_{ijk,r}^{II}\left[\overline{0}\right]f_k^{II} + D_{ijmn,r}^{II}\left[\overline{0}\right]E_{mn}^{II} + D_{ijmnp,r}^{II}\left[\overline{0}\right]E_{mnp}^{II} + ... \end{array}\right\}, \quad \text{etc.}
\end{aligned}
\tag{4.2.26}
$$

The functions $F_{ijk}^{I}[0]$, $F_{ijk}^{II}\left[\overline{0}\right]$, $D_{ijmnp}^{I}[0]$, $D_{ijmnp}^{II}\left[\overline{0}\right]$, $D_{ijmn,r}^{I}[0]$ and $D_{ijmn,r}^{II}\left[\overline{0}\right]$ are all zero due to the definition, then, Eqs.(4.2.25) and (4.2.26) can be simplified

$$
\begin{aligned}
\left\{\begin{array}{c} \left[D_{ijmn}^{I}[0]-\beta^I\cdot I_{ijmn}\right]E_{mn}^{I} + ... \\ +D_{ijmn}^{II}[0]\,E_{mn}^{II} + D_{ijmnp}^{II}[0]\,E_{mnp}^{II} + ... \end{array}\right\} &= -F_{ijk}^{II}[0]\,f_k^{II} \\
\left\{\begin{array}{c} \left[D_{ijmnp,r}^{I}[0]-\beta^I\cdot I_{ijmnpr}\right]E_{mnp}^{I} + ... \\ +D_{ijmn,r}^{II}[0]\,E_{mn}^{II} + D_{ijmnp,r}^{II}[0]\,E_{mnp}^{II} + ... \end{array}\right\} &= -\left\{F_{ijk,r}^{I}[0]\,f_k^I + F_{ijk,r}^{II}[0]\,f_k^{II}\right\}, \quad \text{etc.}
\end{aligned}
\tag{4.2.27}
$$

and

$$
\begin{aligned}
\left\{\begin{array}{c} \left[D_{ijmn}^{II}\left[\overline{0}\right]-\beta^{II}\cdot I_{ijmn}\right]E_{mn}^{II} + ... \\ +D_{ijmn}^{I}\left[\overline{0}\right]E_{mn}^{I} + D_{ijmnp}^{I}\left[\overline{0}\right]E_{mnp}^{I} + ... \end{array}\right\} &= -F_{ijk}^{I}\left[\overline{0}\right]f_k^I \\
\left\{\begin{array}{c} D_{ijmn,r}^{I}\left[\overline{0}\right]E_{mn}^{I} + D_{ijmnp,r}^{I}\left[\overline{0}\right]E_{mnp}^{I} + ... \\ \left[D_{ijmnp,r}^{II}\left[\overline{0}\right]-\beta^{II}\cdot I_{ijmnpr}\right]E_{mnp}^{II} + ... \end{array}\right\} &= -\left\{F_{ijk,r}^{I}\left[\overline{0}\right]f_k^I + F_{ijk,r}^{II}\left[\overline{0}\right]f_k^{II}\right\}, \quad \text{etc.}
\end{aligned}
\tag{4.2.28}
$$

where

$$
\beta^I = \frac{\mu_0}{\mu_0-\mu_1^I} \quad \text{, and} \quad \beta^{II} = \frac{\mu_0}{\mu_0-\mu_1^{II}} \tag{4.2.29}
$$

Solving the linear equation system in Eqs.(4.2.27) and (4.2.28), four unknowns E_{ij}^{I}, E_{ijk}^{I}, E_{ij}^{II} and E_{ijk}^{II} can be determined, and velocity and pressure field can be obtained.

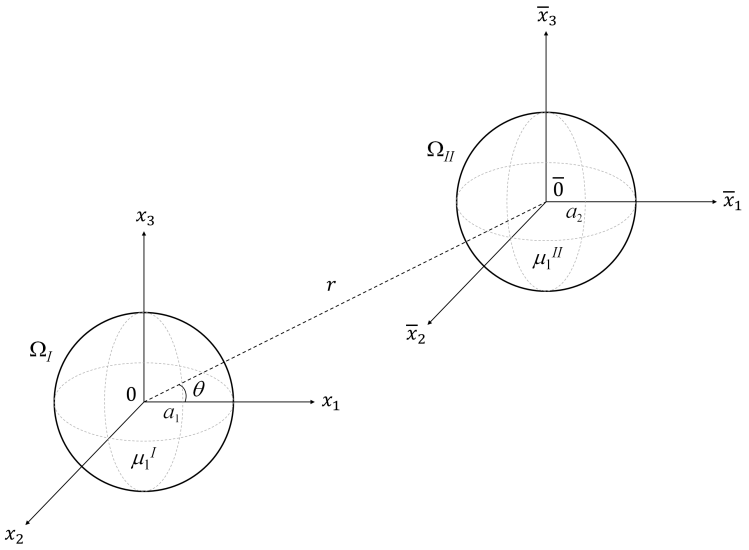

Figure 4.2.1: Geometry of a pair of spherical drops

4.3 Case Studies

When a pair of spherical drops move together in different viscous fluid, it can be imaged that the motion of either one drop will be interacted by the other one and become different compared with the either one moving in isolation. The amplitude of interaction will be affected by the parameters of (1) size; (2) viscosity and (3) corresponding position of drops, and the effect produced by these varied parameters are studied as follows:

Table 1 shows the translational velocity of pair of identical rigid spheres, which the applied body force $\mathbf{f}^I = \mathbf{f}^{II} = (0, 0, 1)$ and radius a_1 and a_2 are both equal to 1, raising in the fluid ($\mu_0 = 1$) when the corresponding distance r between two spheres and angle θ varies. The first row of the table shows the exact solution, as mentioned in Eq.(4.1.1), calculated by Batchelor (1972). The second row of the table shows the approximations of average interior velocity obtained by the present method (EIM) when the eigenstains are assumed as first degree polynomials in the position coordinates. Furthermore, when a pair of identical horizontally oriented solid spheres $\left(\mu_1^I = \mu_1^{II} = \infty\right)$ with different r , the distance between centers of spheres, are raising in the fluid ($\mu_0 = 1$), and the body force applied on both spheres are the same, $\mathbf{f}^I = \mathbf{f}^{II} = (0, 0, 1)$, the distribution of x_3 component of velocity

field along x_1 axis are plotted in Figure 4.3.1. It is obviously observed that the average velocity within both particle will be reduced when the distances between two spheres is increasing, in other words, the longer distance, the smaller interaction between two spheres. Besides, the nonuniform interior velocity, where the inner bound is higher than outer bound, demonstrates the body rotation of both solid spheres when they are horizontal oriented; and the body rotation become slower while the interval is larger.

Table 4.1: The x_3 component of translational velocity of each one of a pair of identical rigid spheres for body force $f_3^I = f_3^{II} = 1$ applied on Ω^I and Ω^{II} with $a_1 = a_2 = 1$

Distance	$r = 4$			$r = 6$			$r = 8$		
Angle (θ)	0	$\frac{\pi}{4}$	$\frac{\pi}{2}$	0	$\frac{\pi}{4}$	$\frac{\pi}{2}$	0	$\frac{\pi}{4}$	$\frac{\pi}{2}$
Batchelor's (1972)	0.2655	0.2824	0.2994	0.2505	0.2633	0.2761	0.2432	0.2532	0.2632
Present method (1^{st} degree polynomial)	0.2656	0.2825	0.2993	0.2505	0.2633	0.2761	0.2433	0.2533	0.2633

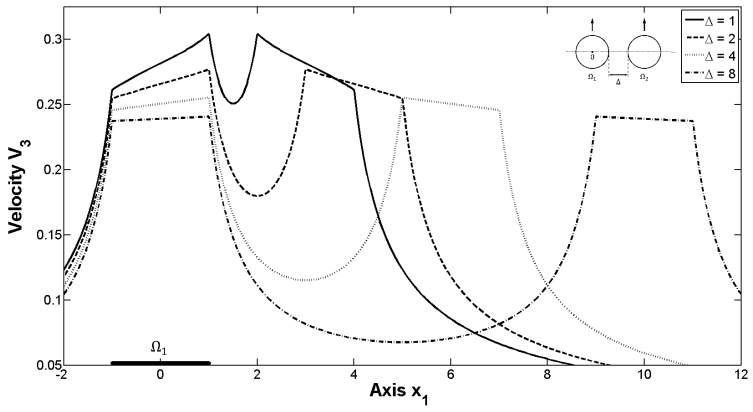

Figure 4.3.1: The distribution of x_3 component of velocity field along x_1 axis; applied body force $f_3^I = f_3^{II} = 1$, viscosity of fluid $\mu_0 = 1$, viscosity of spheres $\mu_1^I = \mu_1^{II} = \infty$, size of drops $a_1 = a_2 = 1$.

Figure 4.3.2 shows the distribution of x_3 component of velocity field along x_1 axis when a pair of identical horizontally oriented spherical drops with different viscosity $\left(\mu_1^{II} \neq \mu_1^I = \infty\right)$

are raising in the fluid ($\mu_0 = 1$), and the body force applied on both spheres are the same, $\mathbf{f}^I = \mathbf{f}^{II} = (0, 0, 1)$. The effect on the interior velocity field of Ω_1, which is the left one with center at origin in Figure 4.2.1, produced by the viscosity change of Ω_2 is very slight, even though the change does influence the interior and average velocity of Ω_2. The x_3 component of raising velocity at center of first drop Ω_1 will be slightly increased from 0.2654 to 0.2656, if the viscosity of second drop Ω_2 is changed from 2 to 100.

Figure 4.3.3 shows the similar results of distribution of x_3 component of velocity field along x_1 axis, all the parameters belong to both drops are the same, including viscosity $\left(\mu_1^I = \mu_1^{II} = \infty\right)$ and applied body force $\mathbf{f}^I = \mathbf{f}^{II} = (0, 0, 1)$, except the size $a_2 \geq a_1 = 1$. The viscosity of fluid μ_0 and distance Δ here keeps 1 and 2 respectively. It is investigated that the size of second drop Ω_2, the right one in Figure 4.2.1, significantly influences the average velocity of first drop Ω_1. The x_3 component of raising velocity at center of first drop Ω_1 will be increased from 0.3347 to 0.5738, if the radius of second drop Ω_2 is expanded from 1 to 2.

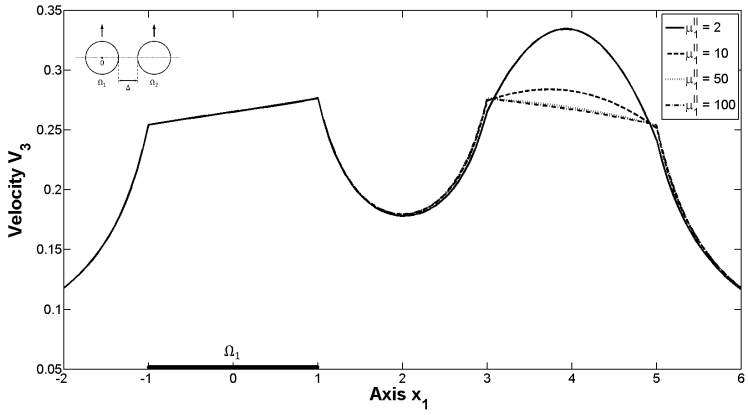

Figure 4.3.2: The distribution of x_3 component of velocity field along x_1 axis; applied body force $f_3^I = f_3^{II} = 1$, distance $\Delta = 2$, viscosity of fluid $\mu_0 = 1$, size of drops $a_1 = a_2 = 1$, viscosity of spheres $\mu_1^I = \infty$, but μ_1^{II} varies.

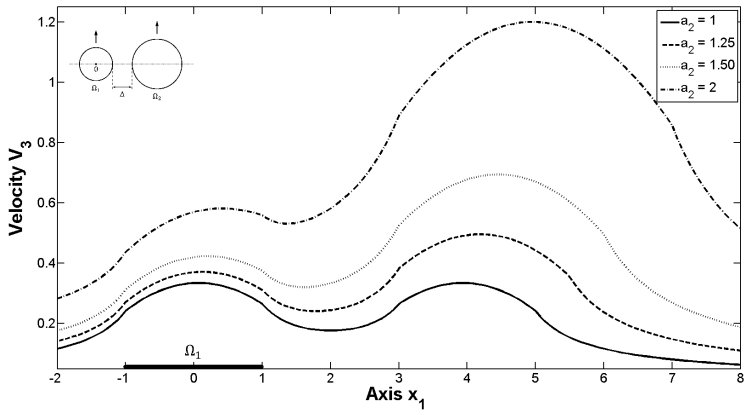

Figure 4.3.3: The distribution of x_3 component of velocity field along x_1 axis; applied body force $f_3^I = f_3^{II} = 1$, distance $\Delta = 2$, viscosity of fluid $\mu_0 = 1$, viscosity of spheres $\mu_1^I = \mu_1^{II} = \infty$, size of drops $a_1 = 1$, but a_2 varies.

Chapter 5

Fabrication of Aluminum and High-Density Polyethylene Functionally Graded Material by the Vibration Method

Vibration method is one of the numerous ways to fabricate functionally graded materials (FGMs). This chapter introduces a vibration method to fabricate the thin interlayer of aluminum (Al) and high-density polyethylene (HDPE) FGMs, whose thermal conductivity is gradually transited from well conductive side to highly insulative side, for solar roofing panels. Besides, under high-frequency vibration, the particle segregation of larger aluminum particles settling in the concentrated suspension of smaller high-density polyethylene is investigated. Altering experimental parameters including vibration time and amplitude, the suspension exhibits different particle segregation patterns: uniform-like, graded and bi-layered after the vibration process. The small cylinder films of Al-HDPE system FGMs has be fabricated by the vibration method with appropriate experimental parameters; this method can also be practically extended to the mass manufacture of large-scale thin interlayer for solar roofing

panel system in the future.

5.1 Overview

For the fabrication of FGM, various manufacture methods have been studied and developed (Suresh and Mortensen, 1998; Miyamoto et al., 1999). Powder metallurgy (PM) is the one of the most popular ways including powder stacking, slip casting, plasma spraying, electrophoretic deposition, gravity sedimentation and vibration etc (Neubrand et al., 2003). However, some kinds of PM methods, such as powder stacking and sequential slip casting (Moya et al., 1992), will make stepwise gradient of material with sharp interfaces resulting in the phenomenon of residual thermal stresses and thermal expansion mismatch along the interfaces. In this chapter, the fundamental theories and previous experimental works relative to vibration method are introduced, as well as our present work.

Different species of particles in a concentrated suspension or a granular medium may segregate under tapping, shaking, vibration or flow. Understanding of particle segregation behavior, including Brazil-nut effect (BN), reverse Brazil-nut effect (RBN) and shear-induced segregation, is crucial for fabrication of FGM by the vibration method. Brazil-nut effect is a phenomenon indicating the hard and larger particles typically rise to the top while a vertical vibration is applied; subsequently, the disordered mixture will gradually become ordered (Jullien and Meakin, 1990). Meanwhile, due to convection mechanism (Knight et al., 1993) and percolation into voids between large particle during shacking (Jullien and Meakin, 1990; Rosato et al., 1987), the small particles settle down to the bottom. The segregation behavior not only depends on the particle size, but also the density and surface roughness (Mobius et al., 2001; Plantard et al., 2006). On the other side, reverse Brazil-nut effect, where the small particles tend to rise up to the top, is discovered by Shinbrot and Muzzio (1998). Moreover, Hong et. al. (2001) demonstrated the crossover between BN and RBN relative to the diameter and mass ratios between two species of particles and the spatial dimension of simulation.

According to the aforementioned principles, the vibration method has been applied to fabricate FGM with continuous variation for eliminating the interfaces successfully in several similar setups and process. C.-Y. Lin et al. (1999) have obtained silicon carbide / aluminum 2124 alloy (SiCp/Al 2124) FGM, combination of vertical and rotative vibration is involved in the manufacture process and followed by powder stacking layer by layer with different volume fraction of SiCp. J. Fiscina et al. applied the Brazil-nut approach to fabricate tungsten-cooper (W-Cu) graded alloy (Fiscina et al., 2003, 2004; Ilic et al., 2007). A.J. Ruys et al. (1996) have developed the thixotropic casting, casting of thixotropic and concentrated suspensions under vibration, to produce ceramic-metal FGM.

In this present work, aluminum and high-density polyethylene functionally graded material (Al-HDPE FGM) is successfully produced by vibration method. Coarse Al powder, fine HDPE powder and small portion of ethanol are mixed as high concentrated suspension. Under vibration with different experimental parameters, the suspension of Al and HDPE will become graded, bi-layered and uniform-like deposition. After stages of dry, melt and solidification, the graded solid cylinder is fabricated; and the gradation of volume fraction of aluminum is determined by density measurement (Rice method) along the depth direction of specimen. In the future, the simulation of this work will be developed for further design optimization.

5.2 Experiment

The vibration method is designed to fabricate the aluminum (Al) and high-density polyethylene (HDPE) functionally graded material (FGM) using a vibration table. This equipment is used to apply the vertical and horizontal vibration to the high-concentrated suspension of Al and HDPE. According to the size and density, the motion of each particle differs under the vibration; the graded deposition can be obtained if the size of materials and experimental parameters are appropriately selected. Unlike the sedimentation method mentioned in

Chapter 2, the vibration method is more suitable for mass production of AL-HDPE FGM as a rapid and economy manufacture process.

5.2.1 Apparatus and Material Preparation

A vibration table, as shown in Figure 5.2.1(a), produces the vibration to the specimen fixed on the table; the frequency and amplitude are controlled by the panel, see Figure 5.2.1(b). Three different levels of vibration are selected for the experiment, the corresponding frequency amplitude are measured and illustrated in Figure 5.2.2, and the vibration behavior of the table is vertical dominant with minor horizontal motion.

For the material preparation, the coarse aluminum powder (Al-111) with the size from 100 to 600 μm is chosen to mix with the finer high-density polyethylene (HDPE) powder with the size from 1 to 100 μm. The particle size distribution of both material are measured by particle analyzer (Mastersizer 2000, Malvern) and plotted in Figure 5.2.3. Besides, under scanning electron microscope (SEM) observation, the shape of aluminum and high-density polyethylene powder is irregular and spherical respectively, see in Figure 5.2.4.

(a) (b)

Figure 5.2.1: Vibration table configuration: (a) outlook, (b) control panel

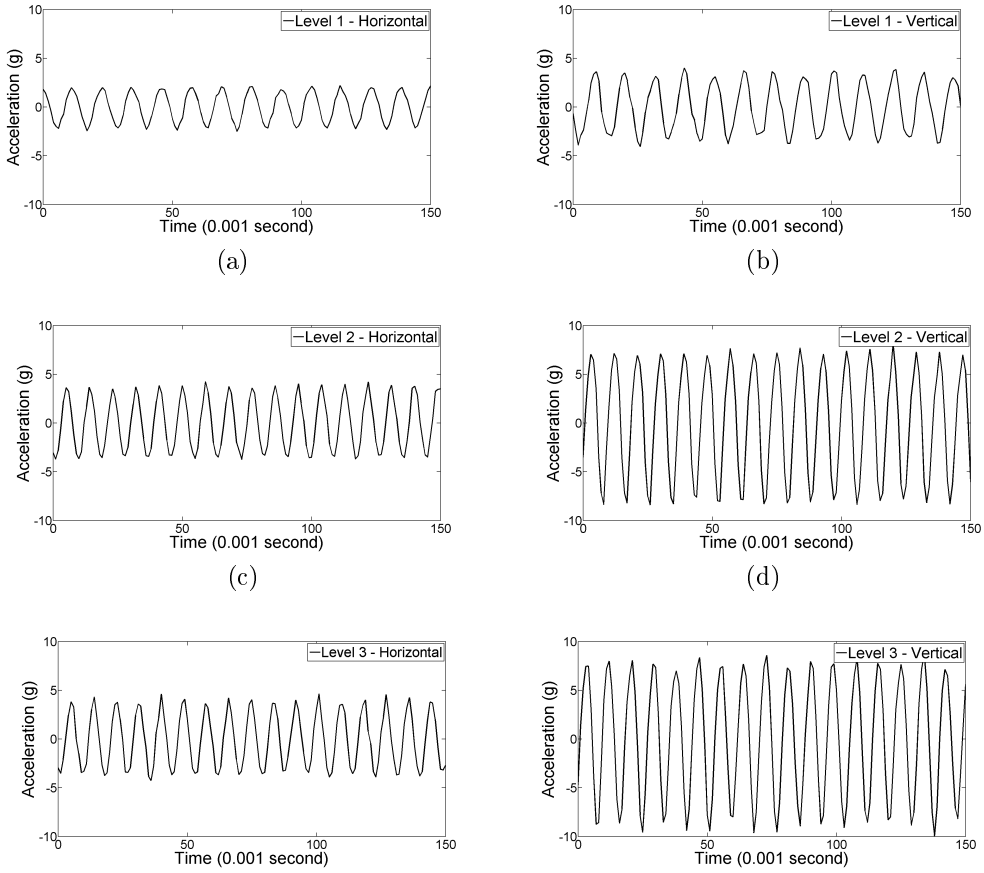

Figure 5.2.2: The corresponding vibration frequency and amplitude for (a) horizontal and (b) vertical direction of level 1; (c) horizontal and (d) vertical direction of level 2; and (e) horizontal and (f) vertical direction of level 3

5.2.2 Experimental Procedure

The whole test procedure is straightforward and containing two major processes, which details are described as follows:

Production of graded deposition

Beforehand, the goal is to create the AL-HDPE FGM with the gradation of volume fraction of aluminum from 0 to 50 %, thus, the appropriate volume ratio of aluminum to HDPE is

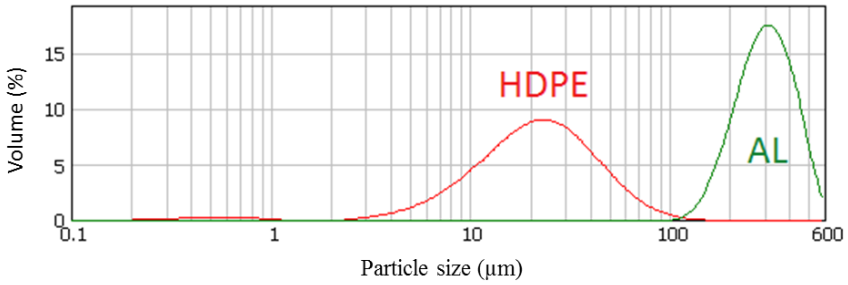

Figure 5.2.3: Particle size distributions of aluminum (Al-111) and high-density polyethylene

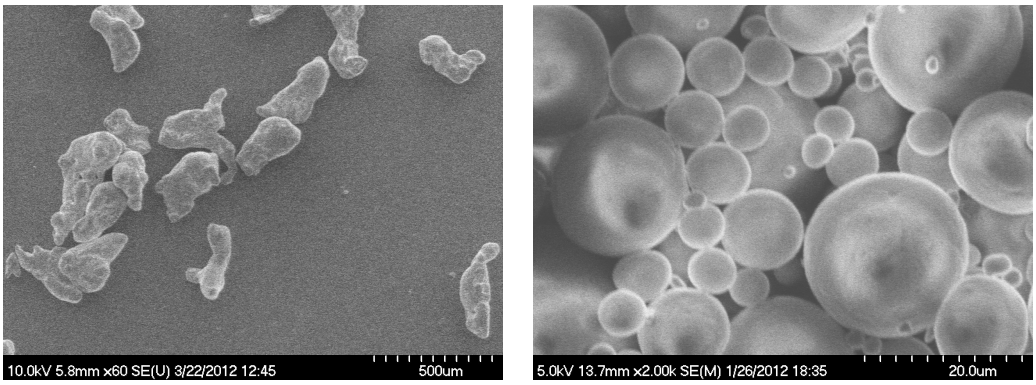

(a) (b)

Figure 5.2.4: SEM observation of (a) aluminum (Al-111); and (b) high-density polyethylene powder

chosen as 1 to 3. The solid loading, weight ratio of powder to solution, keeps 72% (wt.) in the experiment. At the beginning, 7.29 g aluminum powder, 7.71 g high-density polyethylene powder and 6 g ethanol are introduced as aforementioned proportion in the glass cylinder. Next, ultrasonic tank and mechanical mixer are simultaneously used to stir the mixture for 1 hour, as shown in Figure 5.2.5(a), until it becomes visually uniform. Shortly after, the glass cylinder is fixed on the vibration table by plastic clamp; the graded deposition (Figure 5.2.6) is formed after proper vibration is given.

Solidification process

After draining the ethanol off and air-dry the specimen for 24 hours, the deposition becomes completely dry. Then, the deposition is placed into the metal mold, applied with 400 g

weight and heated in the vacuum oven under 180 $^{\circ}C$ for 10 hours. Eventually, the graded solid cylinder will be formed after cooling and curing the sample. The cross section of graded solid cylinder is observed by regular and stereo microscopes as shown in Figure 5.2.7.

(a) (b)

Figure 5.2.5: The fabrication process of (a) mixing; and (b) vibrating the suspension

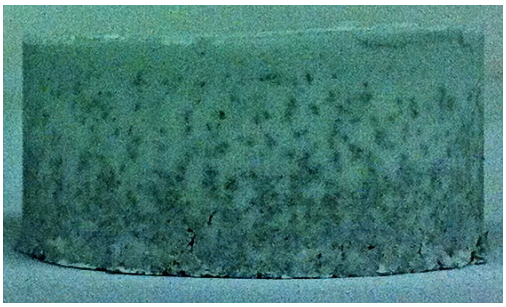

Figure 5.2.6: Graded deposition obtained after proper vibration

5.3 Results and Discussions

During the process of vibration, varied experimental parameters including amplitude, frequency and time of vibration will affect the segregation of aluminum and HDPE particles,

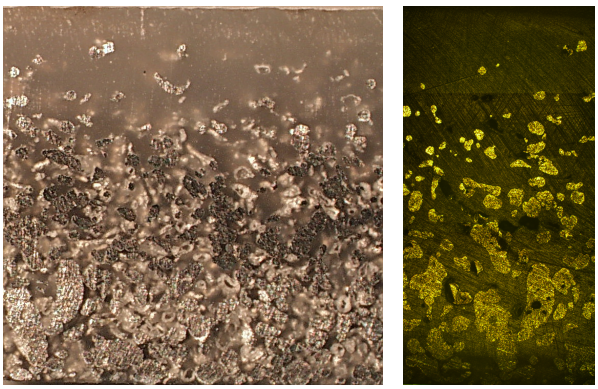

(a) (b)

Figure 5.2.7: Observation of graded solid cylinder by: (a) stereo microscope (b) microscope

as well as the texture of the deposition. Three different levels of vibration, whose corresponding frequency and amplitude are measured in Figure 5.2.2, are chosen to apply on the homogenous mixture for 0, 15, 30 and 60 seconds. The results after vibration are displayed in Figure 5.3.1. There is no gradation occurred even though level 1 vibration has already continued for 60 seconds. However, the graded deposition could be created while the mixture is stood under level 2 and 3 vibration for 30 and 15 seconds, respectively. Subsequently, all aluminum particles tended settling down to the bottom during more longer vibration.

To analyze the gradation, the deposition is divided into five layers along the depth direction after air-dry stage, and the density of each layer is measured by the Rice method (ASTM D-2041) to determine the volume fraction of aluminum. The uniform-like, graded and bi-layered deposition are produced by the varied vibration parameters, and the results of gradation are consistent between Figure 5.3.1 and Figure 5.3.2. The gradation of deposition, which the range of volume fraction of aluminum is from 0 to approximately 50 %, is stable after level 3 vibration for 15 seconds. Also, after 30 seconds vibration of level 2, the gradation is exhibited but not as smooth as the result from previous setup. In addition, the bi-layered and uniform-like gradation are induced by the longer vibration and no vibration, respectively.

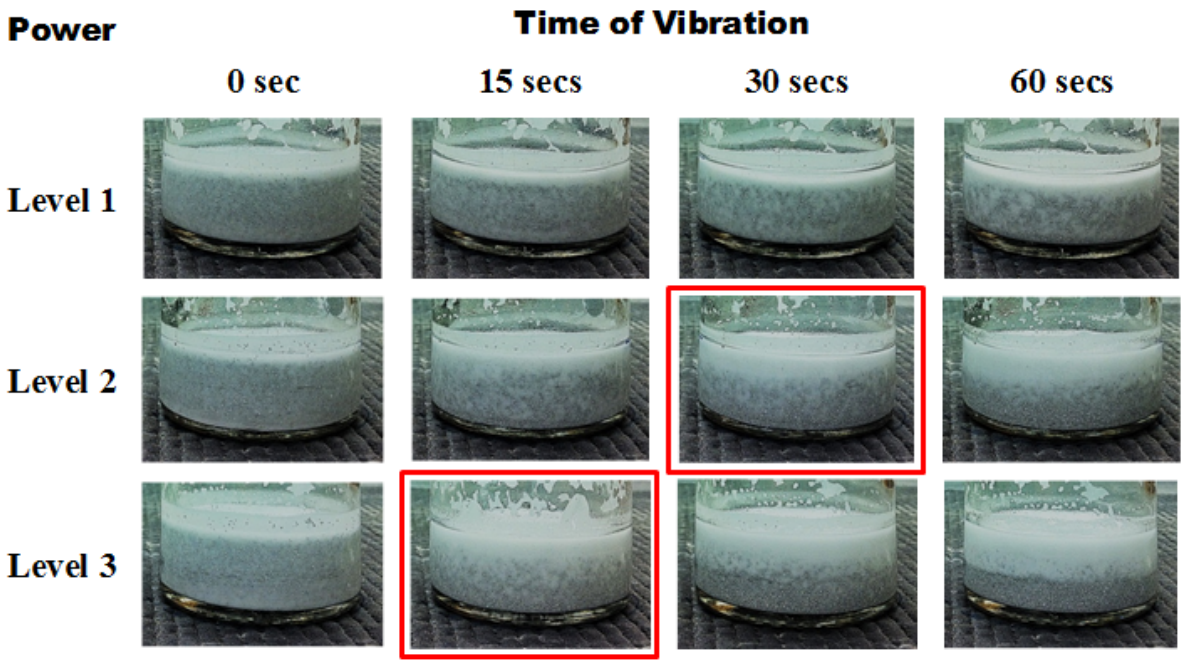

Figure 5.3.1: Observation of vibration process

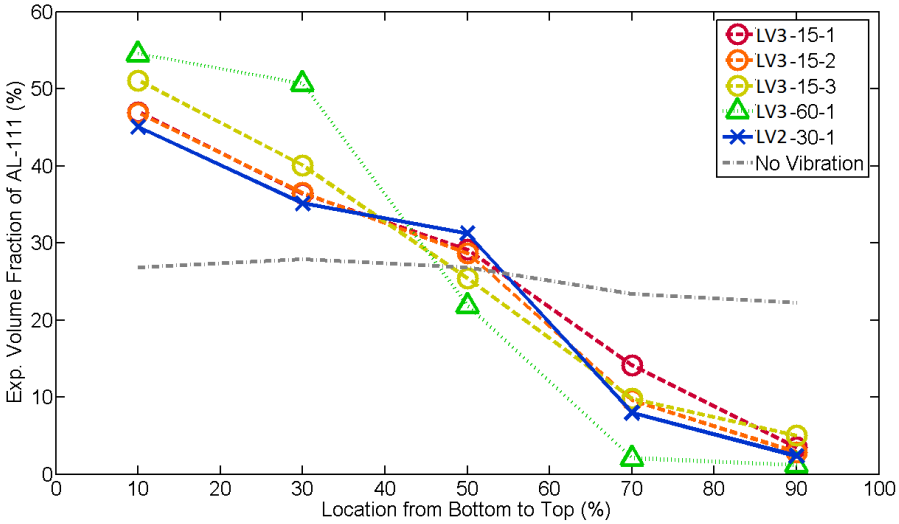

Figure 5.3.2: Comparison between different cases for volume fraction of aluminum at location from the bottom to the top

Compared with the sedimentation method, the vibration method is more practical for mass production of Al-HDPE FGMs for the following reasons: (1) Quicker fabrication process - It is time-saving to create graded deposition by vibration method, on the contrary, it will

takes hours of the sedimentation method. (2) Material saving - the solid loading chosen in sedimentation method is 20% whereas the vibration method is 72%; in other words, the consumption of ethanol become relatively less if the vibration method is applied even though it will be recycled for multiple usage. This test procedure is the framework and will be extended to manufacture the original size ($2^{'} \times 2^{'}$) of Al-HDPE FGM interlayer for solar roofing panel system in the near future. Quantitative simulation and modeling of the loss of the stability of the uniform mix under vibration is underway.

Chapter 6

Performance of Novel Hybrid Solar Roofing Panel

A hybrid solar panel has been invented to integrate photovoltaic (PV) cells onto a substrate through a functionally graded material (FGM) with water tubes cast inside, through which water serves as both heat sink and solar heat collector. Therefore, the PV cells can work at a relatively low temperature while the heat conduction to the substrate can be minimized. Solar panel prototypes have been fabricated and tested at different water flow rates and solar irradiation intensities. The temperature distribution in the solar panel is measured and simulated to evaluate the performance of the solar panel. The finite element simulation results are very consistent with the experimental data. The understanding of heat transfer in the hybrid solar panel prototypes will provide a foundation for future solar panel design and optimization. The finite element model is general and can be extended for different material design and other size of panels.

6.1 Overview

Solar panels have become a very promising and popular approach to collect solar energy. Currently solar panel products in market mainly use photovoltaic (PV) cells for the elec-

tricity generation. PV technology has achieved tremendous progress since the invention in 1839. However, there is still significant research need in the aspects of efficiency improvement and life-cycle cost reduction. For the single crystalline single junction Si technology, the conversion efficiency keeps lower than 30% (Levy, 2007; Shockley and Queisser, 1961). Thus a large portion of solar energy is wasted through heat dissipation (Nozik, 2001; Odeh and Behnia, 2009). Although some emerging technologies can considerably improve energy utilization efficiency, such as multi-junction cells (Kaplar et al., 2000), optical frequency shifting (Trupke et al., 2002), multiple exciton generation cells (Schaller and Klimov, 2004), hot carrier cells (Ross, 1982) and concentration photovoltaic system (Vincenzi et al., 2009), these technologies require high cost and complex service conditions, and thus have not been commercially used in solar roofing panel yet.

Solar thermal technology provides another way to use the thermal energy of solar insolation. Solar thermal collectors have been applied to domestic (bath, cooking, space heating and swimming pool heating etc.) and commercial sectors (pre-heating of boiler and hospitals etc.). Typically, energy payback time (EPBT) for solar thermal system is much less than that of PV systems. The EPBT of PV system can be reduced by using it in a hybrid system integrating PV with solar thermal components, such as hot water (HW) tubes (Crawford et al., 2006). The combination of the above two approaches is not a simple superposition of the materials and costs, but provides a viable solution to significantly increase overall energy utilization efficiency while alleviating the disadvantages of a single approach (Zondag, 2008). A PV-thermal collector enables heat harvesting while improving the PV utilization efficiency by controlling the temperature of PV modules. Currently, some groups have studied the performance of PV-thermal hybrid systems (Vorobiev et al., 2006; Kraemer et al., 2008), which provide the good justifications of the solar hybrid approaches.

In this work, we developed a novel functionally graded material (FGM) based hybrid solar panel as Figure 1.3.4 (Yin, 2009). A PV surface layer, transferring the photo energy into electricity, is bonded to a structural substrate plate through a functionally graded ma-

terial (FGM) interlayer. The FGM contains aluminum powder dispersed in a high density polyethylene (HDPE) matrix with a graded microstructure seen in the left top of Figure 1.3.4. Water pipelines are cast within the FGM to control the panel's temperature. The substrate, namely, plastic lumber made of recycled polymer, provides mechanical loading support and heat insulation of the roof.

FGMs are characterized by continuous variation of the volume fraction of the constituents (Miyamoto et al., 1999). FGMs have attracted significant interests among researchers and engineers because of their unique thermo-mechanical properties and microstructures (Yin et al., 2008c, 2007, 2004). The effective material properties, such as thermal conductivity, vary continuously in the gradation direction and keep constant in the plane normal to the gradation direction (Yin et al., 2008c). In the following experiment, the Al powder concentration gradually decreases from the top to the bottom. Thus the thermal conductivity also decreases gradually from the top to the bottom of the FGM layer.

The remainder of this chapter is organized as follows: Section 6.2 introduces the hybrid solar panel prototype fabrication, and testing instruments and procedure. In Section 6.3, the irradiation space uniformity of the metal halide lamp and the temperature distribution of the solar panel are characterized. A finite element model (FEM) is implemented using ABAQUS to simulate the thermal transfer characteristics of the solar panel. The FEM results are compared with the experimental data. Finally, the overall energy efficiency of the solar panel is evaluated based on the testing results.

6.2 Experimental Setup and Procedure

6.2.1 Solar Panel Fabrication

The hybrid solar panel has been fabricated for photovoltaic (PV), hot water utilization through a multilayered configuration. The PV cells used in the panels are commercial single crystalline Si solar cells with an open circuit voltage V_{oc} of 0.55 V, short circuit current I_{sc} of 4400 mA and an energy conversion efficiency η_{pv} of 13% at room temperature (25°C). The

length, width and thickness of the solar cell are 12.5 cm, 12.5 cm and 270 μm, respectively. Pure Al powder and high density polyethylene (HDPE) matrix are used to fabricate the FGM layer. The thermal conductivity of Al and HDPE are 238 $W/m.K$ and 0.26 $W/m.K$, respectively. The HDPE and Al powder are mixed layer by layer with a continuously changing proportion such as 50% Al volume fraction in the bottom and pure HDPE in the top of a mold. The mix within the mold is baked in a vacuum at 200°C for 1.5 hrs and is then solidified with dimensions of 30.5 cm × 30.5 cm × 1.5 cm. A vacuum sintering process is employed to bond the FGM layer with the plastic lumber substrate which is made of recycled polymeric materials. The water tubes made with copper (Cu) pipes with a diameter of ~6 mm are cast into the FGM layer with a separation of 2.5 cm. Thermal conductive paste with a conductivity of 1.9 $W/m.K$ is used as an adhesive between the PV, and FGM layers. The complete panels are degassed in a vacuum oven at 90°C for 2 hrs.

The photovoltaic (PV) layer can transfer a portion of the solar energy to electricity. The thin PV layer improves the heat conduction and structural integrity within the panel, and protects the polymer materials underneath from UV radiation. The high percentage of aluminum (Al) powder in top surafce of the FGM makes rapidly heat transfer into the water tubes, but below them the heat conduction is blocked by the HDPE and the plastic lumber substrate. The hot water, whose temperature is partially controlled by the flow rate, can be directly utilized by water heating systems for domestic usage.

6.2.2 Testing Method

Eight T type thermal couples ($+/-1°C$) are attached on the panels to detect the temperature distribution of the PV cells and water. The solar panels are tested in a solar room equipped with a metal halide lamp, which can provide irradiation up to 4 KW/m^2. The panel is fixed on a wood frame with 45 degree tilt angle so that the panel surface is normal to the irradiation. A pyranometer is used to measure and calibrate the solar irradiation. A mass flow meter is used to control the cooling water flow rate. The experimental data is collected

with the data acquisition system. The whole system testing set up is shown in Figure 6.2.1.

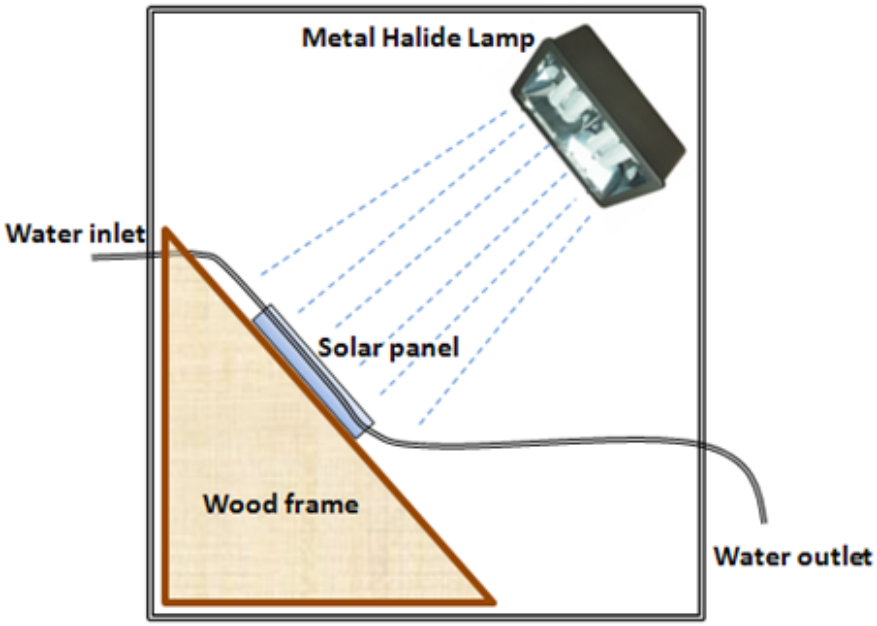

Figure 6.2.1: Solar panel testing setup

The performance of the solar panels are characterized in the following way: The solar panels are put in the solar room under different irradiations of 850 W/m^2 and 1100 W/m^2. Before the water flow starts, the solar panel surface temperature is automatically measured with an interval of 2 seconds until the panel reaches a stabilized temperature. Then the water flow is introduced with the inlet water temperature at $20°C$. The flow rate is controlled by the mass flow meter at 33 ml/min and 66 ml/min for the irradiations of 850 W/m^2 and 1100 W/m^2, respectively. These water flow rates are determined by some trial-error tests so that the panel can be effectively cooled and the outlet water temperature keeps in a range between $32-34°C$. The irradiation levels are chosen to cover a small range around the AM1.5 (1000 W/m^2) condition. The PV cell and water temperatures are recorded continuously until the panel temperature stabilizes again.

6.3 Results and Discussions

6.3.1 Irradiation Space Uniformity

During the tests, we use a metal halide lamp to simulate solar irradiation. The space uniformity of the irradiation is examined through 25 point measurement on the panel surface where is equally divided into 25 square areas. The 25 measuring points are uniformly distributed in the 25 square areas. Two different irradiation settings of 850 W/m^2 and 1100 W/m^2 are tested. The two dimensional irradiation contour maps are shown in Figure 6.3.1. Irradiation maps are approximately symmetric within the panel with respect to the center point which receives the highest irradiations. It is reasonable as the panel surface is normal to the irradiation with the center aligned to the lamp. The coefficients of variation of the 25 point measurements are 2.9% and 3.3% for the irradiation of 850 W/m^2 and 1100 W/m^2, respectively.

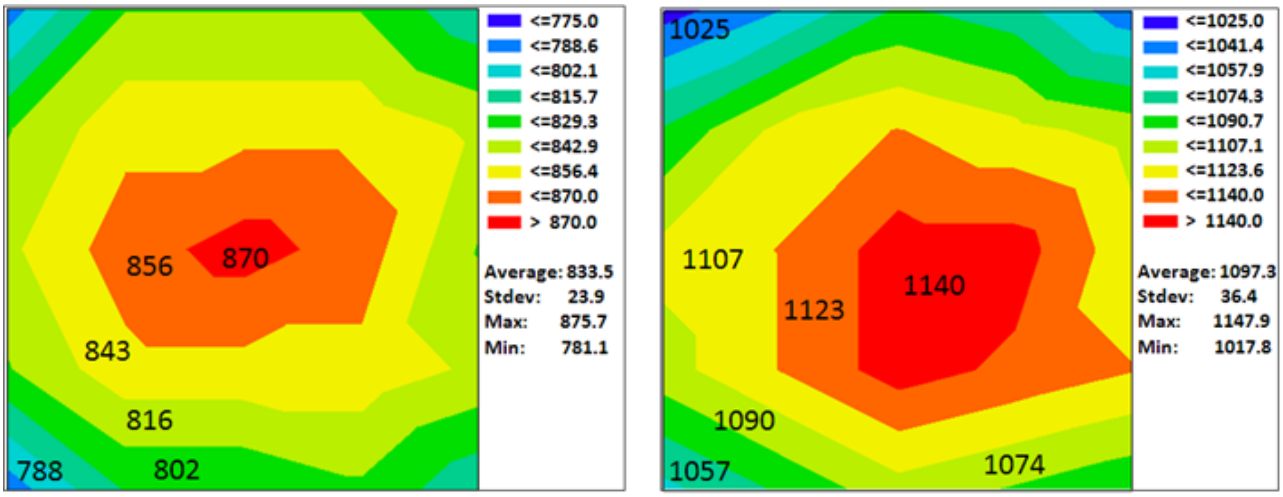

(a) (b)

Figure 6.3.1: Contour map of the solar irradiation on the panel surface for (a) 850 W/m^2 and (b) 1100 W/m^2

6.3.2 Temperature Distribution

Seven thermal couples are attached on the surface of the solar panel to evaluate the temperature distribution, as shown in Figure 6.3.2, which also indicates the direction of water flow along the water tube by the arrows. For the data analysis conveniences, the sensor point number sequence follows the water flow direction. The eighth thermal couple is attached in the outlet water tube to test the outlet water temperature.

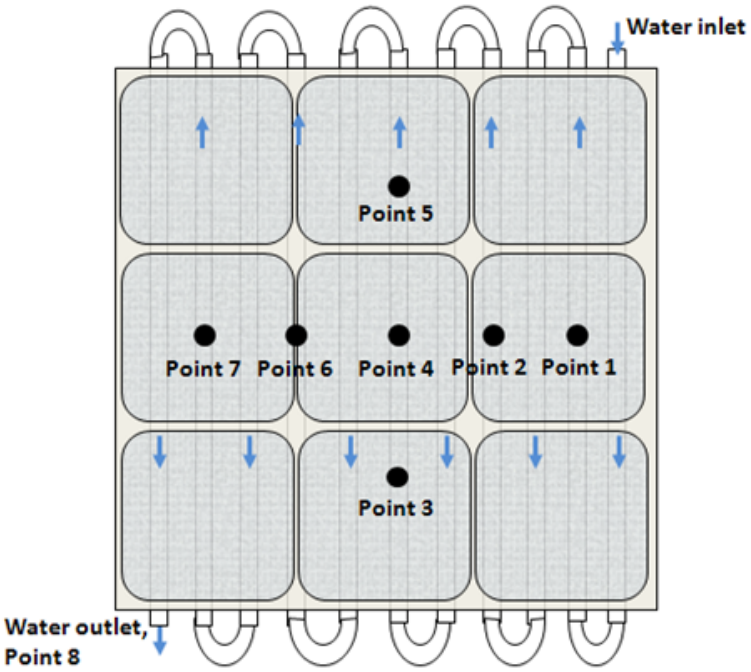

Figure 6.3.2: Position of thermal couples and water flow direction

Figure 6.3.3(a) shows the equilibrium temperature of the 8 points without and with water flow of 33 ml/min under the irradiation of 850 W/m^2, and Figure 6.3.3(b) without and with water flow of 66 ml/min under the irradiation of 1100 W/m^2. It can be seen that even the irradiation map has the center high pattern, most region of solar panel still can be uniformly heated up, as the variation of the high equilibrium temperatures among the 7 points is within $+/-2°C$. With the water flow introduced, the temperatures of the 7 points monotonically increase with the point number sequence. As the higher the point number, the more thermal energy the water absorbed, and the less the cool effect. Figure 6.3.4 shows the temperature

variation with time at two different irradiations and water flow conditions. Before the water flow starts, the solar panel surface temperatures increase fast with time and then gradually saturate at around $50°C$ and $55°C$ at the time around 7700 s ~ 8100 s for the irradiation of 850 W/m^2 and 1100 W/m^2, respectively. With the water flow introduced, the temperatures sharply dropped and then stabilized at around $32°C$ ~ $38°C$. The outlet water temperature is around $32°C$ ~ $34°C$. These results show that water tubes integrated with FGM layers can effectively cool the PV cells.

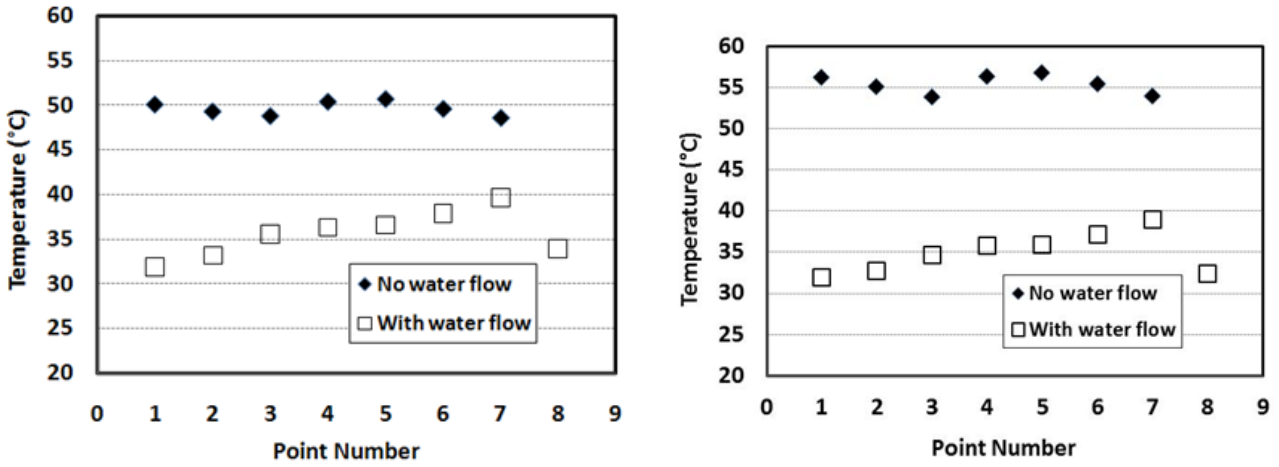

(a) (b)

Figure 6.3.3: Equilibrium temperatures of each point at conditions of (a) irritation: 850 W/m^2, water flow rate: 33 ml/min, (b) irritation: 1100 W/m^2, water flow rate: 66 ml/min

6.3.3 Finite Element Simulation

FEM Model and multilayer discretization

A commercial software package ABAQUS is used to simulate heat transfer across the solar panel. The model and grid generation of solar panel is shown in Figure 6.3.5. The panel is discretized into eight layers in vertical direction including PV cells, thermal conductive paste, and six FGM layers with gradient variation of percentage of HDPE and aluminum. Within layer 4 and 5, there are 11 water tubes uniformly distributed. The thickness of copper tube is 1 mm and inner diameter is 4 mm. More grids are generated around tube area for better

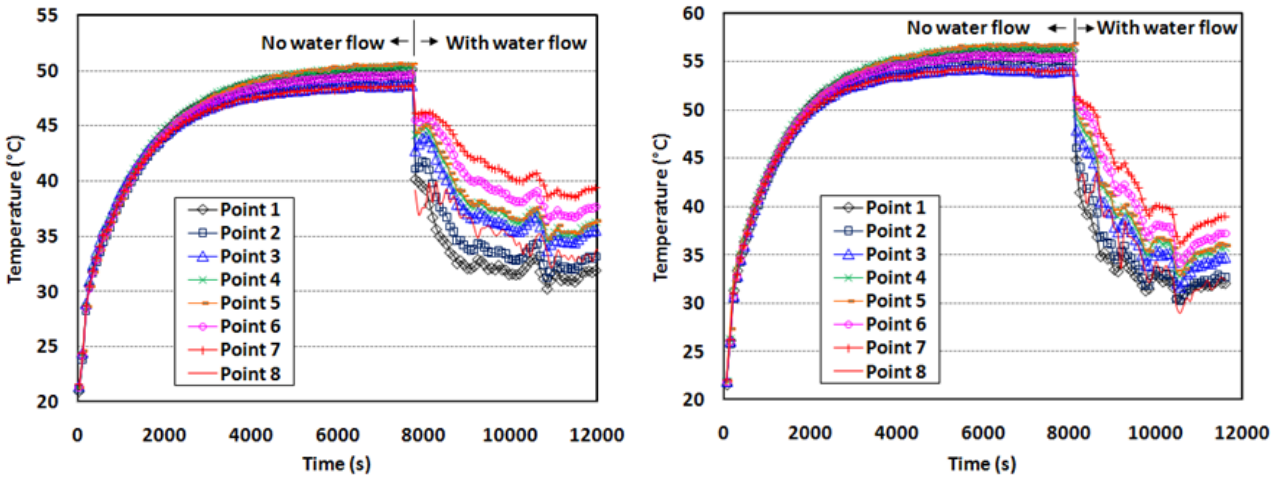

Figure 6.3.4: Temperature variation with time diagram for (a) irritation: 850 W/m^2, water flow rate: 33 ml/min, (b) irritation: 1100 W/m^2, water flow rate: 66 ml/min

accuracy due to the curvature of water tube and fluid heat transfer characteristics.

Material specification

Within each FGM layer, material is assumed to be homogeneous, and the effective thermal conductivity can be calculated based on following equation (Yin et al., 2005).

$$\overline{k} = k_B \frac{\phi\alpha\left[1+\frac{\phi\beta^2}{4}\right]+(1-\phi)}{\phi\frac{k_B}{k_A}\alpha\left[1+\frac{\phi\beta^2}{4}\right]+(1-\phi)} \tag{6.3.1}$$

where k_A, k_B is the thermal conductivity of particle phase A and matrix B, respectively, which stand for two constitution particulate materials for the FGM layer, e. g. the Al and HDPE powders. ϕ is volume fraction of particle phase A, and α, β are defined as (Yin et al., 2005)

$$\alpha = \frac{3k_A}{k_A+2k_B}, \quad \beta = \frac{k_A-k_B}{k_A+2k_B} \tag{6.3.2}$$

By using the thermal conductivity values of 238 $W/m.K$ and 0.26 $W/m.K$ for Al and HDPE, respectively, the effective thermal conductivity of HDPE/Al matrix with different volume fraction can be calculated. Table 6.1 lists the dimension and properties of each layer

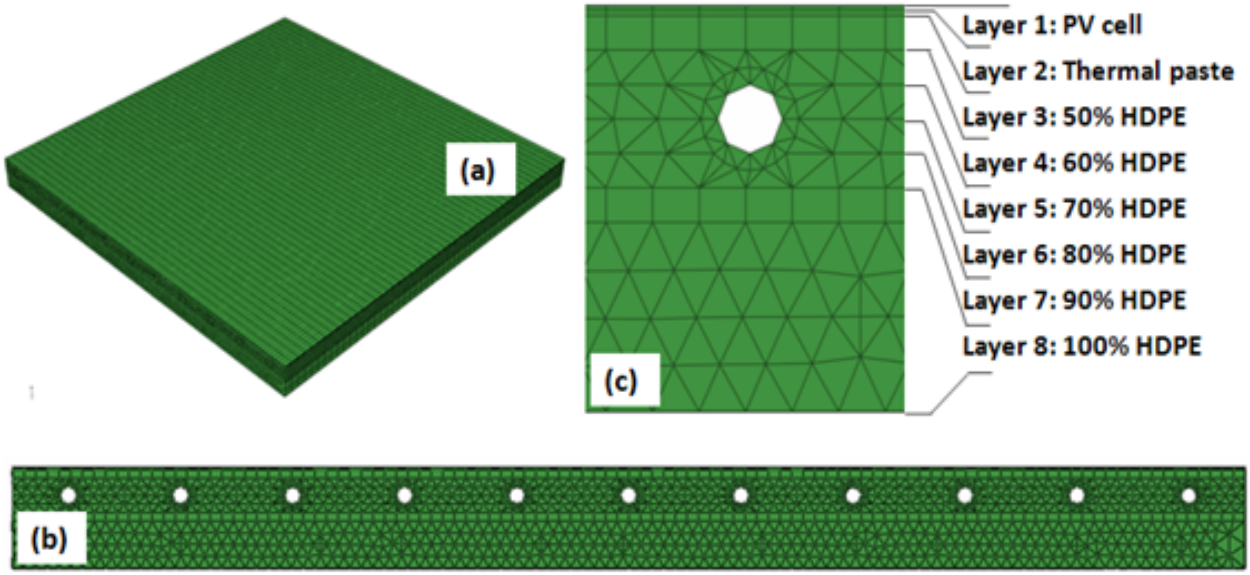

Figure 6.3.5: FEM Model and grid generation for (a) whole of solar Panel, (b) close up of the cross section, and (c) close up of a water tube

and material that are used in the finite element simulation.

Thermal energy circulation

The total input solar energy E_{in} is simulated using the numerical integration of the 25 point irradiation value shown in Figure 6.3.1. A one dimensional thermal conduction model is used to simulate the heat transfer between and within each layer. The radiation and convection heat loss can be calculated as:

$$E_{rad} = \epsilon \cdot s \cdot \left(T_{pv}^4 - T_{am}^4\right) \tag{6.3.3}$$

$$E_{con} = h_c \cdot (T_{pv} - T_{am}) \tag{6.3.4}$$

where ϵ, s, h_c, T_{pv} and T_{am} are the average surface emissivity of silicon ~ 0.6, Stefan-Boltzmann Constant ~ 5.67×10^{-8} $W/m^2.K^4$, convection coefficient of air ~ 5 $W/m^2.K$, panel surface temperature and ambient temperature, respectively (Wieder, 1982; Sopori et al., 1999). The solar room ambient temperature, $T_{am}.$, is also continuously recorded with the range from $25°C$ to $35°C$. A forced convention model is used to describe the heat transfer

Table 6.1: Thickness and properties of each material used in FEM simulation

Layer/Material	Thickness (mm)	Density g/cm^3	Specific heat J/g.K	Thermal conductivity W/m.K
1, PV cell (Si)	0.27	2.33	0.7	130
2, Silicone thermal paste	0.30	2.6	0.7	1.9
3, 50% HDPE	2	1.83	1.58	1.13
4, 60% HDPE	2	1.65	1.74	0.83
5, 70% HDPE	2	1.48	1.85	0.62
6, 80% HDPE	2	1.30	1.98	0.46
7, 90% HDPE	2	1.13	2.12	0.35
8, 100% HDPE	13	0.95	2.25	0.26
Copper tube	1	8.94	0.39	401
Water	-	1	4.18	0.58

between the water and the FGM layers. The Nusselt number is defined as (Bejan, 2004)

$$Nu = \frac{h_w D}{k} \tag{6.3.5}$$

where h_w is convection heat transfer coefficient of water , D is water tube diameter, and k is thermal conductivity of water, which is approximately 0.58 $W/m.K$. Normally, for fully developed pipe flow with uniform wall heat flux, Nusselt number is given by $Nu = 48/11 = 4.36$ (Bejan, 2004). For this model, D is the copper pipe diameter of ~ 4 mm, so the heat convection transfer coefficient of water is

$$h_w = \frac{Nu \cdot k}{D} = 632.2 \ W/m^2.K \tag{6.3.6}$$

For simplicity, we assume the water temperature increases linearly along the water flow path, which can be effectively justified by the data in Figure 6.3.3. Once we know the temperatures of inlet water and outlet water at one time, the temperature distribution of

water flow along the full path within the FGM layer can be approximated for heat transfer simulation in the FEM model.

Simulation results

Figure 6.3.6 shows the equilibrium temperature space distribution in the panel at the condition of the irradiation at 1100 W/m^2 and the water flow rate at 66 ml/min. The red color and blue color stand for high and low temperatures, respectively. Before the water flow starts, the whole panel surface is uniformly heated up, as depicted in Figure 6.3.6(a). When the water flow was introduced, the overall panel surface temperature decreased and linearly distributed from the inlet to outlet position, as shown in Figure 6.3.6(b), which is consistent with the experimental observations in Figure 6.3.3, where the temperatures of point 1~7 monotonically increase with the point number.

The temperature variation with time of the 7 points on the panel are also simulated and compared to the experimental results. As the data profiles of both experiment and simulation for the 7 points are practically the same, only the results of point 4 are shown in Figure 6.3.7. Basically, the FEM simulation results well fit to the experiments. There is a gap (8 % mismatch) between the FEM simulations and experiment data at the initial stage of the temperature increment. This can probably be related to the non-stability of the solar room conditions, such as the air circulation or solar irradiation power, which may contribute to the lower surface temperature of the solar panel compared to simulations. At the equilibrium conditions without water flow, the FEM simulations have good agreement with the experiment data with less than 2.5 % difference. At the temperature falling region after the water flow introduced, the temperature fluctuation of the experiment data is due to the variations of the water flow rate, which is difficult to control at low flow rate. Better fittings in Figure 6.3.7(b) can be achieved at high water flow rate, e.g. 66 ml/min, which normally is more stable compared to 33 ml/min.

6.3.4 Energy Efficiency Analysis

From the simulation and experimental data, it is found that FGM based water tubes can effectively reduce the panel temperature. For the case of 1100 W/m^2 irradiation with 66 ml/min water flow, the panel temperature can be reduced from 55°C to 35°C (average from 32°C to 38°C). The single crystalline Si solar cell efficiency is 13 % at room temperature and normally decreases with temperature. Based on the crystalline Si cell efficiency temperature coefficient of $-0.54\%/°C$ characterized in another work (Yang and Yin, 2011), the efficiency of the PV cell will downgrade to 10.8% at 55°C and recover to 12.3% at 35°C with the FGM cooling function. So that the PV cell performance can keep around 95% of that at room temperature even under 1100 W/m^2 irradiation. Using the 25 point irradiation value in Figure 6.3.1, the total input solar energy E_{in} on the panel can be numerically calculated to be 93.9 W and electric energy generated from PV cell is $E_{pv} = E_{in} \times 12.3\% = 11.5\,W$. In addition, the thermal energy collected by water per second is around $E_{water} = m_{water} \times C_{water} \times \Delta T_{water} = 1.1\,g \times 4.18\,W/g.°C \times 12°C = 55.2\,W$. (The outlet water temperature in around 32°C based on Figure 6.3.4(b)). Thus the overall efficiency of the panel is $\eta = (E_{water} + E_{pv})/E_{in} = (55.2 + 11.5)/93.9 = 71\%$, which are very promising results compared to those of traditional PV thermal hybrid solar panels. The energy efficiency analysis and comparisons with traditional panels are summarized in Table 6.2.

Table 6.2: Energy and efficiency summary and comparisons

Panel Type		Electric Energy (W)	Thermal Energy (W)	Efficiency
FGM based hybrid solar panel	Without water	10.1	0	10.8%
	With water	11.5	55.2	71.0%
Traditional liquid-type PV thermal hybrid solar panel (Ref.)				*53% ~ 68.2%* {Chow, 2010}

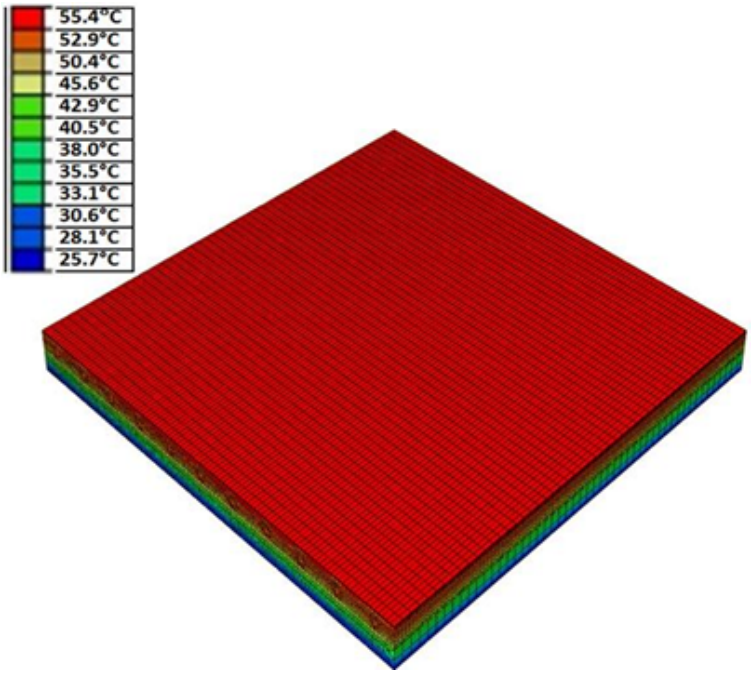

(a)

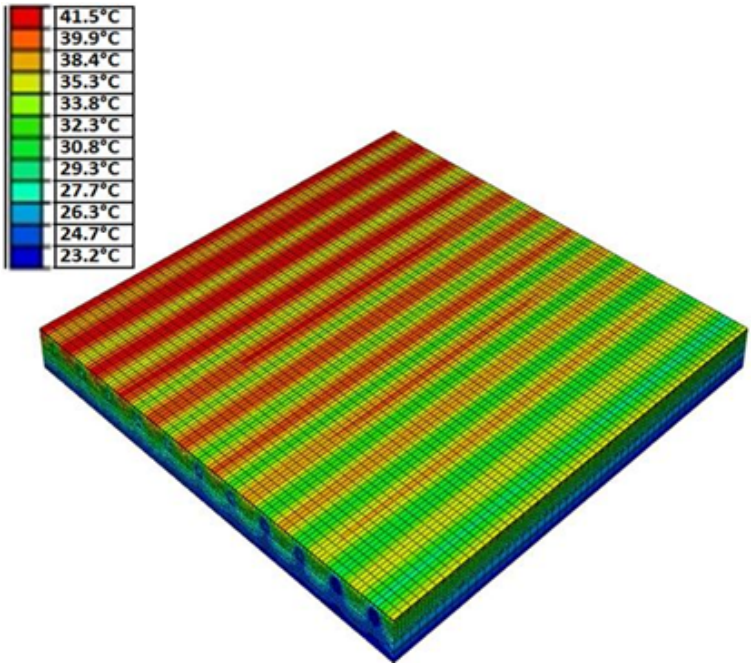

(b)

Figure 6.3.6: Temperature space distributions of the panel at (a) 1100 W/m^2 irradiation without water flow, (b) 1100 W/m^2 irradiation with water flow of 66 ml/min

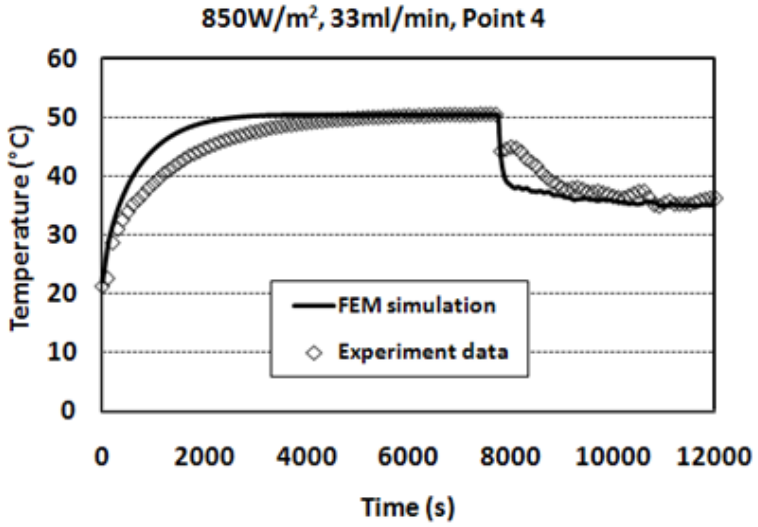

(a)

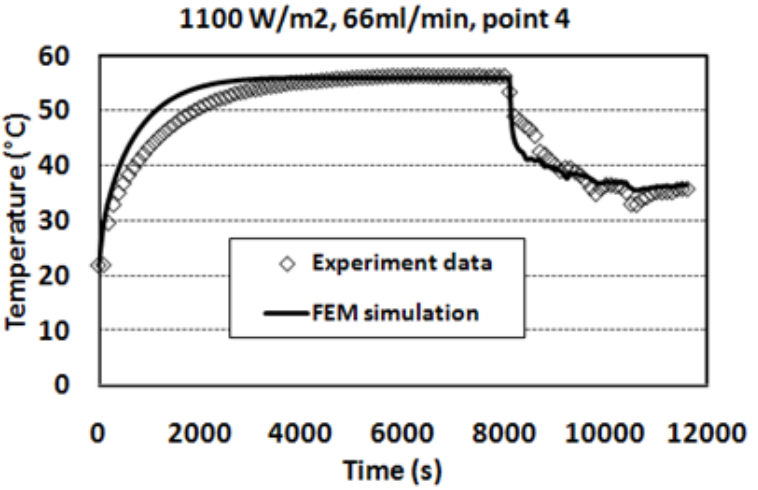

(b)

Figure 6.3.7: FEM simulation and experimental data of the temperature distribution under (a) 850 W/m^2 irradiation and 33 ml/min water flow rate (point 4), and (b) 1100 W/m^2 irradiation and 66 ml/min water flow rate (point 4)

Chapter 7

Conclusions and Future Works

7.1 Summary

This dissertation investigates the fabrication, characterization, and modeling of aluminum and high-density polyethylene functionally graded material (Al-HDPE FGM), which is integrated in our novel hybrid solar roofing panel system. The major research methods and results are summarized as follows. Firstly, a simple, economical, and scalable material manufacturing method of sedimentation was successfully employed to fabricate the deposition of AL-HDPE FGM, and the Stokes' law based modeling was developed to predict the settling motion of mixed particles of aluminum and high-density polyethylene at a small Reynolds number. Secondly, in order to improve the simulation of particle sedimentation, the Eshelby's equivalent inclusion method was initially used to derive the Stokes flow of an ellipsoidal drop moving in a viscous fluid. Then, this method was extended to the cases of two or more spherical drops to discuss the interaction between drops. Thirdly, the vibration method, which is more efficient and economical, was introduced as a suitable fabrication method for mass production of the AL-HDPE FGM. The cylindrical thin film of gradient slurry was successfully created with appropriate experimental parameters and was then sintered into solid specimens. Finally, the performance analysis of the novel hybrid solar roofing panel

was demonstrated by the experiments and finite element simulation. The electrical efficiency of photovoltaic cells was enhanced due to the integration of an aluminum and high-density polyethylene functionally graded material (Al-HDPE FGM) interlayer with water tubes cast inside.

7.2 Key Results

This dissertation has contributed to the following four main aspects related to the fabrication, characterization, and modeling of aluminum and high-density polyethylene functionally graded materials:

Fabrication of Al-HDPE FGM by the sedimentation method

The sedimentation behavior of the spherical aluminum powder and the mix of aluminum and HDPE powder settling in ethanol is investigated. When pure aluminum particles were used, they were divided into three groups with respect to the particle size. The volume fraction of each group was measured by the particle analyzer layer by layer along the thickness direction after the completion of sedimentation and air drying. Similarly, when both aluminum and HDPE particles were used, the volume fraction of aluminum was determined by the Rice density measurement. The numerical simulation based on Stokes' law was developed to predict the sedimentation behavior, which was validated by experimental results. The following conclusions can be made through the experiments and simulation:

- The present model produces very good prediction of particle size distribution in the depth direction of the deposition for pure Al-104 particles. Larger solid load and lower suspension depth (settling distance) of the suspension decrease the material gradation.
- For the case of Al-104 particle mixed with HDPE powder, the complex interaction between finer aluminum and larger HDPE particles produces an unstable sedimentation

process which is not very predictable even with the proposed modeling using a single particle settling in a fluid with a Stokes flow.

- For the case of Al-101, very good agreement between the testing and modeling results is obtained. The results indicate that the sedimentation behavior of particle under laminar flow can be predicted by the numerical model based on the Stokes' law.
- For the case of Al-111, the bi-layered microstructure of the deposition is obtained for the present solid load in suspensions. The proposed modeling may not be applicable if the whole particle system is not under the laminar flow.

Based on the modeling and testing results, the following recommendations for future manufacture of FGMs in solar roofing panels are provided:

1. To make a stable sedimentation process, aluminum particle size should be no less than the HDPE.
2. To make a rapid sedimentation process, larger aluminum particles and higher solid load should be used.
3. When the particles are too large, bi-layered microstructures are produced, which should be avoided. In the current solid load, Al-101 exhibits the best performance for FGM fabrication. However, the optimal particle size depends on the solid load.

The present numerical simulation and modeling framework provides a reliable and effective tool for future design and optimization of FGM manufacturing for the novel solar panels.

Eshelby's equivalent inclusion method for sedimentation

A new approach using the Eshelby's equivalent inclusion method was presented to study the mechanical fields of one ellipsoidal drop moving in a different viscous fluid. The exact solution of the velocity field was obtained in terms of elliptic integrals. The drag force of the drop can be derived at an given effective velocity. When the drop shape is spherical the

results of the drag force for a single sphere, such as a solid particle, a drop, or an air void moving in a fluid, are consistent with Stokes' law. The explicit solution of the velocity and pressure fields were obtained for both the interior and exterior region of the drop, which is consistent with the classic solution (Batchelor, 1967).

Furthermore, the present method can be extended to a complicated condition - the interaction of two spherical drops. A similar algorithm, the eigenstrain rate, is assumed as the polynomial form in the position coordinates, and this was introduced to solve the equation system due to pair of drops. The effect on the translational velocity of each drop produced by the change of parameter are studied and concluded as follows:

1. For the case of two identical arbitrary oriented solid spheres, the longer interval will generate less interaction, including smaller translational velocity and body rotation (no rotation for two vertically oriented drops) of the drops. Moreover, The results of translational velocity from the present method are almost as same as Batchelor's solution.

2. For the case of one solid sphere horizontally oriented with another spherical drop, the change in viscosity of the drop only slightly affected the velocity of the solid sphere.

3. For the case of one fixed-size spherical drop horizontally oriented with another varied-sized spherical drop, the expansion of the varied-sized drop was a significant effect on the velocity of fixed-size drop.

Fabrication of Al-HDPE FGM by the vibration method

The aluminum and high-density polyethylene functionally graded material (Al-HDPE FGM) has successfully been produced by vibration method. Under high-frequency vertical vibration, the particle segregates as demonstrated as reverse Brazil-nut effect (RBN), where larger and heavier aluminum particles tend to settle down to the bottom. The density measurement (Rice method) was used to determine the gradation of the volume fraction of aluminum

along the depth direction of deposition. Different textures of deposition including uniform-like, graded and bi-layered were created according to different vibration parameters. The graded deposition of Al-HDPE mixture, in which the volume fraction of aluminum gradually changes from 0 to 50%, can be stably fabricated when it is subjected to level 3 vibration (-10~8.5 g; 113.33 Hz) for 30 seconds. This quick and economical method will be extend to manufacture the original size ($2^{'} \times 2^{'}$) of Al-HDPE FGM interlayer for solar roofing panel system. Also, it is more suitable for mass production compared with the sedimentation method.

Performance of novel hybrid solar roofing panel

A novel solar panel integrated with photovoltaic cells and water tubes embedded in functionally graded material (FGM) was fabricated. The FGM layer can effectively transfer heat from the PV cells to water tubes and prevent heat transfer to the substrate. The hybrid solar panel exhibits promising performance with PV cells working at relatively low temperatures. Considering electricity and thermal energy collection, the overall panel efficiency is around 71%, which compares favorably with those of traditional PV thermal hybrid solar panels. A finite element model was successfully built to simulate the heat transfer characteristics in the hybrid solar panel prototype and the simulation results were consistent with the experimental data. It provides a general approach for future FGM based solar panel design and optimization.

7.3 Future Works

In the near future, the characterization of aluminum and high-density polyethylene functionally graded material (Al-HDPE FGM) will be continued. After obtaining the graded specimen, the thermal properties including the expansion coefficient, conductivity and diffusivity along the depth direction can be measured by a thermal dilatometer (Orton, Model 2010C

Dilatometer) and a NanoFlash thermal diffusivity analyzer (Netzsch, LFA 447 NanoFlash) layer by layer. Meanwhile, the concepts of Representative Volume Elements (RVE), Eshelby's equivalent inclusion method (EIM) and homogenization method can be used to inversely determine the volume fraction of aluminum (or polyethylene) according to different effective thermal properties, which are determined by a equipment.

Theoretical study of the Eshelby's equivalent inclusion method will be explored further. In the simulation of sedimentation, it can be pushed forward into more complicated cases, such as the many-drops system with different shapes or bounded boundary condition. Furthermore, the effective material properties of structural materials, such as concrete and asphalt, investigated by EIM will be an attractive challenge.

In the long-term, improving the efficiency of the solar roofing panel system will be considered. Inventing a novel, economical and sustainable manufacturing methodology for FGMs with high-quality targeted material properties will be a priority. Moreover, the application of FGM will be extended to the promising materials of structures and infrastructures for functional purposes of sound resistance, heat insulation and fireproofing.

Index

Bibliography

Agarwal, R. K., Garg, H., Jul. 1994. Study of a photovoltaic-thermal system - thermosyphonic solar water heater combined with solar cells. Energy Conversion and Management 35 (7), 605–620.

Al Harbi, Y., Eugenio, N., Al Zahrani, S., Sep. 1998. Photovoltaic-thermal solar energy experiment in saudi arabia. Renewable Energy 15 (1-4), 483–486.

Amada, S., Ichikawa, Y., Munekata, T., Nagase, Y., Shimizu, H., 1997. Fiber texture and mechanical graded structure of bamboo. Composites Part B: Engineering 28, 13–20.

Amada, S., Munekata, T., Nagase, Y., Ichikawa, Y., Kirigai, A., Zhifei, Y., May 1996. The mechanical structures of bamboos in viewpoint of functionally gradient and composite materials. Journal of Composite Materials 30, 800–819.

Amada, S., Untao, S., 2001. Fracture properties of bamboo. Composites Part B: Engineering 32, 451–459.

Avila, K., Moxey, D., de Lozar, A., Avila, M., Barkley, D., Hof, B., Jul. 2011. The onset of turbulence in pipe flow. Science 333, 192–196.

Batchelor, G. K., 1967. An introduction to fluid dynamics. Cambridge University, Cambridge.

Batchelor, G. K., 1972. Sedimentation in a dilute dispersion of spheres. Journal of Fluid Mechanics 52 (02), 245–268.

Becker, B. S., Bolton, J. D., Dec. 1997. Corrosion behaviour and mechanical properties of functionally gradient materials developed for possible hard-tissue applications. Journal of Materials Science-Materials in Medicine 8, 793–797.

Bejan, A., 2004. Convection heat transfer. Wiley.

Bergene, T., Lovvik, O. M., Dec. 1995. Model calculations on a flat-plate solar heat collector with integrated solar cells. Solar Energy 55 (6), 453–462.

Bertolino, N., Monagheddu, M., Tacca, A., Giuliani, P., Zanotti, C., Maglia, F., Tamburini, U. A., 2003. Self-propagating high-temperature synthesis of functionally graded materials as thermal protection systems for high-temperature applications. Journal of Materials Research 18, 448–455.

Bever, M. B., Duwez, P. E., 1972. Gradients in composite materials. Materials Science and Engineering 10, 1–8.

Bhargava, A. K., Garg, H., Agarwal, R. K., 1991. Study of a hybrid solar system-solar air heater combined with solar cells. Energy Conversion and Management 31 (5), 471–479.

Borcea, L., Dec. 2001. On the magneto-elastic properties of elastomer-ferromagnet composites. Journal of the Mechanics and Physics of Solids 49 (12), 2877–2919.

Braunstein, A., Kornfeld, A., 1986. On the development of the solar photovoltaic and thermal (PVT) collector. IEEE Transactions on Energy Conversion EC-1 (4), 31–33.

Brovold, T., Buttlar, W., 2001. Compact hollow cylinder tensile tester.

Caron, P., Faucompre, B., Membrey, F., Foissy, A., 1996. A new white light photosedimentometer for solid-liquid dispersion study: device description, stability and settling behaviour. Powder Technology 89, 91–100.

Chen, C., Cheng, C., 1996. Effective elastic moduli of misoriented short-fiber composites. International Journal of Solids and Structures 33, 2519–2539.

Chen, H.-S., Acrivos, A., 1978. The solution of the equations of linear elasticity for an infinite region containing two spherical inclusions. International Journal of Solids and Structures 14 (5), 331–348.

Chow, T., Feb. 2010. A review on photovoltaic/thermal hybrid solar technology. Applied Energy 87 (2), 365–379.

Chung, K. F., Yu, W. K., 2002. Mechanical properties of structural bamboo for bamboo scaffoldings. Engineering Structures 24, 429–442.

Cirakoglu, M., Bhaduri, S., Bhaduri, S. B., 2002. Processing and characterization of ti-b-based functionally graded materials produced by microwave-activated combustion synthesis. Journal of Materials Research 17, 2823–2830.

Cox III, C., Raghuraman, P., 1985. Design considerations for flat-plate-photovoltaic/thermal collectors. Solar Energy 35 (3), 227–241.

Crawford, R., Treloar, G., Fuller, R., Bazilian, M., Dec. 2006. Life-cycle energy analysis of building integrated photovoltaic systems (BiPVs) with heat recovery unit. Renewable and Sustainable Energy Reviews 10 (6), 559–575.

Dhont, J. K. G., May 1996. An Introduction to Dynamics of Colloids. Elsevier.

D&R International, 2011. 2011 Buildings Energy Data Book.

Dunn, M. L., Taya, M., 1993. Micromechanics predictions of the effective electroelastic moduli of piezoelectric composites. International Journal of Solids and Structures 30, 161–175.

Eshelby, J., 1957. The determination of the elastic field of an ellipsoidal inclusion, and related problems. Proceedings of the Royal Society of London. Series A, Mathematical and Physical Sciences 241, 376–396.

Eshelby, J. D., 1959. The elastic field outside an ellipsoidal inclusion. Proceedings of the Royal Society of London. Series A, Mathematical and Physical Sciences 252, 561–569.

Fiscina, J., Ilic, D. J., Mucklich, F., Dec. 2004. Applying the brazil-nut approach to manufacture w-cu-graded materials. Granular Matter 6, 207–213.

Fiscina, J., Ohligschlager, M., Mucklich, F., Oct. 2003. W-cu graded alloys produced by size segregation of agglomerates induced by vertical vibration at high frequencies. Journal of Materials Science Letters 22, 1455–1457.

Flander, K. D., Rovers, R., 2009. One laminated bamboo-frame house per hectare per year. Construction and Building Materials 23, 210–218.

Florschuetz, L. W., May 1975. On heat rejection from terrestrial solar cell arrays with sunlight concentration. In: 11th Photovoltaic Specialists Conference. Vol. 1. pp. 318–326.

Florschuetz, L. W., 1979. Extension of the hottel-whillier model to the analysis of combined photovoltaic/thermal flat plate collectors. Solar Energy 22, 361–366.

Fujisawa, T., Tani, T., Oct. 1997. Annual exergy evaluation on photovoltaic-thermal hybrid collector. Solar Energy Materials and Solar Cells 47 (1-4), 135–148.

Garcia, J. J., Rangel, C., Ghavami, K., 2012. Experiments with rings to determine the anisotropic elastic constants of bamboo. Construction and Building Materials 31, 52–57.

Garg, H., Adhikari, R., Jul. 1997. Conventional hybrid photovoltaic/thermal (PV/T) air heating collectors: steady-state simulation. Renewable Energy 11 (3), 363–385.

Garg, H. P., Adhikari, R. S., 1998. Transient simulation of conventional hybrid photovoltaic/thermal (PV/T) air heating collectors. International Journal of Energy Research 22 (6), 547–562.

Garg, H. P., Adhikari, R. S., 1999. Performance analysis of a hybrid photovoltaic/thermal (PV/T) collector with integrated CPC troughs. International Journal of Energy Research 23 (15), 1295–1304.

George, E., Richard, A., Ranjan, R., 2000. Special Functions. Cambridge University Press, England.

Ghavami, K., 1988. Application of bamboo as a low-cost construction material. pp. 270–279.

Ghavami, K., 2009. Non-conventional materials and technologies: Application and future tendencies.

Goldman, A., Cox, R., Brenner, H., Dec. 1966. The slow motion of two identical arbitrarily oriented spheres through a viscous fluid. Chemical Engineering Science 21 (12), 1151–1170.

Hatta, H., Taya, M., 1986. Equivalent inclusion method for steady state heat conduction in composites. International Journal of Engineering Science 24, 1159–1172.

He, Y.-R., Subramanian, V., Lannutti, J. J., 1997. Phase instability in ZrO2-NiAl functionally graded materials. Journal of Materials Research 12, 2589–2593.

Hendrie, S. D., 1979. Evaluation of combined photovoltaic/thermal collectors. In: Sun II. Vol. 1. pp. 1865–1869.

Hong, D. C., Quinn, P. V., Luding, S., Apr. 2001. Reverse brazil nut problem: Competition between percolation and condensation. Physical Review Letters 86 (15), 3423–3426.

Hu, W. Y., Guan, H. R., Sun, X. F., Li, S. Z., Fukumoto, M., Okane, I., Aug. 1998. Electrical and thermal conductivities of nickel-zirconia cermets. Journal of the American Ceramic Society 81, 2209–2212.

Huang, J. H., 1996. Equivalent inclusion method for the work-hardening behavior of piezoelectric composites. International Journal of Solids and Structures 33, 1439–1451.

Ilic, D. J., Fiscina, J., Oliver, C. G., Ilic, N., Mucklich, F., Jul. 2007. Self formed cu-w functionally graded material produced via powder segregation. Advanced Engineering Materials 9, 542–546.

Jeffery, G. B., Aug. 1912. On a form of the solution of laplace's equation suitable for problems relating to two spheres. Proceedings of the Royal Society of London. Series A, Containing Papers of a Mathematical and Physical Character 87 (593), 109–120.

Jeffrey, D. J., Nov. 1973. Conduction through a random suspension of spheres. Proceedings of the Royal Society of London. A. Mathematical and Physical Sciences 335 (1602), 355–367.

Ju, J. W., Chen, T. M., Mar. 1994a. Micromechanics and effective moduli of elastic composites containing randomly dispersed ellipsoidal inhomogeneities. Acta Mechanica 103 (1-4), 103–121.

Ju, J. W., Sun, L. Z., 1999. A novel formulation for the exterior-point eshelby's tensor of an ellipsoidal inclusion. Journal of Applied Mechanics 66 (2), 570–574.

Ju, P. J. W., Chen, T. M., Mar. 1994b. Effective elastic moduli of two-phase composites containing randomly dispersed spherical inhomogeneities. Acta Mechanica 103 (1-4), 123–144.

Jullien, R., Meakin, P., Mar. 1990. A mechanism for particle size segregation in three dimensions. Nature 344 (6265), 425–427.

Kaplar, R. J., Kwon, D., Ringel, S. A., Allerman, A. A., Kurtz, S. R., Jones, E. D., Sieg, R. M., 2000. Deep levels in p- and n-type InGaAsN for high-efficiency multi-junction III–V solar cells. Solar Energy Materials and Solar Cells 69 (1), 85–91.

Kern, E. C., Russell, M. C., 1978. Combined photovoltaic and thermal hybrid collector systems. In: 13th Photovoltaic Specialists Conference. Vol. 1. pp. 1153–1157.

Khor, K., Dong, Z., Gu, Y., Mar. 1999. Plasma sprayed functionally graded thermal barrier coatings. Materials Letters 38, 437–444.

Kieback, B., Neubrand, A., Riedel, H., Dec. 2003. Processing techniques for functionally graded materials. Materials Science and Engineering: A 362 (1-2), 81–106.

Kim, S., Karrila, S. J., 1991. Microhydrodynamics: Principle and Selected Applications. Butterworth-Heinemann, Stoneham.

Klingenberg, D. J., Zukoski, C. F., Jan. 1990. Studies on the steady-shear behavior of electrorheological suspensions. Langmuir 6 (1), 15–24.

Knight, J. B., Jaeger, H. M., Nagel, S. R., Jun. 1993. Vibration-induced size separation in granular media: The convection connection. Physical Review Letters 70 (24), 3728–3731.

Koizumi, M., Niino, M., 1995. Overview of FGM research in japan. MRS Bulletin 20, 19–21.

Kraemer, D., Hu, L., Muto, A., Chen, X., Chen, G., Chiesa, M., Jun. 2008. Photovoltaic-thermoelectric hybrid systems: A general optimization methodology. Applied Physics Letters 92 (24), 243503–1–3.

Kroner, E., 1990. Modified green functions in the theory of heterogeneous and/or anisotropic linearly elastic media. In: Micromechanics and Inhomogeneity. pp. 197–211.

Krstic, V. D., 1983. On the fracture of brittle-matrix ductile-particle composites. Philosophical Magazine A-Physics of Condensed Matter Structure Defects and Mechanical Properties 48, 695–708.

Lalovic, B., Kiss, Z., Weakliem, H., Dec. 1986. A hybrid amorphous silicon photovoltaic and thermal solar collector. Solar Cells 19 (2), 131–138.

Lamb, H. S., 1975. Hydrodynamics. Cambridge University, Cambridge.

Lee, C.-H., Chung, M.-J., Lin, C.-H., Yang, T.-H., 2012. Effects of layered structure on the physical and mechanical properties of laminated moso bamboo (phyllosachys edulis) flooring. Construction and Building Materials 28, 31–35.

Lee, P.-H., Liu, Y. J., Yin, H. M., 2013. Simulation of many spherical particles moving in a visocus fluid using the equivalent inclusion method. Physics of Fluids(To be Submitted).

Lee, P.-H., Yin, H. M., 2013. Interaction between a pair of distinct drops moving in a viscous fluid. Physical Review E(To be Submitted).

Levy, R., 2007. Solar energy conversion can be small-scale and low-tech. Physics Today 60 (10), 12–14.

Li, H., Shen, S., 2011. The mechanical properties of bamboo and vascular bundles. Journal of Materials Research 26, 2749–2756.

Liese, W., 1995. Anatomy and utilization of bamboos. European Bamboo Society Journal May, 5–12.

Lin, C. Y., Bathias, C., McShane, H. B., Rawlings, R. D., 1999. Production of silicon carbide al 2124 alloy functionally graded materials by mechanical powder metallurgy technique. Powder Metallurgy 42, 29–33.

Lo, T. Y., Cui, H. Z., Leung, H. C., 2004. The effect of fiber density on strength capacity of bamboo. Materials Letters 58, 2595–2598.

Lo, T. Y., Cui, H. Z., Tang, P. W. C., Leung, H. C., 2008. Strength analysis of bamboo by microscopic investigation of bamboo fibre. Construction and Building Materials 22, 1532–1535.

Mahdavi, M., Clouston, P. L., Arwade, S. R., 2012. A low-technology approach toward fabrication of laminated bamboo lumber. Construction and Building Materials 29, 257–262.

Mena, J., Vera, S., Correal, J. F., Lopez, M., 2012. Assessment of fire reaction and fire resistance of guadua angustifolia kunth bamboo. Construction and Building Materials 27, 60–65.

Meyer, C., 2009. The greening of the concrete industry. Cement and Concrete Composites 31, 601–605.

Mirza, S., Richardson, J. F., 1979. Sedimentation of suspensions of particles of two or more sizes. Chemical Engineering Science 34, 447–454.

Miyamoto, H., 1955. On the problem of elasticity theory for an infinite region containing two spherical cavities. In: Proceedings of the 5th Japan National Congress for Applied Mechanic. p. 125.

Miyamoto, H., Jun. 1958. On the problem of the theory of elasticity for a region containing more than two spherical cavities. Bulletin of JSME 1 (2), 103–108.

Miyamoto, Y., Kaysser, W., Rabin, B., Kawasaki, A., Ford, R., 1999. Functionally graded materials: design, processing and applications. Kluwer Academic Publishers.

Mobius, M. E., Lauderdale, B. E., Nagel, S. R., Jaeger, H. M., Nov. 2001. Brazil-nut effect: Size separation of granular particles. Nature 414 (6861), 270.

Mortensen, A., Suresh, S., 1995. Functionally graded metals and metal-ceramic composites: Part 1 processing. International Materials Reviews 40, 239–265.

Moschovidis, Z. A., Mura, T., 1975. Two-ellipsoidal inhomogeneities by the equivalent inclusion method. Journal of Applied Mechanics 42 (4), 847–852.

Moussa, C., Bartier, O., Mauvoisin, G., Pilvin, P., Delattre, G., 2012. Characterization of homogenous and plastically graded materials with spherical indentation and inverse analysis. Journal of Materials Research 27, 20–27.

Moya, J. S., Sanchezherencia, A. J., Requena, J., Moreno, R., Sep. 1992. Functionally gradient ceramics by sequential slip casting. Materials Letters 14, 333–335.

Mura, T., 1987. Micromechanics of Defects in Solids. Kluwer Academic Publishers, Dordrecht.

Nemat-Nasser, S., Hori, M., 1999. Micromechanics: Overall Properties of Heterogeneous Materials. Elsevier.

Neubrand, A., 2001. Functionally graded materials. In: Editors-in Chief:, K. H. J. B., Robert, W. C., Merton, C. F., Bernard, I., Edward, J. K., Subhash, M., Patrick, V. (Eds.), Encyclopedia of Materials: Science and Technology (Second Edition). Elsevier, Oxford, pp. 3407–3413.

Neubrand, A., Kieback, B., Riedel, H., Dec. 2003. Processing techniques for functionally graded materials. Materials Science and Engineering A - Structural Materials Properties Microstructure and Processing 362, 81–105.

Neubrand, A., Rodel, J., May 1997. Gradient materials: An overview of a novel concept. Zeitschrift Fur Metallkunde 88, 358–371.

Niino, M., Kumakawa, A., Watanabe, R., Doi, Y., 1986. Fabrication of a high pressure thrust chamber by the CIP forming method. Metal powder report 41, 663, 9.

Nishida, N., Yutani, C., Ishibashi-Ueda, H., Tsukamoto, Y., Ikeda, Y., Nakamura, Y., Nov. 2000. Histopathological characterization of aortic intimal sarcoma with multiple tumor emboli. Pathology international 50 (11), 923–927.

Nogata, F., Takahashi, H., 1995. Intelligent functionally graded material: Bamboo. Composites Engineering 5, 743–751.

Nozik, A. J., 2001. Spectroscopy and hot electron relaxation dynamics in semiconductor quantum wells and quantum dots. Annual Review of Physical Chemistry 52 (1), 193–231.

Odeh, S., Behnia, M., 2009. Improving photovoltaic module efficiency using water cooling. Heat Transfer Engineering 30 (6), 499–505.

Pacheco-Torgal, F., Jalali, S., 2011. Cementitious building materials reinforced with vegetable fibres: A review. Construction and Building Materials 25, 575–581.

Panganayi, C., Ogata, H., Hattori, K., Anwar, A. M., 2010. Effectiveness of ECC in curtailing re-emergence of weeds on an earth embankment surface. Construction and Building Materials 24, 545–551.

Plantard, G., Saadaoui, H., Snabre, P., Pouligny, B., Jul. 2006. Surface-roughness-driven segregation in a granular slurry under shear. EPL (Europhysics Letters) 75 (2), 335.

Pompe, W., Worch, H., Epple, M., Friess, W., Gelinsky, M., Greil, P., Hempel, U., Scharnweber, D., Schulte, K., Dec. 2003. Functionally graded materials for biomedical applications. Materials Science and Engineering a-Structural Materials Properties Microstructure and Processing 362, 40–60.

Prakash, J., Nov. 1994. Transient analysis of a photovoltaic-thermal solar collector for cogeneration of electricity and hot air/water. Energy Conversion and Management 35 (11), 967–972.

Raghuraman, P., Nov. 1981. Analytical predictions of liquid and air Photovoltaic/Thermal, flat-plate collector performance. Journal of Solar Energy Engineering 103 (4), 291–298.

Rockendorf, G., Sillmann, R., Podlowski, L., Litzenburger, B., 1999. PV-hybrid and thermoelectric collectors. Solar Energy 67 (4-6), 227–237.

Rosato, A., Strandburg, K. J., Prinz, F., Swendsen, R. H., Mar. 1987. Why the brazil nuts are on top: Size segregation of particulate matter by shaking. Physical Review Letters 58 (10), 1038–1040.

Ross, D., Jan. 1968. The potential due to two point charges each at the centre of a spherical cavity and embedded in a dielectric medium. Australian Journal of Physics 21 (6), 817–822.

Ross, R. T., 1982. Efficiency of hot-carrier solar energy converters. Journal of Applied Physics 53 (5), 3813–3818.

Ruys, A. J., Kerdic, J. A., Sorrell, C. C., Aug. 1996. Thixotropic casting of ceramic-metal functionally gradient materials. Journal of Materials Science 31, 4347–4355.

Sakata, S., Ashida, F., Kojima, T., 2010. Stochastic homogenization analysis for thermal expansion coefficients of fiber reinforced composites using the equivalent inclusion method with perturbation-based approach. Computers & Structures 88, 458–466.

SanchezHerencia, A. J., Morinaga, K., Moya, J. S., 1997. Al2O3/Y-TZP continuous functionally graded ceramics by filtration-sedimentation. Journal of the European Ceramic Society 17, 1551–1554.

Schaller, R. D., Klimov, V. I., May 2004. High efficiency carrier multiplication in PbSe nanocrystals: implications for solar energy conversion. Physical review letters 92 (18), 186601–1–4.

Shabestari, S. G., Gruzleski, J. E., Apr. 1995. Gravity segregation of complex intermetallic compounds in liquid aluminum-silicon alloys. Metallurgical and Materials Transactions A-Physical Metallurgy and Materials Science 26, 999–1006.

Shao, Z.-P., Fang, C.-H., Huang, S.-X., Tian, G.-L., 2010. Tensile properties of moso bamboo (phyllostachys pubescens) and its components with respect to its fiber-reinforced composite structure. Wood Science and Technology 44, 655–666.

Shelley, J. F., Yu, Y.-Y., Mar. 1966. The effect of two rigid spherical inclusions on the stresses in an infinite elastic solid. Journal of Applied Mechanics 33 (1), 68–74.

Shen, M., Bever, M. B., 1972. Gradients in polymeric materials. Journal of Materials Science 7, 741–746, 7.

Shinbrot, T., Muzzio, F. J., Nov. 1998. Reverse buoyancy in shaken granular beds. Physical Review Letters 81 (20), 4365–4368.

Shockley, W., Queisser, H. J., 1961. Detailed balance limit of efficiency of p-n junction solar cells. Journal of Applied Physics 32 (3), 510–519.

Silva, E. C. N., Walters, M. C., Paulino, G. H., Nov. 2006. Modeling bamboo as a functionally graded material: lessons for the analysis of affordable materials. Journal of Materials Science 41, 6991–7004.

Simonet, J., Kapelski, G., Bouvard, D., 2007. A sedimentation process for the fabrication of solid oxide fuel cell cathodes with graded composition. Journal of the European Ceramic Society 27, 3113–3116.

Skoplaki, E., Palyvos, J., May 2009a. On the temperature dependence of photovoltaic module electrical performance: A review of efficiency/power correlations. Solar Energy 83 (5), 614–624.

Skoplaki, E., Palyvos, J., Jan. 2009b. Operating temperature of photovoltaic modules: A survey of pertinent correlations. Renewable Energy 34 (1), 23–29.

Sopian, K., Liu, H., Kakac, S., Veziroglu, T., Mar. 2000. Performance of a double pass photovoltaic thermal solar collector suitable for solar drying systems. Energy Conversion and Management 41 (4), 353–365.

Sopian, K., Yigit, K., Liu, H., Kakac, S., Veziroglu, T., Nov. 1996. Performance analysis of photovoltaic thermal air heaters. Energy Conversion and Management 37 (11), 1657–1670.

Sopori, B., Chen, W., Madjdpour, J., Ravindra, N. M., 1999. Calculation of emissivity of si wafers. Journal of Electronic Materials 28 (12), 1385–1389.

Sternberg, E., Sadowsky, M., 1952. On the axisymmetric problem of the theory of elasticity for an infinite region containing two spherical cavities. Journal of Applied Mechanics (19), 19–27.

Stimson, M., Jeffery, G. B., May 1926. The motion of two spheres in a viscous fluid. Proceedings of the Royal Society of London. Series A 111 (757), 110–116.

Streletskii, A. N., Kolbanev, I. V., Permenov, D. G., Povstugar, I. V., Borunova, A. B., Dolgoborodov, A. Y., Makhov, M. N., Butyagin, P. Y., Sep. 2008. The reactivity of al-based "mechanochemical" nanocomposites. Reviews on Advanced Materials Science 18, 353–359.

Suresh, S., Mortensen, A., 1998. Fundamentals of functionally graded materials. IOM Communications Ltd, London.

Takei, T., Hatta, H., Taya, M., 1991a. Thermal expansion behavior of particulate-filled composites i: Single reinforcing phase. Materials Science and Engineering: A 131, 133–143.

Takei, T., Hatta, H., Taya, M., 1991b. Thermal expansion behavior of particulate-filled composites II: multi-reinforcing phases (hybrid composites). Materials Science and Engineering: A 131, 145–152.

Tampieri, A., Celotti, G., Sprio, S., Delcogliano, A., Franzese, S., Jun. 2001. Porosity-graded hydroxyapatite ceramics to replace natural bone. Biomaterials 22, 1365–1370.

Tan, T., Rahbar, N., Allameh, S. M., Kwofie, S., Dissmore, D., Ghavami, K., Soboyejo, W. O., 2011. Mechanical properties of functionally graded hierarchical bamboo structures. Acta Biomaterialia 7, 3796–3803.

Torres, L. A., Ghavami, K., Garcia, J. J., 2007. A transversely isotropic law for the determination of the circumferential young's modulus of bamboo with diametric compression tests. Latin American applied research 37, 255–260.

Tory, E. M., Hughes, R. J., Bargiel, M., 1995. Validity of measures of sedimentation velocity. Powder Technology 84, 259–267.

Trupke, T., Green, M. A., Wurfel, P., Aug. 2002. Improving solar cell efficiencies by down-conversion of high-energy photons. Journal of Applied Physics 92 (3), 1668–1674.

TSUCHIDA, E., NAKAHARA, I., KODAMA, M., Sep. 1976. On the asymmetric problem of elasticity theory for an infinite elastic solid containing some spherical cavities : 1st report-an infinite solid containing two spherical cavities. Bulletin of JSME 19 (135), 993–1000.

Tutuncu, N., 2007. Stresses in thick-walled FGM cylinders with exponentially-varying properties. Engineering Structures 29, 2032–2035.

Tutuncu, N., Ozturk, M., 2001. Exact solutions for stresses in functionally graded pressure vessels. Composites Part B: Engineering 32, 683–686.

U.S. Department of Agriculture Forest Service, 1999. Wood handbook: wood as an engineering material. Madison, Wisconsin.

van der Lugt, P., van den Dobbelsteen, A. A. J. F., Janssen, J. J. A., 2006. An environmental, economic and practical assessment of bamboo as a building material for supporting structures. Construction and Building Materials 20, 648–656.

Vincenzi, D., Busato, A., Stefancich, M., Martinelli, G., 2009. Concentrating PV system based on spectral separation of solar radiation. physica status solidi (a) 206 (2), 375–378.

Vorobiev, Y., Gonzalez-Hernandez, J., Vorobiev, P., Bulat, L., Feb. 2006. Thermal-photovoltaic solar hybrid system for efficient solar energy conversion. Solar Energy 80 (2), 170–176.

Vries, D. W. D., 1998. Design of a photovoltaic/thermal combi-panel. Dr., Technische Universiteit Eindhoven (The Netherlands), Netherlands.

Wang, Q., Wang, Q., Wan, C., 2012. Preparation and evaluation of a biomimetic scaffold with porosity gradients in vitro. Anais da Academia Brasileira de Ciencias 84, 9–16.

Watari, F., Yokoyama, A., Saso, F., Uo, M., Kawasaki, T., 1995. Functionally gradient dental implant composed of titanium and hydroxyapatite. Polytechniques et Universitaires Romandes, Lausanne, pp. 703–708.

Watari, F., Yokoyama, A., Saso, F., Uo, M., Kawasaki, T., 1997. Fabrication and properties of functionally graded dental implant. Composites Part B: Engineering 28, 5–11.

Wieder, S., Mar. 1982. An Introduction to Solarenergy for Scientists and Engineers. John Wiley & Sons Canada, Limited.

Wolf, M., 1976. Performance analyses of combined heating and photovoltaic power systems for residences. Energy Conversion 16 (1-2), 79–90.

Xiang, H., Shi, Z., Zhang, T., 2006. Elastic analyses of heterogeneous hollow cylinders. Mechanics Research Communications 33, 681–691.

Y. Takao, Y., Chou, T.-W., Taya, M., 1982. Effective longitudinal young's modulus of misoriented short fiber composites. Journal of Applied Mechanics 49, 536–540.

Yang, C.-Y., Ding, Y., York, D., Broeckx, W., 2008. Numerical simulation of sedimentation of microparticles using the discrete particle method. Particuology 6, 38–49.

Yang, D., Yin, H., 2011. Energy conversion efficiency of a novel hybrid solar system for photovoltaic, thermoelectric, and heat utilization. IEEE Transactions on Energy Conversion 26 (2), 662–670.

Yang, D. J., Yuan, Z. F., Lee, P. H., Yin, H. M., 2012. Simulation and experimental validation of heat transfer in a novel hybrid solar panel. International Journal of Heat and Mass Transfer 55, 1076–1082.

Yang, Z. M., Zhang, L. M., Shen, Q., Mar. 2001. Development of mathematical model on preparation of functionally graded material by co-sedimentation. Journal of Materials Science & Technology 17, 275–277.

Yin, H. M., 2004. Micromechanics-based magneto-elastic constitutive modeling of particulate composites. Ph.D., The University of Iowa, United States – Iowa.

Yin, H. M., 2009. Integrated functionally graded solar roofing panel for PV and heat utilization.

Yin, H. M., Buttlar, W. G., Paulino, G. H., Di Benedetto, H., Jan. 2008a. Assessment of existing micro-mechanical models for asphalt mastics considering viscoelastic effects. Road Materials and Pavement Design 9, 31–57.

Yin, H. M., Lai, B., 2012. Viscoelastic characterization of zeolite modified asphalt binder considering phase transformation and air void interaction. Road Materials and Pavements Design 13, 279–299.

Yin, H. M., Lee, P.-H., 2013. Equivalent inclusion method for the stokes flow of an ellipsoidal drop moving in a viscous fluid. Physics of Fluids(Submitted).

Yin, H. M., Li, L. M., Prieto-Munoz, P., Lackey, M., 2009. A novel hybrid solar roofing panel system for photovoltaic-thermoelectric-heat energy utilization.

Yin, H. M., Li, L. M., Prieto-Munoz, P., Lackey, M., 2012. Functionally graded solar roofing panels and systems.

Yin, H. M., Paulino, G. H., Buttlar, W. G., Sun, L. Z., Sep. 2005. Effective thermal conductivity of two-phase functionally graded particulate composites. Journal of Applied Physics 98 (6), 063704–1–9.

Yin, H. M., Paulino, G. H., Buttlar, W. G., Sun, L. Z., 2007. Micromechanics-based thermoelastic model for functionally graded particulate materials with particle interactions. Journal of the Mechanics and Physics of Solids 55, 132–160.

Yin, H. M., Paulino, G. H., Buttlar, W. G., Sun, L. Z., 2008b. Effective thermal conductivity of functionally graded particulate nanocomposites with interfacial thermal resistance. Journal of Applied Mechanics 75, 051113–1–6.

Yin, H. M., Paulino, G. H., Buttlar, W. G., Sun, L. Z., 2008c. Heat flux field for one spherical inhomogeneity embedded in a functionally graded material matrix. International journal of heat and mass transfer 51 (11-12), 3018–3024.

Yin, H. M., Sun, L. Z., Oct. 2006. Magnetoelastic modelling of composites containing randomly dispersed ferromagnetic particles. Philosophical Magazine 86 (28), 4367–4395.

Yin, H. M., Sun, L. Z., Chen, J. S., May 2006. Magneto-elastic modeling of composites containing chain-structured magnetostrictive particles. Journal of the Mechanics and Physics of Solids 54 (5), 975–1003.

Yin, H. M., Sun, L. Z., Paulino, G. H., 2004. Micromechanics-based elastic modeling for functionally graded materials with particle interactions. Acta Materialia 52, 3535–3543.

Yin, H. M., Yang, D. J., Kelly, G., Garant, J., Jan. 2013. Design and performance of a novel building integrated PV/thermal system for energy efficiency of buildings. Solar Energy 87, 184–195.

Yu, W. K., Chung, K. F., Chan, S. L., 2003. Column buckling of structural bamboo. Engineering Structures 25, 755–768.

Yu, Y., Fei, B., Zhang, B., Yu, X., 2007. Cell-wall mechanical properties of bamboo investigated by in-situ imaging nanoindentation. Wood and Fiber Science 39, 527–535.

Yu, Y., Tian, G., Wang, H., Fei, B., Wang, G., 2011. Mechanical characterization of single bamboo fibers with nanoindentation and microtensile technique. Holzforschung 65, 113–119.

Zapryanov, Z., Tabakova, S., 1998. Dynamics of Bubbles, Drops and Rigid Particles. Springer.

Zhou, Y. C., Hashida, T., Feb. 2002. Thermal fatigue failure induced by delamination in thermal barrier coating. International Journal of Fatigue 24, 407–417.

Zondag, H., May 2008. Flat-plate PV-Thermal collectors and systems: A review. Renewable and Sustainable Energy Reviews 12 (4), 891–959.

Nomenclature

ϵ	Surface emissivity of silicon
η	Viscosity of suspension
η_0	Viscosity of the pure ethanol solution
Γ_{ijk}	Modified Green's function
$\langle v_i \rangle$	Overall velocity of the drop in the direction i
ΔT	Temperature difference
Ω	A subdomain of inhomogeneity
$\overline{k}$	Effective thermal conductivity
ϕ	Volume fraction of particles
ρ	Density of the materials (ethanol, Al and HDPE)
C	Specific heat
D	An infinite domain of homogeneous fluid
E_{con}	Convection heat loss
e_{ij}	Strain rate in an infinite domain D
e^*_{ij}	Eigenstrain strain rate applied on subdomain Ω
E_{in}	Input solar energy
E_{pv}	Photovoltaic (PV) cell energy
E_{rad}	Radiation heat loss

E_{water} Thermal energy from water

$F(r)$ Cumulative particle size distribution of Al powder with size no less than r

f_i Body force applied on a subdomain Ω in the direction i

h_c Convection coefficient of air

h_{total} Height of suspension

h_w Convection coefficient of water

I_{sc} Short circuit current

k Thermal conductivity

n Number of sections in discretization

Nu Nusselt number

P Total momentum of particles

$p(\mathbf{x})$ Pressure field in an infinite homogeneous fluid D

Re Reynolds number

S Cross-section area of tube

s Stefan-Boltzmann Constant

T_{am} Ambient temperature

T_{pv} Photovoltaic (PV) cell temperature

$v_i(\mathbf{x})$ Velocity field in an infinite homogeneous fluid D

V_{oc} Open circuit voltage

Appendix A

Hollow Cylinder Test for Bamboo

Bamboo, which has become increasingly popular as a renewable structural material in past decades, is a natural functionally graded material whose elastic modulus gradually increases from the inner to the outer surfaces. A hollow cylinder test has been developed to characterize the strength and stiffness of bamboo specimens in the cross sectional plane. A hydraulic jack is used to inflate rubber hose, which is inserted into a bamboo specimen to apply an inner pressure. The strains on the inner and outer surfaces of the bamboo are measured under an increasing inner pressure until that the bamboo specimen splits. The effective elastic modulus of bamboo varies continuously in the radial direction that is tentatively approximated by a power, exponential and linear function, respectively, each of which includes two parameters to be determined experimentally. Given an inner pressure, the stress and strain distributions along the radial direction can be analytically derived for the three forms of elastic modulus distribution functions, respectively. Fitting the test data with the formulation, we can obtain the two parameters for each elastic modulus distribution function. Based on the cellular microstructure and comparison of the elastic modulus distribution, the exponential function of elastic modulus provides the most reasonable results and is thus recommended for a future standard test method, which is proposed for bamboo material characterization and quality control.

A.1 Overview

The environmental impact of civil engineering infrastructure construction has brought significant attention to the research community in the last decade (Meyer, 2009). In order to relieve this burden, researchers, engineers and the construction industry have been highly interested in non-polluting and sustainable materials for engineering applications (Ghavami, 2009). Bamboo, as a typical natural and renewable material, became increasingly popular as a structural material in past decades (van der Lugt et al., 2006; Flander and Rovers, 2009; Panganayi et al., 2010; Pacheco-Torgal and Jalali, 2011; Lee et al., 2012; Mahdavi et al., 2012). In addition to its environmental considerations, bamboo also has outstanding physical and mechanic properties, such as excellent strength, good flexibility and lightweight. The tensile strength of bamboo fiber can be comparable to that of steel (Nogata and Takahashi, 1995), and the average fracture toughness of bamboo can be higher than that of aluminum alloy (Amada and Untao, 2001). Furthermore, bamboo grows at amazing speeds; it almost grows to its full size in a few months and finishes developing within five years (Liese, 1995).

In some tropical and subtropical counties, such as China and India, bamboo has already been used as a practical and economical structural material (Amada and Untao, 2001; Ghavami, 1988). Thus, analysis for the mechanic properties of bamboo attracts great research interest (Amada et al., 1996, 1997; Chung and Yu, 2002; Yu et al., 2003; Lo et al., 2004; Silva et al., 2006; Yu et al., 2007; Lo et al., 2008; Shao et al., 2010; Li and Shen, 2011; Tan et al., 2011; Garcia et al., 2012; Mena et al., 2012). However, bamboo is a natural FGM and its properties are not as simple as other homogenous material. For example, the elastic modulus and tensile strength may significantly change in the radial direction. Generally, the mechanical properties of bamboo depend on fiber volume fraction and distribution. Because the density of fiber continuously increases from the inner to outer surfaces, the elastic modulus and tensile strength distribution will follow the similar trend (Nogata and Takahashi, 1995; Amada and Untao, 2001; Lo et al., 2008). Furthermore, the anisotropy is another significant characteristic of bamboo. The longitudinal modulus is more than ten

times the radial and circumferential modulus in some empirical studies (Torres et al., 2007; U.S. Department of Agriculture Forest Service, 1999).

To appropriately use bamboo in structures, it is crucial to quantify the mechanical properties of bamboo, including the modulus distribution and loading capacity. Due to the continuously graded properties in the radial direction and heterogeneous microstructure, it is difficult to accurately test mechanical constants point by point. We generally introduce a predefined distribution function of elastic moduli. Through the stress-strain relation at a few points, we can approximately determine the elastic modulus distribution. To simplify the analysis of the approximate elastic modulus distribution, bamboo can be assumed to be a hollow and thick-walled FGM cylinder with axisymmetry. Several research papers have provided the analytical solution for the stress and displacements distribution of this FGM cylinder under inner and outer uniform pressures based on different assumptions of elastic moduli (Tutuncu and Ozturk, 2001; Xiang et al., 2006; Tutuncu, 2007). However, experimental characterization of the FGM material properties of bamboo is still a challenging problem. A standard test method based on an analytical solution will provide a very useful approach in understanding the materials and promote their applications by establishing a uniform standard for safety. The development of the test method can be a good reference of test methods for other FGM materials or structural members.

This appendix aims to investigate the elastic modulus distribution in the radial direction of bamboo's cross section and determine the ultimate strength of a bamboo sample. A hollow cylinder test is developed to characterize the strength and stiffness of bamboo specimens. A hydraulic jack, an instrument which can inflate the diameter of rubber hose, is used to apply pressure along the inner surface of a bamboo specimen during the experiment. The hoop strains on the inner and outer surfaces of the bamboo specimen are measured by strain gauges. Assuming the elastic modulus distribution in the radial direction as a continuous function, we can determine the function by fitting the loading-deformation curves. The selection of the elastic modulus distribution function should be based on the actual mi-

crostructure and mechanical characterization. However, because bamboo's cross section is of a very heterogeneous microstructure, such as varying size and density of bamboo cellulose fibers with fuzzy boundary, it is difficult to accurately characterize the microstructural gradation. In addition, the mechanical properties of fibers also vary with its age and location. Furthermore, because the thickness of bamboo wall is relevantly small compared with the bamboo culm diameter, different functions may provide comparable results. The selection of elastic modulus distribution functions should be based on the physical observation and mathematical soundness. In this work, we investigate three forms of elastic modulus distribution functions as the power, exponential and linear functions, i.e. $E(r) = E_i (r/r_i)^n$; and $E(r) = E_i e^{\lambda \frac{r-r_i}{t}}$, respectively. Fitting the test data with the formulation, we can estimate the two parameters, namely the elastic modulus at the inner surface E_i and gradation parameter n, λ or ξ of the three distribution functions, respectively, for the elastic modulus distribution in the thickness direction. We found that the exponential function provides the most reasonable prediction considering the microstructure and experimental results. Therefore, it is recommended for the future standard test method. Notice that in the literature, the exponential distribution of bamboo mechanical properties has been used by several authors (Nogata and Takahashi, 1995; Amada and Untao, 2001; Silva et al., 2006).

A.2 Formulation

Bamboo is an anisotropic material with microfibers along the axial direction. Because the density of microfibers gradually changes in the radial direction, as shown in Figure A.2.1(a), the elastic modulus also varies in a similar fashion. This appendix is to investigate the elastic modulus distribution in the radial direction of the cross sectional plane. The in-plane Poisson's ratio generally also varies in bamboo stem. Previous studies focused on the variation in the longitudinal direction (Garcia et al., 2012). Because the variation of the in-plane Poisson's ratio in the same cross sectional plane is uncertain in a small range, commonly

a single value of the effective Poisson's ratio is used in analysis and simulation for simplicity (Silva et al., 2006; Torres et al., 2007). In this study, a plane stress problem is considered for the test configuration in Figure A.2.1(b), where no constraint in the longitudinal direction is applied and the stress associated with that direction is assumed to be zero. Furthermore, in the experimental part, uniform pressure is applied on the inner surface of bulk bamboo specimen. For simplicity, a single value of the in-plane Poisson's ratio in the cross section of bamboo specimen will be used for convenience of formulation and implementation of the test method. It is chosen as the average of in-plane Poisson's ratio in the cross section of the specimen, which can be obtained by a uniaxial compression test in the radial direction of a small bamboo specimen taken from the split piece of the bamboo. The effect of the in-plane Poisson's ratio will be discussed later. Without specific note, the Poisson's ratio of bamboo is assumed to be constant at a value of 0.22 following previous work (Garcia et al., 2012). However, the present work is applicable to the Poisson's ratio at different values. The effect of the varying Poisson's ratio in the radial direction is still open to future investigation.

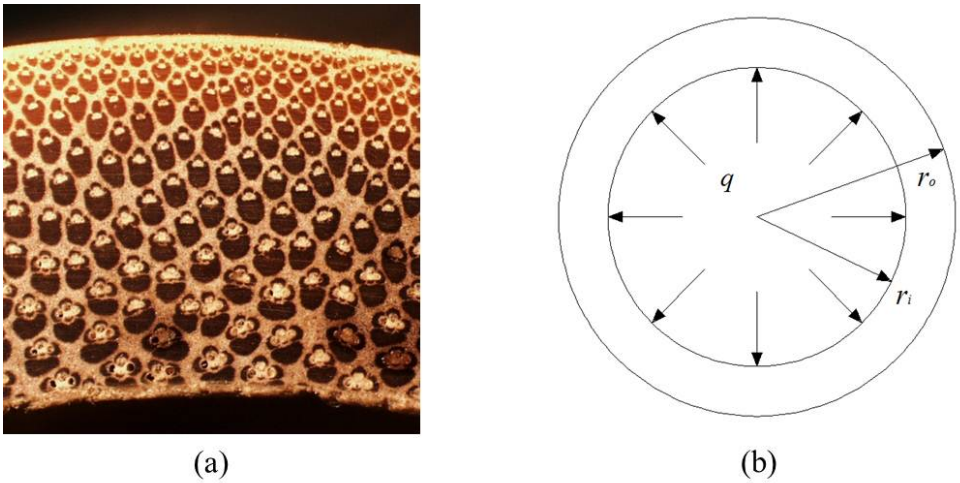

Figure A.2.1: The cross-section of a bamboo specimen: (a) partial cross section of bamboo microstructure, (b) schematic illustration of a hollow cylinder test with uniform inner pressure q applied to the inner surface

The stress distribution in a hollow thick-walled cylinder, which is predicted by three different assumptions of elastic modulus distributions, has been investigated. In all of these

three cases, E_i , r_i and $t = r_o - r_i$ denote the elastic modulus at the inner surface, inner radius and average thickness of bamboo, respectively. Besides, n, λ and ξ are the material gradation parameters to show three different types of elastic modulus distribution functions, respectively.

For an elastic material with the axisymmetry and plain strain assumptions, the strain-displacement equations are

$$\epsilon_r = \frac{du_r}{dr}, \quad \epsilon_\theta = \frac{u_r}{r}, \quad \gamma_{r\theta} = 0, \tag{A.2.1}$$

The constitutive law for plane stress problems is written as

$$\begin{aligned} \sigma_r &= C_{11}\epsilon_r + C_{12}\epsilon_\theta \\ \sigma_\theta &= C_{12}\epsilon_r + C_{11}\epsilon_\theta \end{aligned} \tag{A.2.2}$$

where C_{11} and C_{12} change with r as follows:

$$C_{11} = \frac{E\,(r)}{1-\nu^2}, \quad C_{12} = \frac{E\,(r)\,\nu}{1-\nu^2} \tag{A.2.3}$$

in which the elastic modulus changes in the radial direction and the in-plane Poisson's ratio ν is considered to be constant in the cross section.

The commonly used value of the in-plane Poisson's ratio has been found in the literature in the range of 0.12 ~ 0.43 (Silva et al., 2006; Garcia et al., 2012; Yu et al., 2011).

Without considering body forces, the equilibrium equation is

$$\frac{d\sigma_r}{dr} + \frac{\sigma_r - \sigma_\theta}{r} = 0 \tag{A.2.4}$$

Substituting Eqs.(A.2.1) and (A.2.3) into Eq.(A.2.2) and then into Eq.(A.2.4), the gov-

erning equation in terms of the radial displacement u_r and the elastic modulus $E(r)$ becomes

$$E(r)\left[ru_{r,rr}+u_{r,r}-\frac{u_r}{r}\right]+E^{'}(r)\left[ru_{r,r}+mu_r\right]=0 \tag{A.2.5}$$

in which $m=\nu$ for the plane stress condition. Notice that, if the specimen is long, and the end is constrained, the formulation can be easily transferred to the plane strain condition by redefining m with $m=\frac{\nu}{1-\nu}$ and the corresponding elastic moduli.

For the hollow cylinder with a uniform inner pressure q in Figure A.2.1(b), the boundary conditions are expressed as

$$\sigma_r\mid_{r=r_i}=-q,\quad \sigma_r\mid_{r=r_o}=0 \tag{A.2.6}$$

For different types of elastic modulus distribution of $E(r)$, the stress distribution can be significantly different. In what follows, the three different distribution functions of elastic modulus will be investigated.

A.2.1 Case I: Power Function Distribution

In this case, the elastic modulus is defined as

$$E(r)=E_i\left(\frac{r}{r_i}\right)^n \tag{A.2.7}$$

thus, the first derivative of $E(r)$ with respect to r is

$$E^{'}(r)=\frac{nE_i}{r_i}\left(\frac{r}{r_i}\right)^{n-1} \tag{A.2.8}$$

By substituting Eqs.(A.2.7) and (A.2.8) into Eq.(A.2.5) to obtain the governing equation

$$r^2u_{r,rr}+r(n+1)u_{r,r}+(nm-1)u_r=0 \tag{A.2.9}$$

The displacement for this equation can be solved as

$$u_r = I_1 r^{\frac{-(n+k)}{2}} + I_2 r^{\frac{(-n+k)}{2}} \tag{A.2.10}$$

where $k = \sqrt{n^2 + 4 - 4nm}$

Using Eqs.(A.2.1), (A.2.2a) and (A.2.10), constants I_1 and I_2 are determined with boundary condition Eq.(A.2.6) as

$$\begin{aligned} I_1 &= -\frac{2q\left(1-\nu^2\right) r_i^{\frac{n+k+2}{2}} r_o^k}{E_i(2m-n-k)\left(r_o^k - r_i^k\right)} \\ I_2 &= -\frac{2q\left(1-\nu^2\right) r_i^{\frac{n+k+2}{2}}}{E_i(2m-n+k)\left(r_o^k - r_i^k\right)} \end{aligned} \tag{A.2.11}$$

in which r_i and r_o are inner and outer radii, respectively.

Therefore, the stress components are described as

$$\begin{aligned} \sigma_r &= \frac{q r_i^{\frac{-n+k+2}{2}}}{r_o^k - r_i^k}\left[r^{\frac{n+k-2}{2}} - r_o^k r^{\frac{n-k-2}{2}}\right] \\ \sigma_\theta &= \frac{q r_i^{\frac{-n+k+2}{2}}}{r_o^k - r_i^k}\left[\frac{2-nm+km}{2m-n+k} r^{\frac{n+k-2}{2}} - \frac{2-nm-km}{2m-n-k} r_o^k r^{\frac{n-k-2}{2}}\right] \end{aligned} \tag{A.2.12}$$

A.2.2 Case II: Exponential Function Distribution

For this case, Xiang et al. reported the exact solution using the Whittaker functions (Xiang et al., 2006). The conclusions, with modification on assumption of radial elastic modulus, are listed as below. First, the elastic modulus is defined as

$$E(r) = E_i e^{\lambda \frac{r-r_i}{t}} = \left(E_i e^{-\frac{\lambda}{t} r_i}\right) e^{\frac{\lambda}{t} r} \tag{A.2.13}$$

Furthermore, the coefficients from Eq.(A.2.3) are assumed as

$$C_{11} = C_{11}^0 e^{\frac{\lambda}{t} r}, \quad C_{12} = C_{12}^0 e^{\frac{\lambda}{t} r} \tag{A.2.14}$$

where

$$C_{11}^0 = \frac{E_i}{(1-\nu^2)\, e^{\frac{\lambda}{t} r_i}}, C_{12}^0 = \frac{\nu E_i}{(1-\nu^2)\, e^{\frac{\lambda}{t} r_i}} \tag{A.2.15}$$

Substitute Eq.(A.2.13) into Eq.(A.2.5), the governing equation can be written as

$$u_{r,rr} + \left(\frac{\lambda}{t} + \frac{1}{r}\right) u_{r,r} + \left(\frac{m\lambda}{tr} - \frac{1}{r^2}\right) u_r = 0 \tag{A.2.16}$$

Thus, the general solution for this equation is obtained as

$$u_r = \frac{D_1 M_{a,1}\left(\frac{\lambda}{t} r\right) + D_2 W_{a,1}\left(\frac{\lambda}{t} r\right)}{\sqrt{r e^{\frac{\lambda}{t} r}}} \tag{A.2.17}$$

where $M_{\chi,1}\left(\frac{\lambda}{t} r\right)$ and $W_{\chi,1}\left(\frac{\lambda}{t} r\right)$ are the Whittaker functions (George et al., 2000) with a non-integer index χ ; D_1 and D_2 are constants to be determined by the boundary conditions; $a = m - \frac{1}{2}$.

Substituting Eq.(A.2.17) into Eqs.(A.2.1) and (A.2.2) give the expressions of stress distribution

$$\begin{aligned} \sigma_r &= D_1 M(r) + D_2 W(r) \\ \sigma_\theta &= D_1 \overline{M}(r) + D_2 \overline{W}(r) \end{aligned} \tag{A.2.18}$$

where

$$\begin{aligned} M(r) &= C_{11}^0 (1+m)\, r^{-\frac{3}{2}} \sqrt{e^{\frac{\lambda}{t} r}} M_{b,1}\left(\tfrac{\lambda}{t} r\right) \\ W(r) &= -C_{11}^0 r^{-\frac{3}{2}} \sqrt{e^{\frac{\lambda}{t} r}} W_{b,1}\left(\tfrac{\lambda}{t} r\right) \\ \overline{M}(r) &= C_{11}^0 (1+m)\, r^{-\frac{3}{2}} \sqrt{e^{\frac{\lambda}{t} r}} \left[m M_{b,1}\left(\tfrac{\lambda}{t} r\right) + (1-m) M_{a,1}\left(\tfrac{\lambda}{t} r\right)\right] \\ \overline{W}(r) &= -C_{11}^0 r^{-\frac{3}{2}} \sqrt{e^{\frac{\lambda}{t} r}} \left[m W_{b,1}\left(\tfrac{\lambda}{t} r\right) + (m^2-1) W_{a,1}\left(\tfrac{\lambda}{t} r\right)\right] \end{aligned} \tag{A.2.19}$$

Here $b = m + \frac{1}{2}$. Fitting with the boundary conditions in Eq.(A.2.6), D_1 and D_2 can be calculated as

$$\begin{aligned} D_1 &= \frac{qW(r_o)}{W(r_i)M[33](r_o) - W(r_o)M(r_i)} \\ D_2 &= -\frac{qM(r_o)}{W(r_i)M(r_o) - W(r_o)M(r_i)} \end{aligned} \tag{A.2.20}$$

A.2.3 Case III: Linear Function Distribution

The exact solution for linear distribution is also studied by Xiang et al. (2006) The displacement and the stress distributions are in terms of hyper-geometric functions. The major features of the procedure to obtain the solution are summarized as follows. The elastic modulus with slight modification is expressed as

$$E(r) = E_i + \xi(r - r_i) = Ar + B \tag{A.2.21}$$

Substitute Eq.(A.2.21) into Eq.(A.2.5), the ordinary differential equation of radial displacement can be written as

$$u_{r,rr} + \left(\frac{A}{Ar+B} + \frac{1}{r}\right) u_{r,r} + \left(\frac{mA}{Ar^2+Br} - \frac{1}{r^2}\right) u_r = 0 \tag{A.2.22}$$

The general solution of Eq.(A.2.22) is determined

$$u_r = C_1 F\left(\alpha, \beta; \gamma; -\frac{B}{Ar}\right) r^{\kappa} + C_2 F\left(\alpha - \gamma + 1, \beta - \gamma; 2 - \gamma; -\frac{B}{Ar}\right) r^{\beta} = C_1 F_1(r)\, r^{\kappa} + C_2 F_2(r)\, r^{\beta} \tag{A.2.23}$$

where $F_1(r)$ and $F_2(r)$ are the hyper-geometric functions (2000), C_1 and C_2 are constants to be determined by boundary conditions and

$$\begin{cases} \gamma = 1 + \sqrt{5 - 4m} \quad , \quad \kappa = -\frac{\gamma}{2} \\ \alpha = \frac{\gamma}{2} + 1 \quad , \quad \beta = \frac{\gamma}{2} - 1 \end{cases} \tag{A.2.24}$$

Substituting Eq.(A.2.23) into Eqs.(A.2.1) and (A.2.2) give the expressions of stress distribution

$$\begin{aligned} \sigma_r &= C_1 P(r) + C_2 N(r) \\ \sigma_\theta &= C_1 \overline{P}(r) + C_2 \overline{N}(r) \end{aligned} \tag{A.2.25}$$

where

$$\begin{aligned} P(r) &= C_{11}(r)\left[F_1'(r)\,r^{\kappa}+(m+\kappa)\,F_1(r)\,r^{\kappa-1}\right] \\ N(r) &= C_{11}(r)\left[F_2'(r)\,r^{\beta}+(m+\beta)\,F_2(r)\,r^{\beta-1}\right] \\ \overline{P}(r) &= C_{11}(r)\left[mF_1'(r)\,r^{\kappa}+(1+m\kappa)\,F_1(r)\,r^{\kappa-1}\right] \\ \overline{N}(r) &= C_{11}(r)\left[mF_2'(r)\,r^{\beta}+(1+m\beta)\,F_2(r)\,r^{\beta-1}\right] \end{aligned} \tag{A.2.26}$$

Fitting with boundary condition Eq.(A.2.6), C_1 and C_2 can be calculated as

$$\begin{aligned} C_1 &= \frac{qN(r_o)}{N(r_i)P(r_o)-N(r_o)P(r_i)} \\ C_2 &= -\frac{qP(r_o)}{N(r_i)P(r_o)-N(r_o)P(r_i)} \end{aligned} \tag{A.2.27}$$

A.2.4 Derivation of Two Parameters for Exponential Assumption of Elastic Modulus

In above subsections of three different cases, the radial displacement u_r is expressed in terms of two parameters for three cases of elastic modulus assumptions. Fitting the expression of displacement with the experimental data, which are inner and outer hoop strains, the two parameters can be solved by numerical method . The following is one example of the explicit derivation for the exponential assumption of the elastic modulus.

For case II, where $E(r)=E_i e^{\lambda\frac{r-r_i}{t}}$, the radial displacement could be obtained and have been shown in Eq.(A.2.17) as

$$u_r=\frac{D_1 M_{a,1}\left(\frac{\lambda}{t}r\right)+D_2 W_{a,1}\left(\frac{\lambda}{t}r\right)}{\sqrt{re^{\frac{\lambda}{t}r}}}$$

where D_1 and D_2 have been calculated in Eq.(A.2.20), $M_{\chi,1}\left(\frac{\lambda}{t}r\right)$ and $W_{\chi,1}\left(\frac{\lambda}{t}r\right)$ are the Whittaker functions and $a=m-\frac{1}{2}$.

Substituting Eq.(A.2.17) into $\epsilon_\theta=\frac{u_r}{r}$, the hoop strain can be rewritten as

$$\epsilon_\theta=\frac{D_1 M_{a,1}\left(\frac{\lambda}{t}r\right)+D_2 W_{a,1}\left(\frac{\lambda}{t}r\right)}{\sqrt{r^3e^{\frac{\lambda}{t}r}}} \tag{A.2.28}$$

From the test data, the inner and outer hoop strain with relative internal pressure is plotted in Figure A.4.1. Here, K is defined as the ratio of hoop strain increment to internal pressure increment, and K_i and K_o are the ratios for inner and outer surface, respectively. The optimal K_i and K_o are the slope of lines in Figure A.4.1 and could be solved by least square method; the definition have also mentioned as Eq.(A.4.1)

$$K_i = \frac{\Delta\epsilon_\theta \mid_{r=r_i}}{\Delta q}, \quad K_i = \frac{\Delta\epsilon_\theta \mid_{r=r_o}}{\Delta q}$$

Substituting Eq.(A.2.20) into Eq.(A.2.28) and then into Eq.(A.4.1) give another expressions of K_i and K_o

$$\begin{aligned} K_i &= \frac{G_1 M_{a,1}\left(\frac{\lambda}{t}r_i\right)+G_2 W_{a,1}\left(\frac{\lambda}{t}r_i\right)}{\sqrt{r_i^3 e^{\frac{\lambda}{t}r_i}}} \\ K_o &= \frac{G_1 M_{a,1}\left(\frac{\lambda}{t}r_o\right)+G_2 W_{a,1}\left(\frac{\lambda}{t}r_o\right)}{\sqrt{r_o^3 e^{\frac{\lambda}{t}r_o}}} \end{aligned} \tag{A.2.29}$$

where

$$\begin{aligned} G_1 &= \frac{D_1}{q} = \frac{W(r_o)}{W(r_i)M(r_o)-W(r_o)M(r_i)} = \frac{\left(1-\nu^2\right)r_i^{\frac{3}{2}}\sqrt{e^{\frac{\lambda}{t}r_i}}W_{b,1}\left(\frac{\lambda}{t}r_o\right)}{E_i(1+m)\left[W_{b,1}\left(\frac{\lambda}{t}r_i\right)\cdot M_{b,1}\left(\frac{\lambda}{t}r_o\right)-W_{b,1}\left(\frac{\lambda}{t}r_o\right)\cdot M_{b,1}\left(\frac{\lambda}{t}r_i\right)\right]} \\ G_2 &= \frac{D_2}{q} = \frac{M(r_o)}{W(r_i)M(r_o)-W(r_o)M(r_i)} = \frac{\left(1-\nu^2\right)r_i^{\frac{3}{2}}\sqrt{e^{\frac{\lambda}{t}r_i}}M_{b,1}\left(\frac{\lambda}{t}r_o\right)}{E_i\left[W_{b,1}\left(\frac{\lambda}{t}r_i\right)\cdot M_{b,1}\left(\frac{\lambda}{t}r_o\right)-W_{b,1}\left(\frac{\lambda}{t}r_o\right)\cdot M_{b,1}\left(\frac{\lambda}{t}r_i\right)\right]} \end{aligned} \tag{A.2.30}$$

Substituting Eq.(A.2.30) into Eq.(A.2.29), K_i and K_o can be rewritten as

$$\begin{aligned} K_i &= \frac{\left(1-\nu^2\right)\left[W_{b,1}\left(\frac{\lambda}{t}r_o\right)\cdot M_{a,1}\left(\frac{\lambda}{t}r_i\right)+(1+m)M_{b,1}\left(\frac{\lambda}{t}r_o\right)\cdot W_{a,1}\left(\frac{\lambda}{t}r_i\right)\right]}{E_i(1+m)\left[W_{b,1}\left(\frac{\lambda}{t}r_i\right)\cdot M_{b,1}\left(\frac{\lambda}{t}r_o\right)-W_{b,1}\left(\frac{\lambda}{t}r_o\right)\cdot M_{b,1}\left(\frac{\lambda}{t}r_i\right)\right]} \\ K_o &= \frac{\left(1-\nu^2\right)\left[W_{b,1}\left(\frac{\lambda}{t}r_o\right)\cdot M_{a,1}\left(\frac{\lambda}{t}r_o\right)+(1+m)M_{b,1}\left(\frac{\lambda}{t}r_o\right)\cdot W_{a,1}\left(\frac{\lambda}{t}r_o\right)\right]}{E_i(1+m)\left[W_{b,1}\left(\frac{\lambda}{t}r_i\right)\cdot M_{b,1}\left(\frac{\lambda}{t}r_o\right)-W_{b,1}\left(\frac{\lambda}{t}r_o\right)\cdot M_{b,1}\left(\frac{\lambda}{t}r_i\right)\right]}\left(\frac{r_i}{r_o}\right)^{\frac{3}{2}} e^{\frac{\lambda(r_i-r_o)}{2t}} \end{aligned} \tag{A.2.31}$$

Thus, E_i and λ can be calculated from Eq.(A.2.31), the nonlinear system of equations which only includes two parameters, by numerical method .

A.3 Experiment

The experiment is designed to measure the ultimate radial strength of bamboo by means of a hydraulic jack. This instrument is used to apply pressure on the inner surface of bamboo specimens. As the increment of pressure, the inner and outer hoop strains are measured by strain gauges; and the testing data is used in the following analysis of stiffness. A hollow cylinder test setup has been developed by Brovold and Buttlar for asphalt materials, which is seemly similar to the present test (Brovold and Buttlar, 2001). However, because the size and material properties of bamboo are significantly different from those of asphalt specimens that are considered with a unique elasticity, the formulation and test configuration in the present test are totally different from the previous one.

A.3.1 Apparatus

A hydraulic jack (Figure A.3.1(a)) is an instrument used to supply uniform inner pressure to bamboo while the tubing was inserted into the bamboo specimen. By up and down movement of handle, oil will be pushed away from hydraulic bag to inflatable rubber hose and pressure gauge through metal tubing, which includes holes in the region contacting with rubber hose so that the oil can move from the metal tube to the rubber hose; in consequence, rubber hose will be inflated to apply uniform pressure to inner surface of bamboo. Hose clamps on the both side right out of bamboo are used to block the oil inside the hose from leaking. The value of pressure provided by the jack is displayed by a dial pressure gauge, which is set on the instrument. In order to avoid damaging the instrument, pressure is gradually increased.

A.3.2 Specimen Preparation

To insert rubber hose into the bamboo specimens smoothly, there is a criterion for specimen dimensions. The inner diameter of the bamboo should be more than 28 mm and consistent

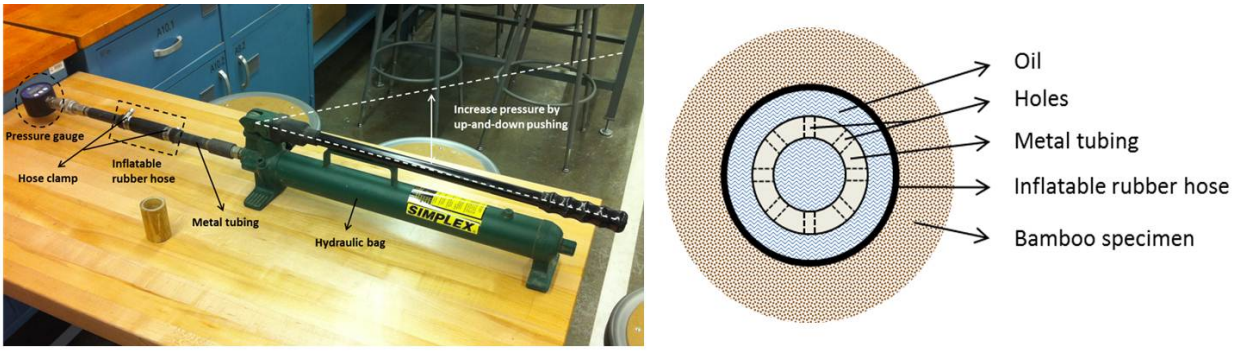

Figure A.3.1: The hollow cylinder test configuration: (a) outlook of hydraulic jack, (b) cross section of hydraulic jack

around the cylinder within 1.5 mm; also, the length of bamboo can be in a range of 40-70 mm. Notice that due to the plane stress assumption, it is important to keep the specimen no more than 70 mm to approximately keep the longitudinal stress at zero. The dimensions of two bamboo specimens are listed in Table A.1. Moreover, strain gauges are attached on the inner and outer surface of testing specimens to obtain the longitudinal and hoop strain.

Table A.1: Dimensions and ultimate radial strength of bamboo specimens

Specimen number	Inner diameter (mm)	Outer diameter (mm)	Length (mm)	Ultimate radial strength (MPa)
#1	28.8	40.2	63.1	1.793
#2	28.8	40.2	63.5	2.613

A.3.3 Test Procedure and Results

After preparation of the bamboo sample shown in Figure A.3.2, tightening up the hose clamp on the both side right out of bamboo and pressure valve on hydraulic jack are important for the accuracy of experiment. Slowly increase pressure on the instrument and record the strain at every increment of 20 psi (0.138 MPa). Due to the installation of hose clamp, the stiffness of rubber hose might slightly varies from edge to middle, which results in the non-uniform

pressure distribution on the tubing if there is no restraint of tubing expansion. However, in this experiment, the bamboo specimen is polished, so that the rubber hose may be well fitted into the bamboo specimens with minimal space; and the stiffness of bamboo is much higher than rubber hose. Considering the stiff constraint of the bamboo and low stiffness of the rubber, the stress state in the rubber can be approximated as a hydrostatic stress state under the hydraulic pressure. Even though the middle of rubber hose will first touch with inner surface of bamboo specimen, the pressure in the middle part applied on bamboo inner surface may not keep increasing significantly until the rubber hose completely fits with the bamboo inner surface. Therefore, a small initial pressure will be required to make a good contact, and then the inner hydrostatic pressure will uniformly pass to the bamboo specimen. The effect of this initial pressure will be carefully addressed in the calculation of elastic modulus and strength. The test data is the basis for estimating the unknown parameters (E_i , and n, λ or ξ) for elastic modulus distribution in the later analysis. Finally, the ultimate radial strength will be measured and recorded in Table A.1. Due to lack of perfect axisymmetry for thickness and microstructure of bamboo, the specimens are always split at the weakest point, such as the thinnest part. Thus, it is seen that there is no direct relation between the dimension and ultimate radial strength of the bamboo specimen.

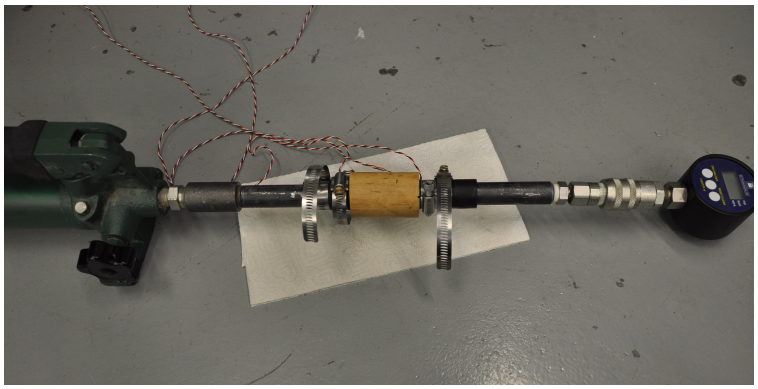

Figure A.3.2: Installation of a bamboo specimen for the hollow cylinder test

A.4 Results and Discussion

The test data of hoop strain with relative inner pressure for sample #1 and #2 are plotted in Figure A.4.1. Here,K_i and K_o are defined as the slope, and the ratio of hoop strain increment to inner pressure increment, of linear fitting line. The relation between hoop strains and constants K_i and K_o are as below

$$K_i = \frac{\Delta\epsilon_\theta \mid_{r=r_i}}{\Delta q}, \quad K_o = \frac{\Delta\epsilon_\theta \mid_{r=r_o}}{\Delta q} \tag{A.4.1}$$

The fitting lines in Figures A.4.1(a) and (b) do not pass and start from origin, which is different with normal stress-strain diagram. At the beginning of the test, the inflatable rubber hose did not touch with inner surface of bamboo specimen completely. Consequently, in the process of fully fitting hose with inner surface of specimen, the hoop strain may be still zero even there are some pressure already applied. Therefore, only the slope of the fitting line is used in the data analysis for elastic modulus distribution.

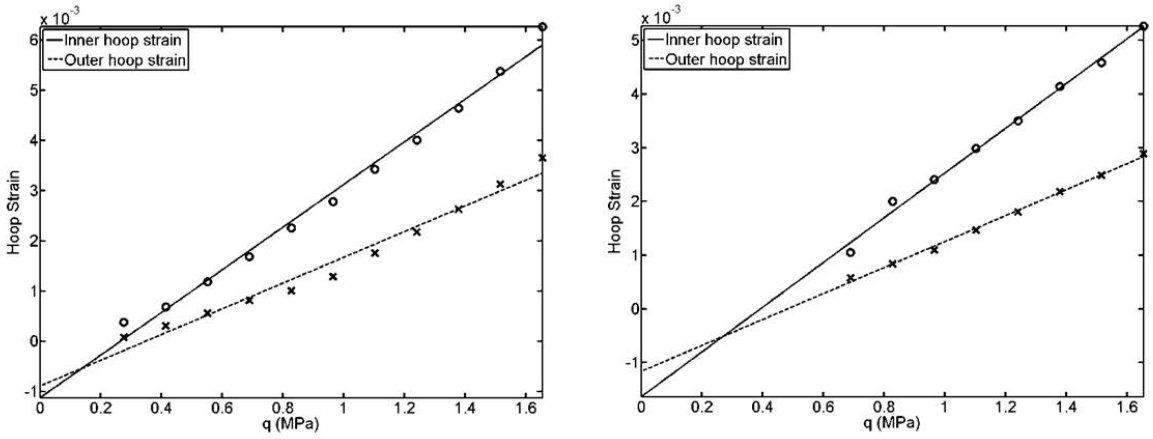

Figure A.4.1: Variation of inner and outer hoop strain increasing with the inner pressure for: (a) sample #1 and (b) sample #2

Using Eq.(A.4.1) with the slopes of the curves in Figure A.4.1, two unknown parameters for each elastic modulus distribution function, E_i and n for $E(r) = E_i (r/r_i)^n$, E_i and λ for $E(r) = E_i e^{\lambda \frac{r-r_i}{t}}$ and E_i and ξ for $E(r) = E_i + \xi(r - r_i)$, can be determined numerically.

For example, the detail steps for the exponential function are included in Section A.2.4. The results for two samples in three cases are listed in Table A.2. The calculated elastic modulus distributions of sample #1 and #2 produced by the three functions are plotted in Figure A.4.2. The distributions with the power function and the exponential function provide very close results; whereas the linear function considerably deviates from them.

Table A.2: Determined parameters for three different elastic modulus functions

Specimen number	$E(r)=E_i\left(\frac{r}{r_i}\right)^n$		$E(r)=E_i e^{\lambda\frac{r-r_i}{t}}$		$E(r)=E_i+\xi(r-r_i)$	
	E_i	n	E_i	λ	E_i	ξ
#1	288.45	5.580	314.46	1.789	207.59	235.24
#2	184.84	7.862	205.27	2.552	81.56	302.68

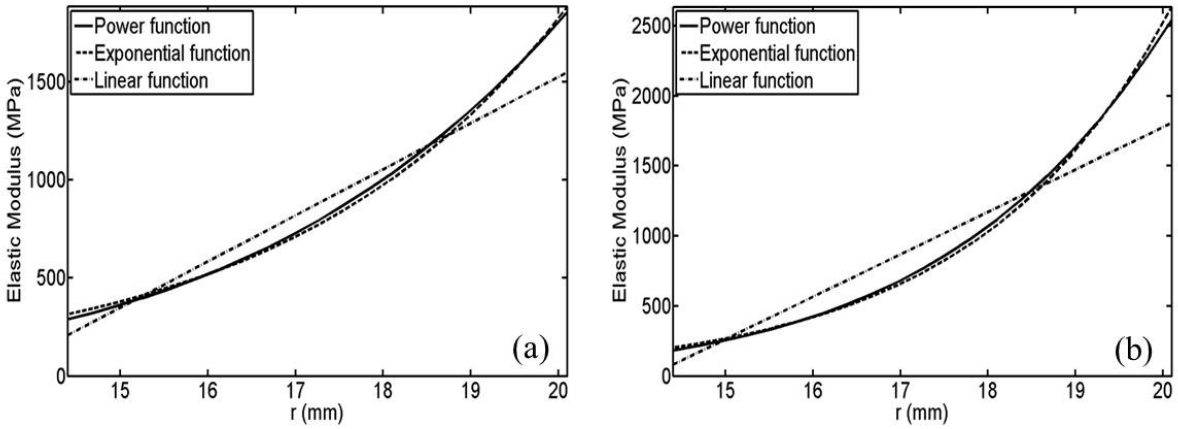

Figure A.4.2: In-plane elastic modulus distribution fitted by the three functions for: (a) sample #1, (b) sample #2 with Poisson's ratios at 0.22

Moreover, utilizing Eqs.(A.2.12), (A.2.18), (A.2.25) and the Hooke's Law with these calculated elastic modulus distributions, the hoop and radial stress and strain distributions can be predicted under any inner and outer pressure. The predictions of stress and strain are plotted in Figures A.4.3 and A.4.4, where the specimen is under specific internal pressure. The three elastic modulus distribution functions provide very close predictions of radial

stress and hoop strain. However, as for hoop stress and radial strain, the prediction of linear function deviates from the other two considerably.

To verify the accuracy of the analysis for determining the elastic modulus, the theoretical results are compared with the experimental data. For specimen #1 and #2, the test data of hoop strain with relative inner pressure is shown in Figure A.4.1. However, the actual inner pressure applied to the bamboo specimen is lower than the relative inner pressure, because the initial pressure is not zero when the inflating tubing just touches the inner surface of the bamboo. Thus, after zeroing out the initial pressure, test data of hoop strain with actual pressure are given in Table 3. It is found that there is a good consistency between the reorganized test data and the theoretical analysis. For specimen #1, the theoretical solution of the hoop strains on the inner and outer surfaces produced by three methods are all 0.0036 and 0.0022.

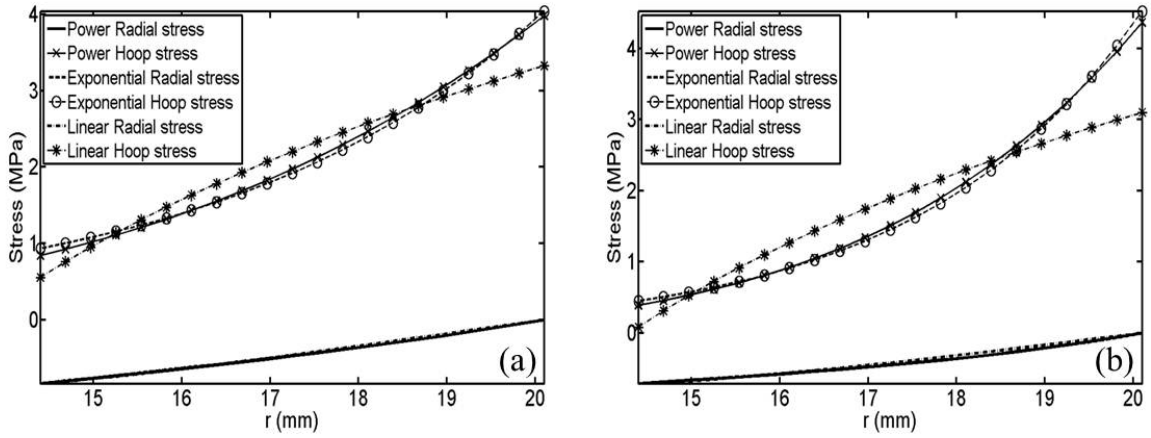

Figure A.4.3: Radial and hoop stress distribution using the three elastic modulus distribution functions under specific internal pressures for: (a) sample #1 under 0.84 internal pressure (MPa), (b) sample #2 under 0.71 internal pressure (MPa)

However, the most accurate and reasonable assumption should be chosen and adopted in future testing. The microstructure in Figure A.2.1(a) shows the bamboo is made of fibers and the matrix, which exhibit significantly different strength and elastic modulus (Nogata and Takahashi, 1995; Amada and Untao, 2001). The density of fiber plays the dominate role on the effective strength and elastic moduli of bamboo; it also becomes the basis for choosing an

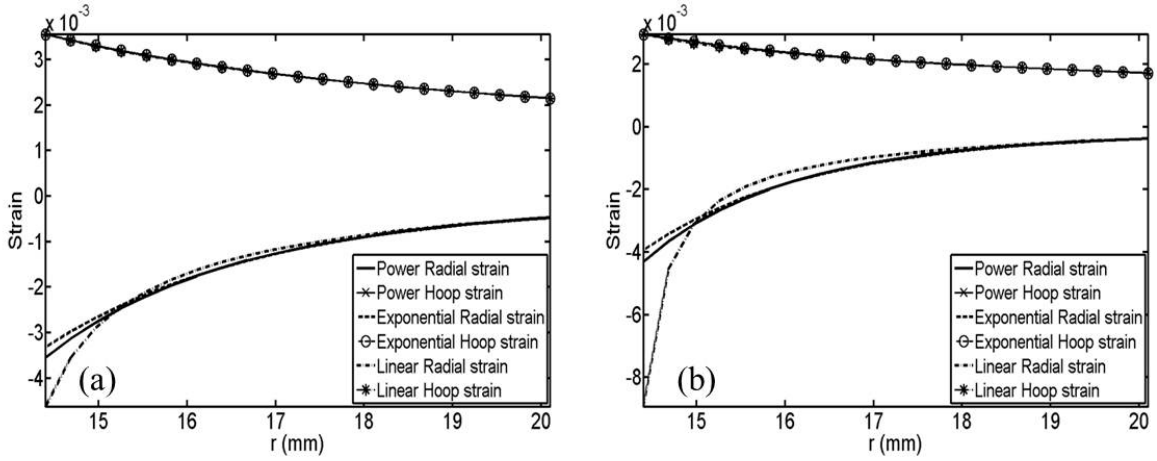

Figure A.4.4: Radial and hoop strain distribution using the three elastic modulus distribution functions under specific internal pressures for: (a) sample #1 under 0.84 internal pressure (MPa), (b) sample #2 under 0.71 internal pressure (MPa)

Table A.3: Test data of hoop strain with actual internal pressure

Specimen #1	Actual internal pressure (MPa)							
	0.43	0.56	0.70	0.84	0.98	1.11	1.25	1.39
Inner hoop strain (10^{-3})	1.69	2.26	2.79	3.43	4.01	4.65	5.38	6.27
Outer hoop strain (10^{-3})	8.12	1.01	1.29	1.76	2.18	2.63	3.13	3.65
Specimen #2	Actual internal pressure (MPa)							
	0.30	0.43	0.57	0.71	0.85	0.99	1.12	1.26
Inner hoop strain (10^{-3})	1.05	2.00	2.41	2.99	3.50	4.15	4.59	5.27
Outer hoop strain (10^{-3})	0.58	0.84	1.10	1.47	1.80	2.18	2.49	2.89

appropriate elastic distribution function. It is also mentioned that the volume fraction of fiber along the radial direction is not linear but curved from the inner to the outer surface in these studies, for example of Figure A.2.1(a). Thus, for elastic modulus distribution, the power and exponential functions in terms of radius should be more trustworthy. As shown in Figures A.4.2~A.4.4, the theoretical solutions for the modulus and the prediction of stress and strain for the first two methods are quite similar. However, because the power function always starts at zero when , when the bamboo wall is very thick, it may produce non-physical prediction. Considering the growth curve and microstructure of bamboo (Nogata and Takahashi, 1995), the exponential distribution function is recommended for future testing. However, the other two functions can be useful for quality control tests for some FGM composites which are

designed with the two distribution functions.

As mentioned in Section A.2, the variation of in-plane Poisson's ratio can be in the range from 0.12 to 0.43 (Silva et al., 2006; Garcia et al., 2012; Yu et al., 2011). To investigate the effect of Poisson's ratio on elastic modulus prediction, different Poisson's ratio, which the value is 0.15, 0.22 and 0.30, are adopted in the calculation. The comparison of elastic modulus distribution with exponential function between different Poisson's ratios for each sample is showed in Figure A.4.5. Considerable differences of elastic modulus predictions are observed at the inner and outer surfaces. In the middle range, different Poisson's ratios provide the similar results of elastic modulus predictions. Therefore, to accurately predict the elastic modulus at the inner and out surfaces, rigorous characterization of the in-plane Poisson's ratio of bamboo is necessary. Otherwise, a commonly used Poisson's ratio, say 0.22, may produce a usable prediction. In addition, the sensitivity of the Poisson's ratio on elastic modulus prediction depends on the measurements of strains. Obviously, the sample #2 exhibits a much lower sensitivity than the sample #1.

The maximum in-plane elastic modulus of sample #1 and #2 from analysis are about 1.88and 2.63 GPa. Compared with the elastic modulus, the maximum longitudinal elastic modulus is much higher; sample #1 and #2 are also tested by uniaxial compression, and their longitudinal elastic moduli are 29.82 and 35.21 GPa, respectively. The average ratio between the in-plane elastic modulus and the longitudinal elastic modulus is 0.069. This anisotropy, where the longitudinal modulus is more than ten times the value of other elastic constants, is also presented by previous research (Torres et al., 2007; U.S. Department of Agriculture Forest Service, 1999).

A.5 Summary

This appendix investigates the elastic modulus distribution in the radial direction of bamboo samples. A hollow cylinder test has been developed and the analytical formulation for the

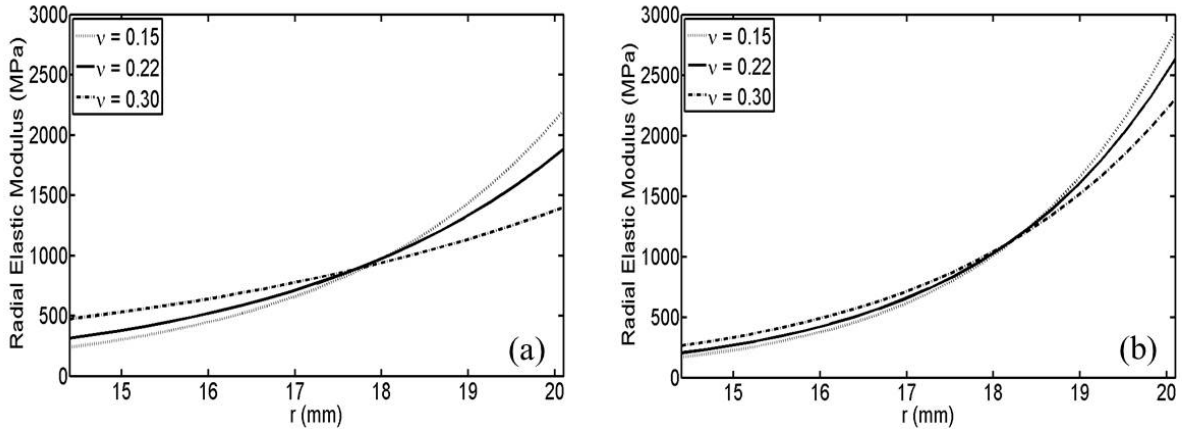

Figure A.4.5: Predictions of the in-plane elastic modulus distribution using the exponential function with Poisson's ratios at 0.15, 0.22 and 0.30, respectively, for: (a) sample #1, (b) sample #2

elastic fields has been derived for the axisymmetric problem. Furthermore, experimental tests and data analysis demonstrate that the radial stress and hoop strain on the inner and outer surface predicted by three assumptions fit the test data quite well. Combining this comparison with the consideration of the volume fraction distribution of bamboo fiber along the radial direction, the exponential distribution function $E(r) = E_i e^{\lambda \frac{r-r_i}{t}}$ is recommended in future testing.

The anisotropy of bamboo has been mentioned in some empirical studies, and our findings are in agreement with them. The average ratio between the radial modulus and the longitudinal modulus is 0.069, which is in a reasonable range. This analysis and test results demonstrate the reliability of the proposed hollow cylinder test method. Despite the advantages of the modulus analysis and hollow cylinder test, it does have its limitation. The dimensions of bamboo specimens are limited; the inner diameter of specimens has to be larger than that of the rubber hose and within the range of tubing inflation. For different applications of bamboo species, different sizes of the test equipment are recommended in future implementation.

Based on the demonstrated experiments and formulation, a standard test method is proposed for investigation of the elastic modulus distribution and the ultimate split strength

of bamboo. This study also provides a basis for research on analysis of elastic modulus and prediction of stress and strain for others hollow FGM cylinders. Further investigation of the variation of Poisson's ratio in the cross section is underway.

Appendix B

Derivation of the Velocity and Pressure Fields Caused by a Concentrated Force

Consider a concentrated force **F** at a given point **x**', the above equation can be changed to

$$\mu_0 \frac{\partial^2 v_j}{\partial x_i \partial x_i} - \frac{\partial p}{\partial x_j} = -F_j \delta(\mathbf{x} - \mathbf{x}^{'}), \qquad v_{i,i} = 0 \tag{B.0.1}$$

Following the Papkovich-Neuber general solution (Nemat-Nasser and Hori, 1999), the solution of the above equation can be constructed as

$$v_i = \frac{b_i}{\mu_0} - \frac{1}{2\mu_0} \frac{\partial \left[x_j b_j + b^0 \right]}{\partial x_i} \tag{B.0.2}$$

and

$$p = \frac{1}{2} \frac{\partial^2 \left[x_j b_j + b^0 \right]}{\partial x_i \partial x_i} \tag{B.0.3}$$

where **b** and b^0 are a vector field and a scalar field, respectively. Substituting Eqs.(B.0.2) and (B.0.3) into Eq.(B.0.1), one can obtain

$$b_{i,jj} = -F_i \delta(\mathbf{x} - \mathbf{x}^{'}); \text{ and } b^0_{,ii} = x_i^{'} F_i \delta(x - x^{'})$$

Therefore, the potential theory provide

$$b_i = \frac{1}{4\pi}\frac{F_i}{|\mathbf{x}-\mathbf{x}'|};\ \text{and}\ b^0 = -\frac{1}{4\pi}\frac{x_i' F_i}{|\mathbf{x}-\mathbf{x}'|} \tag{B.0.4}$$

Using the definition in Eqs.(3.2.8) and (3.2.9), one can write

$$v_i = \frac{1}{4\pi\mu_0}\left[\frac{\delta_{ij}}{|\mathbf{x}-\mathbf{x}'|} - \frac{1}{2}\frac{\partial^2 |\mathbf{x}-\mathbf{x}'|}{\partial x_i \partial x_j}\right] F_j = G_{ij} F_j \tag{B.0.5}$$

and

$$p = -\frac{1}{4\pi}\frac{\partial}{\partial x_j}\frac{F_j}{|\mathbf{x}-\mathbf{x}'|} = -\frac{1}{4\pi}\frac{\partial \phi}{\partial x_j} F_j \tag{B.0.6}$$

Appendix C

Expression of the Integral Terms of Φ, Ψ, Φ_p and Ψ_p and Their Derivatives

By following the concept from Mura (1987), Sun and Ju (1999) and Yin's dissertation (2004), Φ and Ψ denote the integral of the functions ϕ and ψ over an ellipsoidal inclusion Ω as

$$\begin{cases} \Phi = \int_{\Omega} \phi \, dx' \\ \Psi = \int_{\Omega} \psi \, dx' \end{cases} \tag{C.0.1}$$

where ϕ and ψ are defined in Eq.(3.2.8). In the following, Φ_p and Ψ_p denote the integral of $\phi x_p^{'}$ and $\psi x_p^{'}$

The the integral terms of Φ, Ψ, Φ_p, and Ψ_p and their derivative terms over an ellipsoidal domain can be derived and expressed as

$$\Phi = \frac{1}{2} \left[I(\lambda) - x_r x_r I_R(\lambda) \right] \tag{C.0.2}$$

$$\Phi_{,i} = -x_i I_I(\lambda) \tag{C.0.3}$$

$$\Phi_{,ij} = -\delta_{ij} I_I(\lambda) - x_i I_{I,j} \tag{C.0.4}$$

$$\Phi_p = \frac{1}{2} a_p^2 x_p \left[I_p(\lambda) - x_r x_r I_{RP}(\lambda) \right] \tag{C.0.5}$$

$$\Phi_{p,i} = \frac{1}{2} a_P^2 \left\{ \delta_{ip} \left[I_P(\lambda) - x_r x_r I_{RP}(\lambda) \right] - 2 x_p \left[x_i I_{IP}(\lambda) \right] \right\} \tag{C.0.6}$$

$$\Phi_{p,ij} = -a_P^2 \left[\delta_{ip} x_j I_{JP}(\lambda) + \delta_{jp} x_i I_{IP}(\lambda) + \delta_{ij} x_p I_{IP}(\lambda) + x_i x_p I_{IP,j}(\lambda) \right] \tag{C.0.7}$$

$$\Psi_{,ij} = \left\{ \begin{array}{c} \frac{1}{2}\delta_{ij} \left[I(\lambda) - x_r x_r I_R(\lambda) \right] - \frac{1}{2}\delta_{ij} a_I^2 \left[I_I(\lambda) - x_r x_r I_{RI}(\lambda) \right] \\ -x_i x_j \left[I_J(\lambda) - a_I^2 I_{IJ}(\lambda) \right] \end{array} \right\} \tag{C.0.8}$$

$$\Psi_{,ijk} = \left\{ \begin{array}{c} -\delta_{ij} x_k \left[I_K(\lambda) - a_I^2 I_{IK}(\lambda) \right] - \left(\delta_{ik} x_j + \delta_{jk} x_i \right) \left[I_J(\lambda) - a_I^2 I_{IJ}(\lambda) \right] \\ -x_i x_j \left[I_J(\lambda) - a_I^2 I_{IJ}(\lambda) \right]_{,k} \end{array} \right\} \tag{C.0.9}$$

$$\Psi_{,ijkl} = \left\{ \begin{array}{c} -\delta_{ij}\delta_{kl} \left[I_K(\lambda) - a_I^2 I_{IK}(\lambda) \right] - \delta_{ij} x_k \left[I_K(\lambda) - a_I^2 I_{IK}(\lambda) \right]_{,l} \\ -\left(\delta_{ik}\delta_{jl} + \delta_{jk}\delta_{il} \right) \left[I_J(\lambda) - a_I^2 I_{IJ}(\lambda) \right] - \left(\delta_{ik} x_j + \delta_{jk} x_i \right) \left[I_J(\lambda) - a_I^2 I_{IJ}(\lambda) \right]_{,l} \\ -\left(\delta_{il} x_j + \delta_{jl} x_i \right) \left[I_J(\lambda) - a_I^2 I_{IJ}(\lambda) \right]_{,k} - x_i x_j \left[I_J(\lambda) - a_I^2 I_{IJ}(\lambda) \right]_{,kl} \end{array} \right\} \tag{C.0.10}$$

$$\Psi_{p,ij} = \frac{1}{2} a_P^2 \left\{ \begin{array}{c} \delta_{ip} x_j \left[I_J(\lambda) - x_r x_r I_{RJ}(\lambda) \right] - \delta_{ip} x_j a_P^2 \left[I_{JP}(\lambda) - x_r x_r I_{RJP}(\lambda) \right] \\ + \left(\delta_{jp} x_i + \delta_{ij} x_p \right) \left[I_I(\lambda) - x_r x_r I_{RI}(\lambda) \right] \\ -a_P^2 \left(\delta_{jp} x_i + \delta_{ij} x_p \right) \left[I_{IP}(\lambda) - x_r x_r I_{RIP}(\lambda) \right] \\ +2 x_i x_j x_p \left(-I_{IJ} + a_P^2 I_{IJP} \right) \end{array} \right\} \tag{C.0.11}$$

$$\Psi_{p,ijk} = a_P^2 \left\{ \begin{array}{c} \frac{1}{2}\delta_{ip}\delta_{jk}\left[I_J\left(\lambda\right) - x_r x_r I_{RJ}\left(\lambda\right)\right] \\ -\frac{1}{2}\delta_{ip}\delta_{jk}a_P^2\left[I_{JP}\left(\lambda\right) - x_r x_r I_{RJP}\left(\lambda\right)\right] \\ +\delta_{ip}x_j\left[-x_k I_{KJ}\left(\lambda\right) + a_P^2 x_k I_{KJP}\left(\lambda\right)\right] \\ +\frac{1}{2}\left(\delta_{jp}\delta_{ik} + \delta_{ij}\delta_{kp}\right)\left[I_I\left(\lambda\right) - x_r x_r I_{RI}\left(\lambda\right)\right] \\ -\frac{1}{2}\left(\delta_{jp}\delta_{ik} + \delta_{ij}\delta_{kp}\right)a_P^2\left[I_{IP}\left(\lambda\right) - x_r x_r I_{RIP}\left(\lambda\right)\right] \\ +\left(\delta_{jp}x_i + \delta_{ij}x_p\right)\left[-x_k I_{KI}\left(\lambda\right) + a_P^2 x_k I_{KJP}\left(\lambda\right)\right] \\ +\left(\delta_{ik}x_j x_p + \delta_{jk}x_i x_p + \delta_{kp}x_i x_j\right)\left[-I_{IJ}\left(\lambda\right) + a_P^2 I_{IJP}\left(\lambda\right)\right] \\ +x_i x_j x_p\left[-I_{IJ}\left(\lambda\right) + a_P^2 I_{IJP}\left(\lambda\right)\right]_{,k} \end{array} \right\} \tag{C.0.12}$$

$$\Psi_{p,ijkl} = a_P^2 \left\{ \begin{array}{c} \delta_{ip}\delta_{jk}x_l\left(-I_{LJ} + a_P^2 I_{LJP}\right) + \left(\delta_{ip}\delta_{jl}x_k + \delta_{ip}\delta_{kl}x_j\right)\left(-I_{KJ} + a_P^2 I_{KJP}\right) \\ +\left(\delta_{ij}\delta_{kp}x_l + \delta_{ik}\delta_{jp}x_l\right)\left(-I_{LI} + a_P^2 I_{LIP}\right) \\ +\left(\delta_{ij}\delta_{kl}x_p + \delta_{ij}\delta_{lp}x_k + \delta_{il}\delta_{jp}x_k + \delta_{jp}\delta_{kl}x_i\right)\left(-I_{KI} + a_P^2 I_{KIP}\right) \\ +\left(\delta_{ik}\delta_{jl}x_p + \delta_{ik}\delta_{lp}x_j + \delta_{il}\delta_{jk}x_p\right)\left(-I_{JI} + a_P^2 I_{JIP}\right) \\ +\left(\delta_{il}\delta_{kp}x_j + \delta_{jk}\delta_{lp}x_i + \delta_{jl}\delta_{kp}x_i\right)\left(-I_{JI} + a_P^2 I_{JIP}\right) \\ +\delta_{ip}x_j x_k\left(-I_{KJ} + a_P^2 I_{KJP}\right)_{,l} + \left(\delta_{jp}x_i x_k + \delta_{ij}x_k x_p\right)\left(-I_{KI} + a_P^2 I_{KIP}\right)_{,l} \\ +\left(\delta_{ik}x_j x_p + \delta_{jk}x_i x_p + \delta_{kp}x_i x_j\right)\left(-I_{JI} + a_P^2 I_{JIP}\right)_{,l} \\ +\left(\delta_{il}x_j x_p + \delta_{jl}x_i x_p + \delta_{lp}x_i x_j\right)\left(-I_{JI} + a_P^2 I_{JIP}\right)_{,k} \\ +x_i x_j x_p\left(-I_{JI} + a_P^2 I_{JIP}\right)_{,kl} \end{array} \right\} \tag{C.0.13}$$

where Mura's extended index notation (1987) is used, namely, repeated lower case indices are summed up as usual index notation, and; upper case indices take on the same numbers as the corresponding lower case ones but are not summed. In the above equation, the following elliptic integrals are used:

$$\begin{cases} I(\lambda) &= 2\pi a_1 a_2 a_3 \int_\lambda^\infty \frac{ds}{\Delta(s)} \\ I_i(\lambda) &= 2\pi a_1 a_2 a_3 \int_\lambda^\infty \frac{ds}{\left(a_i^2+s\right)\Delta(s)} \\ I_{ij}(\lambda) &= 2\pi a_1 a_2 a_3 \int_\lambda^\infty \frac{ds}{\left(a_i^2+s\right)\left(a_j^2+s\right)\Delta(s)} \\ \Delta(s) &= \sqrt{\left(a_1^2+s\right)\left(a_2^2+s\right)\left(a_3^2+s\right)} \end{cases} \tag{C.0.14}$$

and λ is the largest root of the equation

$$\frac{x_1^2}{(a_1^2+\lambda)} + \frac{x_2^2}{(a_2^2+\lambda)} + \frac{x_3^2}{(a_3^2+\lambda)} = 1 \tag{C.0.15}$$

For a spherical domain, i.e. $a_1 = a_2 = a_3 = a$, the the integral terms of Φ, Ψ, Φ_p, and Ψ_p and their derivative terms can be explicitly derived and expressed as

$$\Phi = \begin{cases} \frac{4\pi}{3}\rho a^2 & \text{for } x > a \\ 2\pi\left(a^2 - \frac{1}{3}x^2\right) & \text{for } x \le a \end{cases} \tag{C.0.16}$$

$$\Phi_{,i} = \begin{cases} -\frac{4\pi}{3}\rho^2 a n_i & \text{for } x > a \\ -\frac{4\pi}{3}x_i & \text{for } x \le a \end{cases} \tag{C.0.17}$$

$$\Phi_{,ij} = \begin{cases} -\frac{4\pi}{3}\rho^3\left(-\delta_{ij} + 3n_i n_j\right) & \text{for } x > a \\ -\frac{4\pi}{3}\delta_{ij} & \text{for } x \le a \end{cases} \tag{C.0.18}$$

$$\Phi_p = \begin{cases} \frac{4\pi}{15}\rho^2 a^3 n_p & \text{for } x > a \\ 2\pi\left(\frac{1}{3}a^2 - \frac{1}{5}x^2\right)x_p & \text{for } x \le a \end{cases} \tag{C.0.19}$$

$$\Phi_{p,i} = \begin{cases} -\frac{4\pi}{15}\rho^3 a^2\left(-\delta_{ip} + 3n_i n_p\right) & \text{for } x > a \\ -\frac{2\pi}{15}\left[-\left(5a^2 - 3x^2\right)\delta_{ip} + 6x_i x_p\right] & \text{for } x \le a \end{cases} \tag{C.0.20}$$

$$\Phi_{p,ij} = \begin{cases} \frac{4\pi}{5}\rho^4 a\left(-\delta_{ij}n_p - \delta_{ip}n_j - \delta_{jp}n_i + 5n_in_jn_p\right) & \text{for } x > a \\ \frac{4\pi}{5}\left[-\delta_{ij}x_p - \delta_{ip}x_j - \delta_{jp}x_i\right] & \text{for } x \le a \end{cases} \tag{C.0.21}$$

$$\Psi_{,ij} = \begin{cases} \frac{4\pi}{15}\rho a^2\left[\left(5-\rho^2\right)\delta_{ij} + \left(-5+3\rho^2\right)n_in_j\right] & \text{for } x > a \\ \frac{4\pi}{15}\left[\left(5a^2 - x^2\right)\delta_{ij} - 2x_ix_j\right] & \text{for } x \le a \end{cases} \tag{C.0.22}$$

$$\Psi_{,ijk} = \begin{cases} \frac{4\pi}{15}\rho^2 a\left[\begin{array}{c} -\left(5-3\rho^2\right)\left(\delta_{ij}n_k + \delta_{ik}n_j + \delta_{jk}n_i\right) \\ +15\left(1-\rho^2\right)n_in_jn_k \end{array}\right] & \text{for } x > a \\ -\frac{8\pi}{15}\left(\delta_{ij}x_k + \delta_{ik}x_j + \delta_{jk}x_i\right) & \text{for } x \le a \end{cases} \tag{C.0.23}$$

$$\Psi_{,ijkl} = \begin{cases} \frac{4\pi\rho^3}{15}\left[\begin{array}{c} -\left(5-3\rho^2\right)\left(\delta_{ij}\delta_{kl} + \delta_{ik}\delta_{jl} + \delta_{il}\delta_{jk}\right) \\ +15\left(1-\rho^2\right)\delta_{ij}n_kn_l + 15\left(1-\rho^2\right)\delta_{kl}n_in_j \\ +15\left(1-\rho^2\right)\left(\delta_{ik}n_jn_l + \delta_{il}n_jn_k + \delta_{jk}n_in_l + \delta_{jl}n_in_k\right) \\ -15\left(3-7\rho^2\right)n_in_jn_kn_l \end{array}\right] & \text{for } x > a \\ -\frac{8\pi}{15}\left(\delta_{ij}\delta_{kl} + \delta_{ik}\delta_{jl} + \delta_{il}\delta_{jk}\right) & \text{for } x \le a \end{cases} \tag{C.0.24}$$

$$\Psi_{p,ij} = \begin{cases} \frac{4\pi}{105}a^3\rho^2\left[\begin{array}{c} \left(7-3\rho^2\right)\left(\delta_{ij}n_p + \delta_{ip}n_j + \delta_{jp}n_i\right) \\ -3\left(7-5\rho^2\right)n_in_jn_p \end{array}\right] & \text{for } x > a \\ \frac{4\pi}{105}\left[\left(7a^2 - 3x^2\right)\left(\delta_{ij}x_p + \delta_{ip}x_j + \delta_{jp}x_i\right) - 6x_ix_jx_p\right] & \text{for } x \le a \end{cases} \tag{C.0.25}$$

$$\Psi_{p,ijk} = \begin{cases} \frac{4\pi}{105}\rho^3 a^2 \begin{bmatrix} (7-3\rho^2)\left(\delta_{ij}\delta_{kp}+\delta_{ik}\delta_{jp}+\delta_{jk}\delta_{ip}\right) \\ -3\left(7-5\rho^2\right)\left(\delta_{ij}n_k n_p+\delta_{kp}n_i n_j+\delta_{ik}n_j n_p\right) \\ -3\left(7-5\rho^2\right)\left(\delta_{ip}n_j n_k+\delta_{jk}n_i n_p+\delta_{jp}n_i n_k\right) \\ +105\left(1-\rho^2\right)n_i n_j n_k n_p \end{bmatrix} & \text{for } x > a \\ \frac{4\pi}{105} \begin{bmatrix} \left(7a^2-3x^2\right)\left(\delta_{ij}\delta_{kp}+\delta_{ik}\delta_{jp}+\delta_{jk}\delta_{ip}\right) \\ -6\left(\delta_{ij}x_k x_p+\delta_{kp}x_i x_j+\delta_{ik}x_j x_p\right) \\ -6\left(\delta_{ip}x_j x_k+\delta_{jk}x_i x_p+\delta_{jp}x_i x_k\right) \end{bmatrix} & \text{for } x \leq a \end{cases} \tag{C.0.26}$$

$$\Psi_{p,ijkl} = \begin{cases} \frac{4\pi}{35}\rho^4 a \begin{bmatrix} -\left(7-5\rho^2\right)\left(\delta_{ij}\delta_{kl}+\delta_{ik}\delta_{jl}+\delta_{il}\delta_{jk}\right)n_p \\ -\left(7-5\rho^2\right)\left(\delta_{jp}\delta_{kl}+\delta_{kp}\delta_{jl}+\delta_{lp}\delta_{jk}\right)n_i \\ -\left(7-5\rho^2\right)\left(\delta_{ip}\delta_{kl}+\delta_{ik}\delta_{lp}+\delta_{il}\delta_{kp}\right)n_j \\ -\left(7-5\rho^2\right)\left(\delta_{ij}\delta_{lp}+\delta_{ip}\delta_{jl}+\delta_{il}\delta_{jp}\right)n_k \\ -\left(7-5\rho^2\right)\left(\delta_{ij}\delta_{kp}+\delta_{ik}\delta_{jp}+\delta_{ip}\delta_{jk}\right)n_l \\ +35\left(1-\rho^2\right)\left(\delta_{ij}n_k n_l n_p+\delta_{ik}n_j n_l n_p+\delta_{il}n_k n_k n_p\right) \\ +35\left(1-\rho^2\right)\left(\delta_{ip}n_j n_k n_l+\delta_{jk}n_i n_l n_p+\delta_{jl}n_i n_k n_p\right) \\ +35\left(1-\rho^2\right)\left(\delta_{jp}n_i n_k n_l+\delta_{kl}n_i n_j n_p+\delta_{kp}n_i n_j n_l\right) \\ +35\left(1-\rho^2\right)\left(\delta_{lp}n_i n_j n_k\right)-35\left(7-9\rho^2\right)n_i n_j n_k n_l n_p \end{bmatrix} & \text{for } r > a \\ -\frac{8\pi}{35}\begin{bmatrix} \left(\delta_{ij}\delta_{kl}+\delta_{ik}\delta_{jl}+\delta_{il}\delta_{jk}\right)x_p \\ +\left(\delta_{jp}\delta_{kl}+\delta_{kp}\delta_{jl}+\delta_{lp}\delta_{jk}\right)x_i \\ +\left(\delta_{ip}\delta_{kl}+\delta_{ik}\delta_{lp}+\delta_{il}\delta_{kp}\right)x_j \\ \left(\delta_{ij}\delta_{lp}+\delta_{ip}\delta_{jl}+\delta_{il}\delta_{jp}\right)x_k \\ \left(\delta_{ij}\delta_{kp}+\delta_{ik}\delta_{jp}+\delta_{ip}\delta_{jk}\right)x_l \end{bmatrix} & \text{for } r \leq a \end{cases} \tag{C.0.27}$$

where

$$\begin{cases} x = \left(x_i x_i\right)^{\frac{1}{2}} \\ \rho = \frac{a}{x} \\ n_i = \frac{x_i}{x} \end{cases} \tag{C.0.28}$$